ABSTRACT

Title of Dissertation: MODELING THE FRACTURE OF POLYMER NETWORKS

Manyuan Tao
Doctor of Philosophy, 2023

Dissertation Directed by: Professor Maria Cameron
Department of Mathematics

This dissertation is devoted to modeling the fracture of highly elastic materials that consist of polymer networks, such as elastomers and hydrogels. These polymer materials are composed of long polymer chains of repeating molecular units, which are crosslinked to form a three-dimensional network structure. A polymer network fractures by breaking covalent bonds, but the experimentally measured strength of a polymer network is orders of magnitude lower than the strength of covalent bonds. In this dissertation, we develop mesoscale models to understand what are the necessary ingredients leading to a large reduction in the strength of polymer networks observed in experiments.

We hypothesize that the large reduction in strength is caused by statistical variation in lengths of polymer chains and a J-shaped stress-stretch relationship. The polymer chain carries entropic forces for most of the extension and carries covalent forces only for a narrow range of the extension. As a result, the statistical distribution of chain lengths causes only a small fraction of polymer chains to be highly stressed when the network is near fracture.

We test this hypothesis using two mesoscale models: an idealized *parallel chain model* and a two-dimensional *network model*. Both models assume a statistical distribution for the lengths of polymer chains. Polymer chains are represented by freely-jointed chains that feature a nonlinear J-shaped stress-stretch relationship. The parallel chain model allows for simple calculations and is amenable for analysis by analytical tools. The network model accounts for the effect of stress concentration and is amenable for numerical simulations.

Our models show that the combination of a J-shaped stress-stretch relationship and a distribution of chain lengths leads to a large reduction in strength, while keeping the variability in strength small from sample to sample. The large scatter in chain lengths causes a reduction in strength by up to two orders of magnitude, which explains a portion of the giant discrepancy between the experimentally measured strength of hydrogels and the strength of covalent bonds. Furthermore, our models demonstrate a power law relationship between the strength and the scatter in chain lengths. We provide an analytical derivation of the power law by taking advantage of the simplicity of the parallel chain model.

In addition to studying macroscopic fracture properties, we further investigate the microscopic characteristics and the breaking mechanism of the polymer network, using the network model. By examining the characteristics of shortest paths, we find that the links traversed by a large number of shortest paths are more likely to break. Finally, we connect the microstructure of the network to the macroscopic mechanical properties. It is observed that the strength of the network correlates with the growth of holes during deformation.

MODELING THE FRACTURE OF POLYMER NETWORKS

by

Manyuan Tao

Dissertation submitted to the Faculty of the Graduate School of the
University of Maryland, College Park in partial fulfillment
of the requirements for the degree of
Doctor of Philosophy
2023

Advisory Committee:
Professor Maria Cameron, Chair/Advisor
Professor Ricardo Nochetto
Professor Dionisios Margetis
Professor Deep Ray
Professor Pratyush Tiwary, Dean's Representative

Acknowledgments

First of all, I owe my sincere gratitude to my dear advisor, Dr. Maria Cameron, for guiding me through the research journey on applied mathematical problems over the past four years. Masha has been constantly providing me with inspiring feedback and uplifting encouragement, making my graduate study smooth and fruitful. I appreciate the invaluable time, effort, and support she has dedicated to this dissertation. I have learnt from Masha not only aspects of research, but have also been highly motivated by her passion for life. It is my greatest fortune to have Masha as my PhD advisor.

I would like to express my gratitude to the members of my dissertation committee: Dr. Ricardo Nochetto, Dr. Dionisios Margetis, Dr. Deep Ray, and Dr. Pratyush Tiwary for the indispensable help, advice, and support they have given me along the way. I thank Dr. P. S. Krishnaprasad for introducing me to the field of optimal control theory.

Many thanks to all of my friends, in Maryland and back in China, for their company to share joys and difficulties, ups and downs. I truly cherish the supportive atmosphere in Masha's research group. I thank my bestie Ye Tao for her lovely conversations all the time.

Most importantly, none of my academic achievements would have been attainable without the support of my family. I owe my deepest gratitude to my dearest, lovely parents: Dajun Tao and Juying Yuan for their endless love, unconditional support, and smiling faces. They have been consistently creating such a loving environment for me that I always feel confident and determined to make my own choices in life.

Table of Contents

List of Tables

List of Figures

Chapter 1: Introduction to the dissertation

This dissertation is devoted to modeling the fracture of highly elastic materials that consist of polymer networks, such as elastomers and hydrogels. We start the introduction with an overview of polymer materials and their mechanical properties. Then we review the experimental works and theoretical models that investigate fracture mechanisms for many observed phenomena in polymer materials, and discuss the phenomena that have not been explained in previous studies. In the end we summarize the main contributions of this dissertation and provide an outline for the following chapters.

1.1 Background

Polymer materials are everywhere in our daily life. They are divided into two types: naturally occurring and synthetic. Both types of polymers play essential roles due to their broad spectrum of properties [1, 2]. Wool, cotton, and cellulose are natural polymer-based materials that have been used since ancient times. Proteins and DNA in our bodies are natural biopolymers that are fundamental to biological structure and function. Examples of synthetic polymers include nylon in fabrics and polyethylene in plastics. These polymer materials consist of long polymer chains of repeating molecular units, known as monomers, which are crosslinked to form a three-dimensional network structure.

In recent years, hydrogels – the polymer network swollen with water – have found numerous biomedical applications, e.g., scaffolds for tissue engineering [3], drug delivery [4] (drug molecules are held inside polymeric networks), and design of artificial muscles, skins, smart optical systems (contact lenses) [5–7]. Hydrogels are also used in other spheres of industry. The network structure of hydrogels can absorb large quantities of fluids without the essential skeletal rupture. The ability to expand upon absorbing fluids makes hydrogels good packers for sealing in oil wells [8, 9].

Numerous existing and potential applications for hydrogels motivate the study of their fracture properties. These properties are typically quantified by the material characteristics such as strength, extensibility, work of fracture, shear modulus, and toughness. In recent experimental work by Yang, Yin, and Suo [10], samples of polyacrylamide hydrogels without and with initial cut were stretched in a few different settings and stress-stretch curves were obtained. The key finding of [10] is that *the scatter in material properties such as strength, extensibility, and work of fracture between samples is relatively small* – variability, i.e., the ratio of the standard deviation to the mean was found to be within 10%; however, *the experimentally measured strength is much lower, by about three orders of magnitude, than the theoretical strength associated with breaking covalent bonds.* By contrast, the strength of brittle hard materials such as silica scatters enormously, often by orders of magnitude [11]. A comparison between silica [11, 12] and polyacrylamide (PAAM) hydrogel [10] on the mechanical properties is summarized in Table 1.1.

It should be noted that the large discrepancy between the experimental strength of silica and the covalent bond strength is known to be caused by crack-like flaws [12], i.e., stress concentration at defects. However, the ultimate properties (strength, extensibility,

Table 1.1: A comparison between silica glass and PAAM hydrogel.

Silica glass	PAAM hydrogel
A model hard material	A model soft material
Elastic prior to rupture	Elastic prior to rupture
Modulus scatters by $\sim 1\%$	Modulus scatters by $\sim 10\%$
Strength scatters by $\gg 10\%$ – caused by *crack-like flaws*	Strength scatters by $\sim 10\%$ – **needs to be explained**
Strength $\ll$ molecular strength – caused by *cracks*	Strength $\ll$ molecular strength – **needs to be explained**

and work of fracture) of PAAM hydrogels are insensitive to small cuts up to 1 mm [10], suggesting that the structure of a polymer network deconcentrates stress. *This fundamental difference between silica glass and polymeric gels draws our attention. Why is the measured strength of a polymer network so low compared to the strength of covalent bonds?*

The hydrogel is a polymer network filled with water molecules, as depicted in Fig. 1.1. Water has low viscosity so the friction between polymer chains is low. When stretched, the polymer network deforms with near-perfect elasticity. The elastic deformation is due to the entropy of polymer chains [13]. At a crack tip in the stretched polymer network, consider a polymer chain that is about to break. Because friction between polymer chains is negligible, the tension in the polymer chain transmits over its entire length. The tension in the polymer chain also transmits to other polymer chains through crosslinks and entanglements [14]. Furthermore, the high tension transmits to even more polymer chains as they stretch and

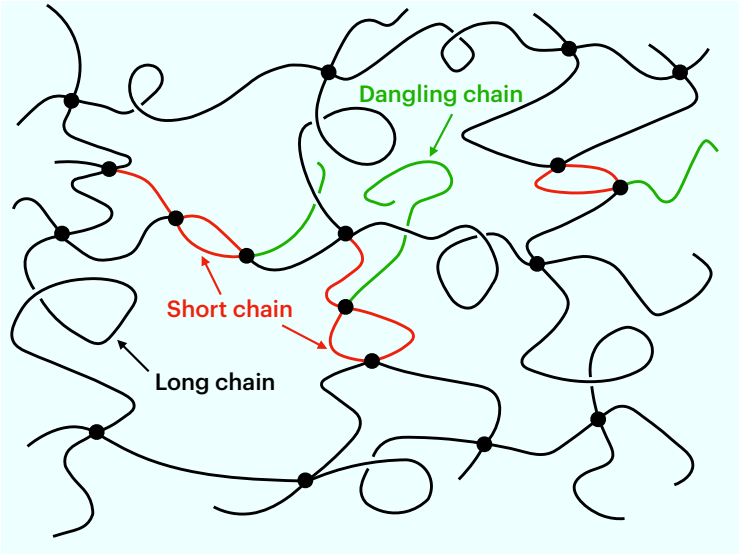

Figure 1.1: An illustration for network imperfection in hydrogels. Short chains, long chains, and dangling chains are coexistent in the network.

re-orientate. When the polymer chain breaks at a single covalent bond, high tension in a large volume of the polymer network releases. That is, a long-chain polymer network of negligible interchain friction deconcentrates stress at a crack tip, so that a small crack-like flaw will not lower the microscopically measured strength appreciably. Recently it has been suggested by the work of Z. Suo [10] that the low strength of a polymer network originates not from a crack-like flaw, but from the polymer network itself.

The central claim of [10] is that the small scatter of material characteristics from sample to sample, combined with the large reduction in strength compared to the ideal network, is a manifestation of something very basic: *network imperfection* (see Fig. 1.1). The polymer network consists of polymer chains with different lengths. When the network is stretched near rupture, only a small fraction of polymer chains are stressed to the covalent bond strength, and other polymer chains still carry entropic forces. The two types of forces differ by about two orders of magnitude.

1.2 Definitions

In this section, we provide an overview of the key mechanical properties that we will refer to throughout this dissertation.

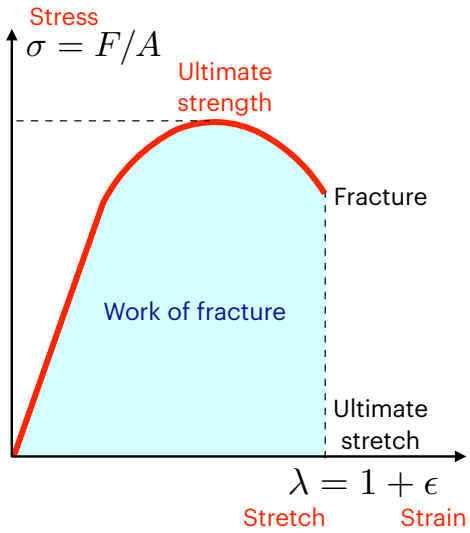

Figure 1.2: Stress-stretch curve.

Stress. Stress is a measure of the force applied to a material per unit area, defined as the ratio of the force to the cross-sectional area of the material, $\sigma = F/A$. Stress is expressed in units of force per unit area (e.g., $\mathrm{N/m^2}$ or Pa).

Stretch. Stretch is defined as the fractional change in length of the material, i.e., the ratio of the final length to the initial length, $\lambda = l/l_0$. It is a dimensionless quantity that measures the elongation of a material when subjected to stress.

Strength. Strength refers to the maximum stress (i.e. maximum force per unit area) that a material can withstand before failure. It indicates the ability of a material to resist deformation under an applied load.

Extensibility. Extensibility is a measure of how much a material can be elongated before reaching its breaking point. In this work, we define the extensibility by the stretch at which the maximum force is achieved.

Work of fracture. The work of fracture is a measure of the energy required to rupture a material, defined as the area under the stress-stretch curve up to fracture.

Modulus. The modulus, also known as Young's modulus, is a measure of the stiffness of a material, defined as the slope of the stress-stretch curve during elastic deformation.

1.3 Previous studies

A real polymer network is imperfect. Short chains, long chains, and dangling chains are coexistent in the network, as shown in Fig. 1.1. The idea that network imperfection plays a fundamental role in defining mechanical properties of polymer materials dates back to the work of Lake and Thomas [15] where they conducted stretching experiments with precut samples of vulcanized rubber. They explained the observed hysteresis (the Mullins effect [16]) in a sequence of stretches by tearing the shortest polymer chain in each stretch. Therefore, if a sample is stretched consecutively two times to the same length, the work of the second stretch is smaller than that of the first one.

Network imperfection also profoundly affects other mechanical properties of polymer materials, such as strength [17] and toughness [18]. In recent experimental work [10], the effects of network imperfection on mechanical properties have been studied for hydrogels. The central claim of this work is that network imperfection keeps the ultimate properties (strength, extensibility, and work of fracture) of hydrogels within small scatter from sample to sample, but does significantly reduce the ultimate properties compared to those of the perfect network.

We remark that the main difference between the vulcanized rubber and the hydrogel is that the polymer network in rubber is filled with air while the network in hydrogel is filled with water. While the latter situation may seem more involved, it is actually more amenable to modeling. On the one hand, water serves as a lubricant so the friction between polymer chains can be neglected. On the other hand, water has low viscosity, hence the additional force required to cause its flow within the network is negligible.

Understanding mechanical properties of polymer networks on the theoretical level, i.e., designing models that capture the observed phenomena, is of great interest. This challenge has been approached from two directions in the literature: macroscopic and microscopic. A macroscopic PDE-based model for the fracture of polymeric gels was developed in [19], and finite element simulations of the fracture of precut hydrogel samples were performed. The advantage of this PDE model is that it allows us to compute fracture properties of reasonable size samples and make theoretical predictions. Nevertheless, as any PDE model, it is homogenized and does not account for randomness in lengths of polymer chains.

On the other extreme of scales, fracture of polymer materials has been studied by Robbins and collaborators by means of molecular simulations [20, 21]. Formation of craze ahead of the crack tip propagating through the sample, craze deformation, and eventual failure were examined on a submicron scale. The polymer chains were modeled by means of beads interacting according to a truncated Lennard-Jones potential glued to a fourth-degree polynomial. These studies provide valuable insights into the processes taking place on the molecular level in polymer networks while they are being stretched and ruptured. However, molecular simulations are too computationally expensive to conduct many enough of them to accumulate data for statistical analysis.

Finally, we present a review of existing works that investigated the stress-stretch relationship of polymer chains. A J-shaped stress-stretch relationship was derived in the seminal work of Kuhn and Grün [22] where the force-extension curve of a freely-jointed chain is described by the Langevin function. For single chains of polyacrylamide, a J-shaped force-extension curve was measured using an atomic force microscope [23]. It turns out that the experimentally measured force-extension curve fits the Langevin function well except

when the chains are near rupture. In [23], the authors fit the measured force-extension curve by modifying the Langevin function with a stiffness near rupture.

The J-shaped stress-stretch relationships have been combined with polydispersity, i.e., a distribution of chain lengths, in the mechanics models. Itskov and Knyazeva [24] incorporated polydispersity into the freely-jointed chain model to simulate the Mullins effect. Lavoie et al. [25] combined the Langevin chain model and rate-dependent scission to compare stress-stretch relationships in mono and polydisperse networks. Yang et al. [26] developed a cohesive zone model which considers a J-shaped force-extension relationship, rate-dependent chain rupture, and polydispersity. These works focused on studying various aspects of stress-stretch relationships, but the effect of the scatter in chain lengths on the mechanical properties of polymer networks was not specifically investigated.

1.4 Unexplained phenomena and research goals

In this dissertation, we focus our attention on the phenomena that have not been explained in previous works. Our goal is to understand what are the necessary ingredients leading to a combination of the following fracture properties observed in [10]:

- A small variability in strength between samples.
- A large reduction in strength in comparison with the ideal network where all polymer chains are of the same length.

Since there is no existing common model that explains these phenomena, our task is to develop mesoscale models that allow for variability in local properties and are amenable for numerical simulations.

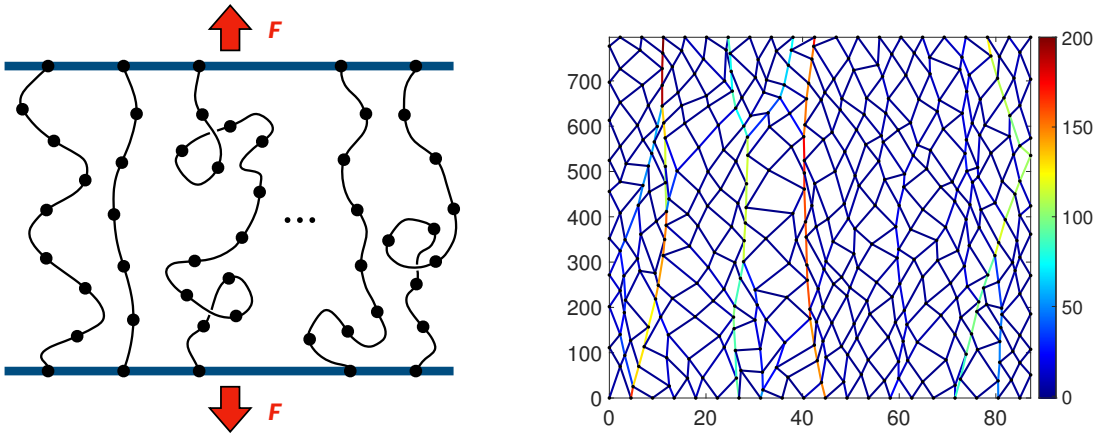

(a) Parallel chain model

(b) Network model

Figure 1.3: (a): The parallel chain model. A large number of polymer chains are arranged in parallel and attached to two rigid plates. Each chain has a random number of monomers. (b): The network model. An array of nodes is connected into a diamond grid by links. Each link represents a polymer chain consisting of a random number of Kuhn segments. The network is of size 20×20. The colorcode shows the stress of individual links.

We hypothesize that the unexplained phenomena described above are caused by the following two facts present in the polymer network:

(i) Statistical variation in lengths of polymer chains.

(ii) A nonlinear J-shaped stress-stretch relationship.

When the network is near fracture, only a small fraction of polymer chains carry the force near the covalent strength, and the majority of chains carry forces due to entropic elasticity.

We test this hypothesis using two simple models depicted in Fig. 1.3: an idealized *parallel chain model* and a two-dimensional *network model*. Both models feature a nonlinear J-shaped stress-stretch relationship and assume a statistical distribution for the lengths of polymer chains. The parallel chain model allows for simple calculations and is amenable for analysis by analytical tools. The network model is designed to mimic the polymer skeleton of hydrogels and is amenable for numerical simulations.

The parallel chain model can be simulated numerically with low computational cost. The advantage of this idealized model is that it allows us to calculate the mean force exerted by polymer chains and analyze important mechanical properties, including strength and extensibility. In particular, we are interested in the reduction in strength compared to the ideal model. By numerical computation and analytical derivation, our objective is to understand and quantify the effect of the scatter in chain lengths on the strength of the parallel chain model.

The network model accounts for the effects of stress concentration and interchain interaction, which are ignored in the parallel chain model. As a result, simulations of the network model are much more computationally demanding, especially for larger networks. The goal of our work there is to investigate the reduction in ultimate properties (strength, extensibility, and work of fracture) and the variation in these properties from sample to sample. This investigation focuses on understanding the fracture properties of networks with a distribution of chain lengths.

In addition to studying macroscopic fracture properties, we further focus our attention on the microscopic characteristics and the breaking mechanism of the polymer network. This part of research is motivated by the recent work of Yin et al. [27] where they performed topology analyses of the polymer network by means of coarse-grained molecular simulations. The authors characterized the microstructure of strain-induced damage by the evolution of the global shortest path length between well-separated crosslinks. Inspired by this finding, we investigate the characteristics of shortest paths and formation of holes in the network model. The objective is to establish a connection between the microstructure of the network and the macroscopic mechanical properties.

1.5 Summary and outline

In this dissertation, we develop two mesoscale models, the parallel chain model and the network model, to study the fracture properties of polymer networks observed from experiments. Our models assume a J-shaped stress-stretch relationship and account for statistical variation in lengths of polymer chains. We investigate the effects of these two key features on reducing strength by numerical simulations and analytical argument for the parallel chain model, and by numerical simulations for the network model. We develop a software package written in the C language from scratch since the standard engineering software (e.g. ABACUS) cannot handle the numerical issues arising in the simulations. Furthermore, we examine the microscopic characteristics of the network structure, including evolution of shortest paths and holes. The main contributions are summarized as follows.

In Chapter 2, we provide a complete description of the two facts that our models account for, which form the foundation for our work in the later chapters. We first present an overview of the classical Langevin function [22] and the modified Langevin function [23], which are standard for describing the force-extension relationship of freely-jointed chains. However, they are not suitable for simulations of the network model since they yield a zero chain length at zero force. This entails the need for designing appropriate stress-stretch relationships that allow for a nonzero equilibrium length. For this purpose, we derive the root-mean-square displacement of a polymer chain in the direction of the force. We also discuss the choice of the chain length distribution motivated by experimental data [18, 28].

In Chapter 3, we investigate the effect of statistical variation in lengths of polymer chains on strength using the parallel chain model. We consider three types of parallel chain

models: type one assumes a linear stress-stretch relationship, while the other two feature J-shaped stress-stretch curves derived from the Langevin function [22] and the modified Langevin function [23], respectively. Our results show that, with the J-shaped stress-stretch relationship, even a small scatter in chain lengths greatly reduces the strength of the parallel chain model. The scatter leads to a reduction in strength by up to two orders of magnitude. We further show that the strength of the parallel chain model scales with the coefficient of variation, the ratio of the standard deviation to the mean, by a power law. This power law relationship is also derived analytically, demonstrating the robustness of the power law to the J-shaped force-extension curve and the distribution of chain lengths.

In Chapter 4, we develop a network model based on a diamond grid structure, which is an idealized representation of a polymer network. We incorporate network imperfection into the model by assuming a statistical distribution for the lengths of polymer chains. Numerical simulations are performed on networks of different sizes and of various amounts of scatter in chain lengths. By conducting stretching experiments of network samples up to complete fracture, we obtain stress-stretch curves from which strength, extensibility, and work of fracture can be extracted. We find that the strength of the network model can be reduced to as low as 15% of the ideal strength, while the variation in strength is small from sample to sample. Furthermore, the power law between the strength and the scatter in chain lengths is observed in the network model.

The reduction in strength obtained by both models accounts for a portion of the giant discrepancy between the experimentally measured strength of hydrogels and the strength of covalent bonds [10]. One limitation of the network model is that we cannot extrapolate the power law relationship to larger network sizes, and simulations of larger networks are

more computationally demanding. This motivates our subsequent study on the microscopic characteristics and the breaking mechanism of the polymer network.

In Chapter 5, we shift our focus towards investigating the connection between the microstructure of the network model and the macroscopic mechanical properties. The work in this chapter can be divided into two parts. In the first part, we focus on understanding where the stress tends to concentrate in the network. As suggested by [27], we analyze the topology of the network model by computing the *shortest paths* between the top and bottom boundaries. We characterize the broken links during deformation through analyses of shortest paths in both qualitative and quantitative ways. We confirm that broken links tend to occur on the global minimum shortest path, or on the shortest path with length very close to the global minimum. Furthermore, we find that the links traversed by a large number of shortest paths are more likely to experience breakage. We demonstrate that link-breaking events can be quantitatively characterized by the number of shortest paths passing through the link, which represents the betweenness centrality of a link.

In the second part of Chapter 5, we focus on the question of how the macroscopic mechanical properties, such as strength, are controlled by the microstructural evolution of the polymer network. We answer this question from two perspectives. On the one hand, we analyze the evolution of the shortest path length distribution and find that the peak force occurs when the minimum shortest path length approaches the initial average length of shortest paths. On the other hand, we study the formation and growth of *holes* while the network is being stretched and torn. We demonstrate a phase transition in the network topology as the applied force grows, reaches the peak, and eventually drops down to zero.

Finally, in Chapter 6 we give conclusions and discuss future perspectives.

Chapter 2: Stress-stretch relationship and chain length distribution

This chapter provides a full description of the two facts that our models account for in the modeling of polymer chains. That is, a nonlinear J-shaped stress-stretch relationship and statistical variation in lengths of polymer chains. We hypothesize that the combination of these two key features leads to a large reduction in the strength of polymer networks. The theoretical details discussed in this chapter for modeling a single chain will be applied in simulations of fracture of polymer networks in Chapters 3 and 4.

We first present an overview of the classical Langevin function which is standard for describing the force-extension relationship of a freely-jointed chain. However, the Langevin function is not appropriate for simulations of the network model since it yields a zero chain length at zero force. We then derive the root-mean-square displacement of a freely-jointed chain in the direction of the force, which admits a nonzero equilibrium length. We employ the root-mean-square displacement as the nonlinear J-shaped stress-stretch relationship in our models.

Moreover, we discuss the choice of the chain length distribution to be used in the simulations. Motivated by experimental data [18, 28], we assume the Weibull distribution for the lengths of polymer chains. It should be noted that the chain length distribution to be used in simulations is *not* limited to the Weibull distribution.

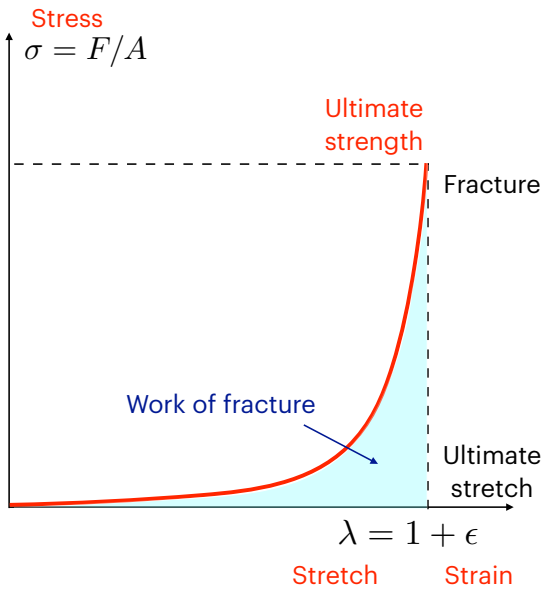

Figure 2.1: J-shaped stress-stretch curve.

2.1 Introduction

In Section 2.2, we study the stress-stretch relationship on a single polymer chain. In engineering, a stress-stretch curve for a material gives the relationship between the stress, i.e., the ratio of the force to the cross-sectional area of the material, and the stretch, i.e., the ratio of the final length to the initial length. It reveals many of the mechanical properties of the material, such as Young's modulus, the ultimate strength, and the work of fracture, as illustrated in Fig. 2.1. Many biological soft tissues (e.g. mammalian skin and flesh [5,6]) exhibit the type of stress-stretch curve shown in this figure, which is known as a J-shaped curve [7]. The curve shows the following behavior of a material. Initially, small increases in stress lead to large extensions. As the fracture point is approached, the material becomes stiffer and more difficult to extend. Such J-shaped stress-stretch behavior causes many biomaterials to be extremely tough, even though the fracture energy (i.e. work of fracture)

is not particularly high. Returning to the microscopic scale, we employ this J-shaped curve as the stress-stretch relationship on a polymer chain.

The first statistical attempt for deriving a J-shaped stress-stretch relationship was made by Kuhn and Grün [22], where the force-extension curve of a single freely-jointed chain is described by the Langevin function. For a single chain of polyacrylamide (PAAM), a J-shaped force-extension curve was measured using an atomic force microscope [23]. The experimental force-extension curve fits the Langevin function well except when the chains are near rupture. The covalent bonds are stretchable near rupture, which limits the steep slope of the Langevin function. Zhang et al. [23] fit the measured force-extension curve using an extensible freely-jointed chain (EFJC) model, in which the Langevin function is modified with a stiffness near rupture as an adjustable parameter.

It is important to note that the Langevin function describes the mean displacement of a freely-jointed chain in the direction of the applied force [22]. We provide a brief derivation of this classical function via statistical treatment of a single polymer chain in Section 2.2.1. It can be seen that the mean displacement of a chain is zero if there is no pulling force. However, for a freely-jointed chain of n links, each with equal length l, it is well-known that the equilibrium chain length takes the root-mean-square value, $\sqrt{n}\,l$. This fact motivates our work in Section 2.3, where we derive the root-mean-square displacement of a polymer chain in the direction of the force.

2.2 J-shaped stress-stretch relationship

In this section, we describe in full detail the characteristic stress-stretch relationship that is nonlinear and J-shaped (see Fig. 2.1) on a single polymer chain. We first present an overview of the classical Langevin function which expresses the end-to-end distance of a freely-jointed chain as a function of the applied pulling force. The derivation of the Langevin function using a statistical model of polymer chains is attributed to the pioneering work of Kuhn and Grün [22]. This work was originally written in German. Here we provide a re-derivation of the Langevin function in Section 2.2.1. Furthermore, we describe the modified Langevin function that fits the experimentally measured force-extension curve for polyacrylamide (PAAM) [23] in Section 2.2.2.

We represent a polymer chain by a freely-jointed chain depicted in Fig. 2.2(a), which consists of n statistically independent, rigid segments of equal length. These statistically independent segments are referred to as Kuhn segments. The length of a Kuhn segment, denoted by I_k, is called the Kuhn length [29, 30]. Each chain possesses a stress-stretch relationship of the form $f = f(z, n)$ where f is the applied pulling force, z is the extension of the chain (i.e. end-to-end distance), and n is the number of Kuhn segments per chain. We prescribe a constant breaking force on the chain, f_b, which is much larger than the entropic force. If the force on a chain exceeds f_b, the chain ruptures and is removed. The breaking force is the same for all polymer chains. Throughout this chapter, we will always assume that the force f and the distance z are nondimensional quantities. We denote the force measured in Newtons and the distance measured in meters by $\mathbf{f}$ and $\mathbf{z}$, respectively.

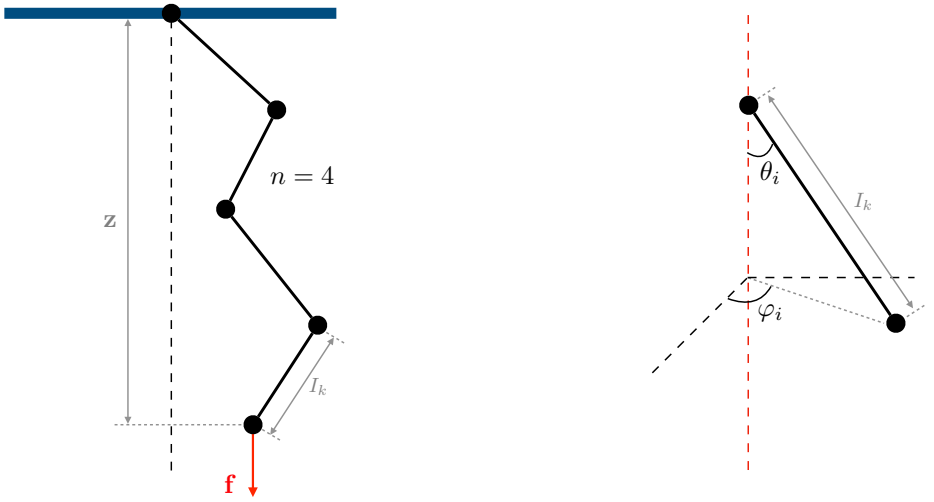

(a) (b)

Figure 2.2: (a): Freely-jointed chain model. (b): The red dashed line is the axis along the direction of the force. θ_i is the polar angle between the ith link and the axis of the force. φ_i is the azimuthal angle around the axis of the force.

2.2.1 The classical Langevin function

The classical Langevin function, first derived in the work of Kuhn and Grün [22], describes the force law of a polymer chain. For a polymer chain of n Kuhn segments, the force-extension relationship, i.e., the end-to-end distance $\mathbf{z}$ as a function of the applied pulling force $\mathbf{f}$, is given by the Langevin function:

$$\mathbf{z}(\mathbf{f}) = nI_k \left[\coth\left(\frac{\mathbf{f}I_k}{k_B T}\right) - \frac{k_B T}{\mathbf{f}I_k} \right], \tag{2.1}$$

where I_k is the Kuhn length, k_B is the Boltzmann constant, and T is the temperature. It was derived based on a *freely-jointed chain* model (see Fig. 2.2(a)) where a polymer chain is represented by a sequence of beads connected by rigid links. Each link of length I_k

represents a monomer. The n rigid links are joined at their ends by freely rotating joints which represent the covalent bonds. One end of the polymer chain is fixed while the other end is subject to a pulling force of constant magnitude $\mathbf{f}$ in a fixed direction. Let $\mathbf{z}$ be the displacement of the chain associated with the force, i.e., the end-to-end distance projected onto the direction of the force. The mean value of the displacement $\langle \mathbf{z} \rangle$ under the external force $\mathbf{f}$ was derived by Kuhn and Grün [22]. Here we provide a re-derivation of the Langevin function for which the original work was written in German.

In statistical mechanics, the mean value of the displacement at equilibrium is defined by a weighted sum over all microstates γ:

$$\langle \mathbf{z} \rangle = \sum_{\gamma} p_{\gamma} \mathbf{z}_{\gamma}, \tag{2.2}$$

where p_{γ} is the probability for the system to be in a microstate γ and $\mathbf{z}_{\gamma}$ is the displacement of the polymer chain at that microstate. The probability of a microstate is proportional to the Boltzmann probability density [31]:

$$p_{\gamma} \sim \exp\left(\frac{\mathbf{f}\mathbf{z}_{\gamma}}{k_B T}\right). \tag{2.3}$$

A microstate of the system is characterized by two sets of angles (see Fig. 2.2(b)): the polar angle between each rigid link and the axis of the force, $\{\theta_i\}$, as well as the azimuthal angle that each link rotates around the axis of the force, $\{\varphi_i\}$. The two angles vary in the intervals $\theta_i \in [0, \pi]$ and $\varphi_i \in [0, 2\pi]$. The number of microstates is proportional to the surface element on the unit sphere, $\sin\theta_i d\theta_i d\varphi_i$. Then the weighted sum over all microstates

in (2.2) is given by an integral:

$$\sum_{\gamma} = \int_0^{2\pi} \cdots \int_0^{2\pi} \int_0^{\pi} \cdots \int_0^{\pi} \sin\theta_1 \cdots \sin\theta_n d\theta_1 \cdots d\theta_n d\varphi_1 \cdots d\varphi_n$$
$$= (2\pi)^n \int_0^{\pi} \cdots \int_0^{\pi} \sin\theta_1 \cdots \sin\theta_n d\theta_1 \cdots d\theta_n. \tag{2.4}$$

We further write the displacement $\mathbf{z}_\gamma$ of the chain at microstate γ in terms of the angles $\{(\theta_i, \varphi_i)\}$, $i = 1, 2, ..., n$:

$$\mathbf{z}_\gamma = \sum_{i=1}^{n} I_k \cos\theta_i. \tag{2.5}$$

Thus the mean value of $\mathbf{z}$ is given by

$$\langle \mathbf{z} \rangle = \frac{(2\pi)^n \int_0^{\pi} \cdots \int_0^{\pi} \left(\sum_{i=1}^n I_k \cos\theta_i\right) \left[\prod_{i=1}^n \exp\left(\frac{\mathbf{f} I_k \cos\theta_i}{k_B T}\right) \sin\theta_i\right] d\theta_1 \cdots d\theta_n}{(2\pi)^n \int_0^{\pi} \cdots \int_0^{\pi} \left[\prod_{i=1}^n \exp\left(\frac{\mathbf{f} I_k \cos\theta_i}{k_B T}\right) \sin\theta_i\right] d\theta_1 \cdots d\theta_n}$$
$$= \frac{I_k \sum_{i=1}^n \left[\int_0^{\pi} \exp\left(\frac{\mathbf{f} I_k \cos\theta_i}{k_B T}\right) \sin\theta_i \cos\theta_i d\theta_i\right] \left[\prod_{j\neq i} \int_0^{\pi} \exp\left(\frac{\mathbf{f} I_k \cos\theta_j}{k_B T}\right) \sin\theta_j d\theta_j\right]}{\prod_{i=1}^n \int_0^{\pi} \exp\left(\frac{\mathbf{f} I_k \cos\theta_i}{k_B T}\right) \sin\theta_i d\theta_i}. \tag{2.6}$$

Since the angles $\{\theta_i\}_{i=1}^n$ are independent, we can replace θ_i and θ_j in (2.6) by a uniform angle θ. We then have

$$\langle \mathbf{z} \rangle = \frac{n I_k \left[\int_0^{\pi} \exp\left(\frac{\mathbf{f} I_k \cos\theta}{k_B T}\right) \sin\theta \cos\theta d\theta\right] \left[\int_0^{\pi} \exp\left(\frac{\mathbf{f} I_k \cos\theta}{k_B T}\right) \sin\theta d\theta\right]^{n-1}}{\left[\int_0^{\pi} \exp\left(\frac{\mathbf{f} I_k \cos\theta}{k_B T}\right) \sin\theta d\theta\right]^n}$$
$$= n I_k \frac{\int_0^{\pi} \exp\left(\frac{\mathbf{f} I_k \cos\theta}{k_B T}\right) \sin\theta \cos\theta d\theta}{\int_0^{\pi} \exp\left(\frac{\mathbf{f} I_k \cos\theta}{k_B T}\right) \sin\theta d\theta}. \tag{2.7}$$

The two integrals in (2.7) can be evaluated analytically. We first integrate the denominator,

$$\begin{aligned}\int_0^{\pi} \exp\left(\frac{\mathbf{f}I_k\cos\theta}{k_BT}\right)\sin\theta d\theta &= -\frac{k_BT}{\mathbf{f}I_k}\left[\exp\left(\frac{\mathbf{f}I_k\cos\pi}{k_BT}\right)-\exp\left(\frac{\mathbf{f}I_k\cos 0}{k_BT}\right)\right]\\ &= \frac{k_BT}{\mathbf{f}I_k}\left[\exp\left(\frac{\mathbf{f}I_k}{k_BT}\right)-\exp\left(-\frac{\mathbf{f}I_k}{k_BT}\right)\right]\\ &= \frac{2k_BT}{\mathbf{f}I_k}\sinh\left(\frac{\mathbf{f}I_k}{k_BT}\right). \end{aligned} \tag{2.8}$$

Then, by integrating by parts and applying the integral in (2.8), we compute the numerator of (2.7) as follows:

$$\begin{aligned}&\int_0^{\pi} \exp\left(\frac{\mathbf{f}I_k\cos\theta}{k_BT}\right)\sin\theta\cos\theta d\theta\\ &= -\frac{k_BT}{\mathbf{f}I_k}\left[\exp\left(\frac{\mathbf{f}I_k\cos\pi}{k_BT}\right)\cos\pi-\exp\left(\frac{\mathbf{f}I_k\cos 0}{k_BT}\right)\cos 0\right.\\ &\qquad\left.+\int_0^{\pi}\exp\left(\frac{\mathbf{f}I_k\cos\theta}{k_BT}\right)\sin\theta d\theta\right]\\ &= \frac{k_BT}{\mathbf{f}I_k}\left[\exp\left(\frac{\mathbf{f}I_k}{k_BT}\right)+\exp\left(-\frac{\mathbf{f}I_k}{k_BT}\right)-\int_0^{\pi}\exp\left(\frac{\mathbf{f}I_k\cos\theta}{k_BT}\right)\sin\theta d\theta\right]\\ &= \frac{k_BT}{\mathbf{f}I_k}\left[2\cosh\left(\frac{\mathbf{f}I_k}{k_BT}\right)-\frac{2k_BT}{\mathbf{f}I_k}\sinh\left(\frac{\mathbf{f}I_k}{k_BT}\right)\right]\\ &= \frac{2k_BT}{\mathbf{f}I_k}\left[\cosh\left(\frac{\mathbf{f}I_k}{k_BT}\right)-\frac{k_BT}{\mathbf{f}I_k}\sinh\left(\frac{\mathbf{f}I_k}{k_BT}\right)\right]. \end{aligned} \tag{2.9}$$

Finally, substituting (2.8) and (2.9) into (2.7), we obtain the following expression for the mean value of $\mathbf{z}$:

$$\langle\mathbf{z}\rangle = nI_k\left[\coth\left(\frac{\mathbf{f}I_k}{k_BT}\right)-\frac{k_BT}{\mathbf{f}I_k}\right]. \tag{2.10}$$

This yields the Langevin function (2.1) which describes the mean displacement of a single freely-jointed chain in the direction of the applied force.

The Langevin function (2.1) can be rewritten in a dimensionless form that expresses the fractional extension, i.e., the ratio of the chain extension to the contour length, as a function of the normalized force. Dividing (2.1) by the contour length of a polymer chain, nI_k, we have

$$\frac{\mathbf{z}}{nI_k} = \coth\left(\frac{\mathbf{f}I_k}{k_BT}\right) - \frac{k_BT}{\mathbf{f}I_k}. \tag{2.11}$$

As mentioned above, the force $\mathbf{f}$ measured in Newtons and the distance $\mathbf{z}$ measured in meters can be normalized to nondimensional quantities f and z respectively. The normalization is given by

$$\begin{aligned} f &= \frac{\mathbf{f}I_k}{k_BT}, \\ z &= \frac{\mathbf{z}}{I_k}, \end{aligned} \tag{2.12}$$

where I_k is the Kuhn length, k_B is the Boltzmann constant, and T is the temperature. Then we denote the nondimensional form of the Langevin function in (2.11) by

$$\frac{z}{n} = \coth f - \frac{1}{f} =: \mathcal{L}(f), \tag{2.13}$$

where z/n is the fractional extension. We will use only nondimensional quantities in this dissertation and omit the adjective "nondimensional" for brevity.

A graph of the classical Langevin function (2.13) is shown in Fig. 2.3. It features a sharp transition from the regime where very small force is sufficient to stretch the chain approaching its full length, to a blow up of the force along a vertical asymptote as the chain reaches its full length.

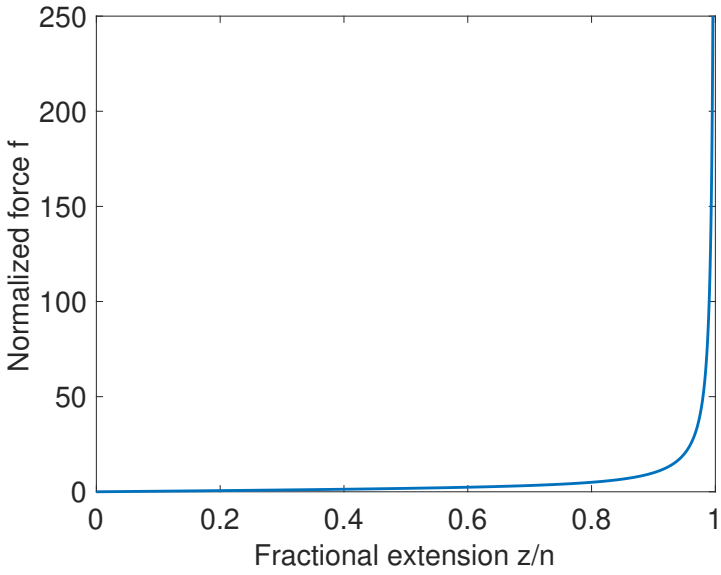

Figure 2.3: Normalized force f versus fractional extension z/n for the classical Langevin function (2.13).

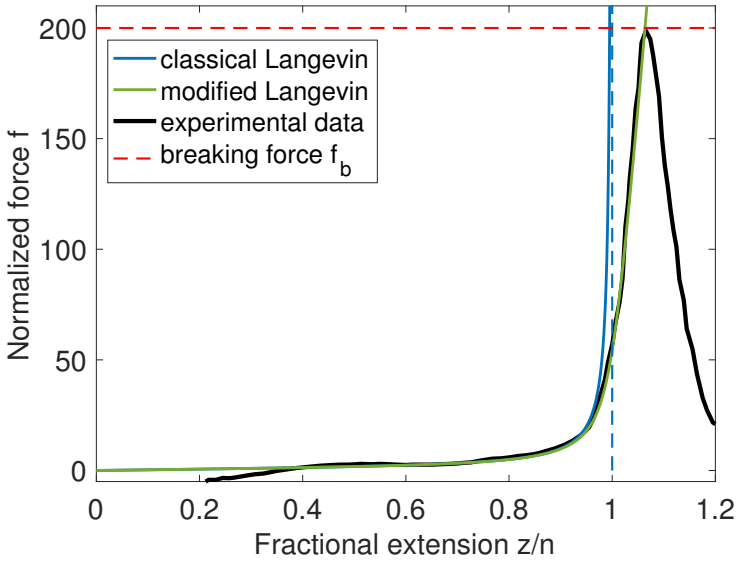

Figure 2.4: Normalized force f versus fractional extension z/n. Blue curve: classical Langevin function (2.13). Green curve: modified Langevin function defined in (2.15). Black graph: schematic of the experimental force-extension curve measured from stretching PNIPAM, for which $n = 676.47$, $I_k = 0.68$ nm, $T = 300$ K, and $K = 26000$ pN/nm [23].

2.2.2 The modified Langevin function

The classical Langevin function was modified to fit a measured force-extension curve for poly(N-isopropylacrylamide) (PNIPAM) in the experimental work [23]. As illustrated in Fig. 2.4, it was observed that the Langevin function (blue curve) did not match the experimental force-extension curve (black graph) in the high-force region [23]. Therefore, a modified Langevin function which allows Kuhn segments to deform under stress was used to fit the measured curve:

$$\mathbf{z}(\mathbf{f}) = \left(nI_k + \frac{n\mathbf{f}}{K}\right)\left[\coth\left(\frac{\mathbf{f}I_k}{k_BT}\right) - \frac{k_BT}{\mathbf{f}I_k}\right], \tag{2.14}$$

where K is the segment elasticity that characterizes the deformability of Kuhn segments. The nondimensional form of (2.14) is given by

$$\frac{z}{n} = \left(1 + \frac{fk_BT}{KI_k^2}\right)\mathcal{L}(f), \tag{2.15}$$

where $\mathcal{L}(f)$ is the Langevin function defined in (2.13).

A graph of the modified Langevin function (2.15) is plotted in Fig. 2.4 (green curve). It shows a good match to the experimental force-extension curve measured from stretching PNIPAM chains, with $n = 676.47$, $I_k = 0.68$ nm, $T = 300$ K, and $K = 26000$ pN/nm [23]. A schematic of the experimental force-extension curve is shown in Fig. 2.4 (black graph). The breaking force measured in [23] is normalized to $f_b = 200$. We prescribe this normalized breaking force f_b on polymer chains in our models.

We remark that the classical Langevin function (2.13) and the modified Langevin function (2.15) both give a zero chain extension at zero force. This can be easily seen from the derivation of the Langevin function by Kuhn and Grün [22]: if there is no pulling force, the distribution of the extension of the chain is isotropic, and the mean displacement is hence zero. However, it is well-known that the equilibrium length of a freely-jointed chain of n Kuhn segments takes the root-mean-square value, $\sqrt{n}I_k$, by considering the chain as a random walk of n steps of length I_k. Taking this fact into account, the design of appropriate stress-stretch relationships is needed.

2.3 Root-mean-square deviation

In this section, we derive the root-mean-square (RMS) deviation of a freely-jointed chain for two distances: the end-to-end distance and the displacement in the direction of the force. Both of them achieve a nonzero chain length at zero force. Note that the root-mean-square (RMS) deviation is a stretch-stress relationship, expressing stretch as a function of stress. We further design a close approximation for the inversion.

We consider the following three-dimensional model for a freely-jointed chain consisting of n Kuhn segments (see Fig. 2.5). The chain is represented by a sequence of points $\{(x_j, y_j, z_j)\}_{j=0}^{n}$ where neighboring points (x_j, y_j, z_j) and $(x_{j+1}, y_{j+1}, z_{j+1})$ are joined by links of length $I_k = 1$. One end of the chain (x_0, y_0, z_0) is fixed at the origin while the other end (x_n, y_n, z_n) is pulled by a constant force f along the direction of the z-axis. The orientation of each link is specified by the two angles θ and φ described in Section 2.2.1.

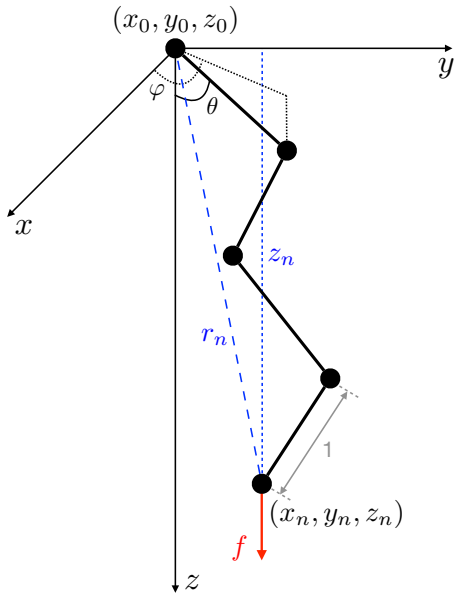

Figure 2.5: Three-dimensional model for a freely-jointed chain of n Kuhn segments.

Let r_n be the end-to-end distance of the chain, i.e.,

$$r_n = \|(x_n, y_n, z_n) - (x_0, y_0, z_0)\|_2 = \sqrt{x_n^2 + y_n^2 + z_n^2}, \tag{2.16}$$

and z_n corresponds to the displacement of the chain in the direction of the pulling force f, as illustrated in Fig. 2.5. We denote the root-mean-square values of these two distances by $r_{\text{RMS}} := \langle r_n^2 \rangle^{\frac{1}{2}}$ and $z_{\text{RMS}} := \langle z_n^2 \rangle^{\frac{1}{2}}$ respectively.

As discussed in Section 2.2.1, the mean value of a quantity is defined by (2.2), which is a weighted sum over all microstates. The probability density function (PDF) of a microstate is given by (2.3) and (2.4). We write the free end of the chain in terms of the angles $\{(\theta_j, \varphi_j)\}$, $j = 1, 2, ..., n$, by using the spherical coordinates:

$$(x_n, y_n, z_n) = \sum_{j=1}^{n} (\sin\theta_j \cos\varphi_j, \sin\theta_j \sin\varphi_j, \cos\theta_j). \tag{2.17}$$

The angles $\{\varphi_j\}_{j=1}^n$ are independent and uniformly distributed on $[0, 2\pi]$. The other angles $\{\theta_j\}_{j=1}^n$ are also independent and distributed on $[0, \pi]$ according to the following PDF:

$$p(\theta) = \frac{\exp(f\cos\theta)\sin\theta}{\int_0^\pi \exp(f\cos\theta)\sin\theta d\theta}, \quad 0 \le \theta \le \pi, \tag{2.18}$$

where f is the normalized force. The joint PDF of two independent angles θ_j and θ_k $(j \neq k)$ is the product, $p(\theta_j, \theta_k) = p(\theta_j)p(\theta_k)$.

Here we provide a brief summary of the main results. The expression for the RMS end-to-end distance is given by

$$r_{\text{RMS}} = \sqrt{n + (n^2 - n)[\mathcal{L}(f)]^2}, \tag{2.19}$$

where $\mathcal{L}(f)$ is the Langevin function defined in (2.13). In the absence of the force f, the equilibrium chain length is $r_0 = \sqrt{n}$ since $\mathcal{L}(f)$ approaches 0 as $f \to 0$. This agrees with the random walk consideration mentioned in Section 2.2.2. The derivation of (2.19) is detailed in Section 2.3.1. The RMS deviation for the displacement in the direction of the force takes the following form:

$$z_{\text{RMS}} = \sqrt{n\left[1 - \frac{2\mathcal{L}(f)}{f}\right] + (n^2 - n)[\mathcal{L}(f)]^2}. \tag{2.20}$$

At zero force, we obtain the initial displacement in the z-direction,

$$z_0 = \sqrt{\frac{n}{3}}. \tag{2.21}$$

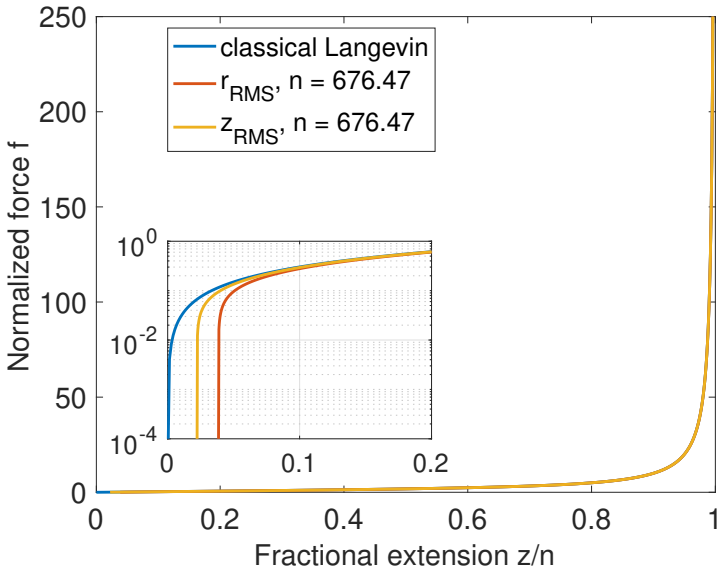

Figure 2.6: Normalized force f versus fractional extension z/n. Blue curve: classical Langevin function (2.13). Red curve: r_{RMS} given by (2.19) for $n = 676.47$. Yellow curve: z_{RMS} given by (2.20) for the same n. The inset shows the different behavior of three curves when the force is near zero.

Details for the derivation of (2.20) and (2.21) are given in Section 2.3.2. We also calculated the mean value of the absolute displacement in the direction of the force, $\langle |z_n| \rangle$, but derived only an upper bound for this quantity. Graphs of the two RMS deviations, r_{RMS} and z_{RMS}, are shown in Fig. 2.6. Here the number of Kuhn segments is taken from the measurement of PNIPAM in [23], $n = 676.47$. It can be seen that both curves agree well with the classical Langevin function except when the force is near zero. The inset shows the discrepancy near the equilibrium length.

In this work, we employ the RMS displacement in the direction of the force, z_{RMS}, as the force-extension curve for a polymer chain. Moreover, we design another J-shaped force-extension curve by modifying z_{RMS} with a stiffness near rupture, in the same manner

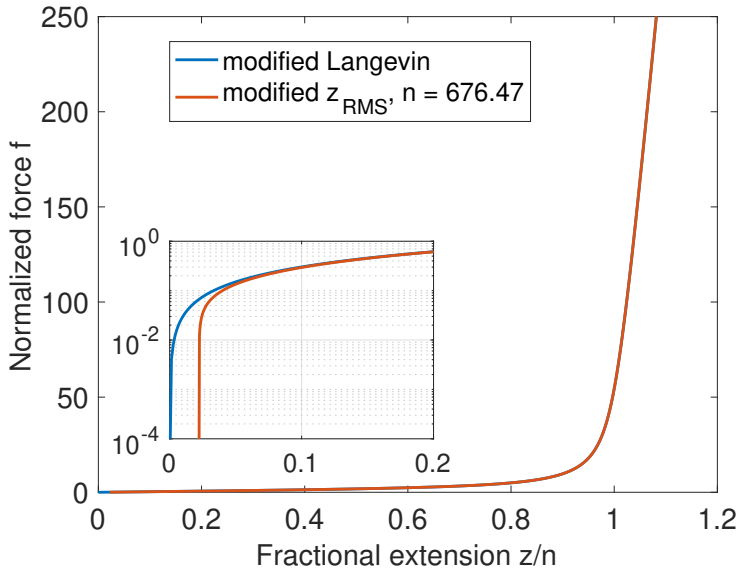

Figure 2.7: Normalized force f versus fractional extension z/n. Blue curve: modified Langevin function (2.15). Red curve: modified z_{RMS} given by (2.22) for $n = 676.47$. The inset shows the different behavior of two curves near the zero force.

as the modified Langevin function (2.15):

$$\text{modified } z_{\text{RMS}} = \left(1 + \frac{f k_B T}{K I_k^2}\right) \sqrt{n\left[1 - \frac{2\mathcal{L}(f)}{f}\right] + (n^2 - n)[\mathcal{L}(f)]^2}. \tag{2.22}$$

A graph of the modified z_{RMS} for $n = 676.47$ is shown in Fig. 2.7 (red curve). Its behavior resembles the modified Langevin function but admits a nonzero equilibrium length (2.21).

2.3.1 Derivation of the root-mean-square distance

We consider a freely-jointed chain of n Kuhn segments, each with link length 1, as shown in Fig. 2.5. The root-mean-square (RMS) end-to-end distance is defined by

$$r_{\text{RMS}} := (\mathbb{E}[r_n^2])^{\frac{1}{2}} = (\mathbb{E}[x_n^2 + y_n^2 + z_n^2])^{\frac{1}{2}}, \tag{2.23}$$

where (x_n, y_n, z_n) is the free end of the chain that is pulled by a constant force f along the z-axis. The endpoint (x_n, y_n, z_n) can be expressed as (2.17) using the spherical coordinates. We compute $\mathbb{E}[r_n^2]$ in terms of the angles $\{(\theta_j, \varphi_j)\}$, $j = 1, 2, ..., n$:

$$\begin{aligned}\mathbb{E}[r_n^2] &= \mathbb{E}\left[\left(\sum_{j=1}^{n} \sin\theta_j \cos\varphi_j\right)^2 + \left(\sum_{j=1}^{n} \sin\theta_j \sin\varphi_j\right)^2 + \left(\sum_{j=1}^{n} \cos\theta_j\right)^2\right] \\ &= \mathbb{E}\left[\sum_{j=1}^{n} (\sin\theta_j \cos\varphi_j)^2 + 2\sum_{j<k} \sin\theta_j \cos\varphi_j \sin\theta_k \cos\varphi_k + \sum_{j=1}^{n} (\sin\theta_j \sin\varphi_j)^2 \right. \\ &\quad \left. + 2\sum_{j<k} \sin\theta_j \sin\varphi_j \sin\theta_k \sin\varphi_k + \sum_{j=1}^{n} (\cos\theta_j)^2 + 2\sum_{j<k} \cos\theta_j \cos\theta_k\right]. \end{aligned} \tag{2.24}$$

The probability density function (PDF) of angles $\{\theta_j\}_{j=1}^n$, $p(\theta)$, is given by (2.18), and angles $\{\varphi_j\}_{j=1}^n$ are uniformly distributed on $[0, 2\pi]$. Note that the joint PDF of two independent angles θ_j and θ_k $(j \neq k)$ is the product, $p(\theta_j, \theta_k) = p(\theta_j)p(\theta_k)$.

We first compute the two cross terms in (2.24), i.e. $\mathbb{E}[\sin\theta_j \cos\varphi_j \sin\theta_k \cos\varphi_k]$ and $\mathbb{E}[\sin\theta_j \sin\varphi_j \sin\theta_k \sin\varphi_k]$. Since all the angles are independent, it follows that

$$\mathbb{E}[\sin\theta_j \cos\varphi_j \sin\theta_k \cos\varphi_k] = \mathbb{E}[\sin\theta_j]\mathbb{E}[\cos\varphi_j]\mathbb{E}[\sin\theta_k]\mathbb{E}[\cos\varphi_k],$$

$$\mathbb{E}[\sin\theta_j \sin\varphi_j \sin\theta_k \sin\varphi_k] = \mathbb{E}[\sin\theta_j]\mathbb{E}[\sin\varphi_j]\mathbb{E}[\sin\theta_k]\mathbb{E}[\sin\varphi_k].$$

It can be easily seen that

$$\mathbb{E}[\cos\varphi] = \frac{1}{2\pi}\int_0^{2\pi} \cos\varphi d\varphi = 0,$$
$$\mathbb{E}[\sin\varphi] = \frac{1}{2\pi}\int_0^{2\pi} \sin\varphi d\varphi = 0,$$

where φ has a uniform distribution on $[0, 2\pi]$. Hence the two cross terms would vanish. The expectation in (2.24) can then be simplified,

$$\begin{aligned}
&\mathbb{E}[r_n^2] \\
&= \mathbb{E}\left[\sum_{j=1}^{n}(\sin\theta_j\cos\varphi_j)^2 + \sum_{j=1}^{n}(\sin\theta_j\sin\varphi_j)^2 + \sum_{j=1}^{n}(\cos\theta_j)^2 + 2\sum_{j<k}\cos\theta_j\cos\theta_k\right] \\
&= n\left(\mathbb{E}\left[(\sin\theta\cos\varphi)^2\right] + \mathbb{E}\left[(\sin\theta\sin\varphi)^2\right] + \mathbb{E}\left[\cos^2\theta\right]\right) + 2\sum_{j<k}\mathbb{E}[\cos\theta_j\cos\theta_k]. \qquad (2.25)
\end{aligned}$$

We compute each of the four expectations in (2.25) as follows.

$$\begin{aligned}
\mathbb{E}\left[(\sin\theta\cos\varphi)^2\right] &= \mathbb{E}\left[\sin^2\theta\right]\mathbb{E}\left[\cos^2\varphi\right] \\
&= \frac{\int_0^\pi \exp(f\cos\theta)\sin^3\theta d\theta \int_0^{2\pi}\cos^2\varphi d\varphi}{2\pi\int_0^\pi \exp(f\cos\theta)\sin\theta d\theta} \\
&= \frac{\int_0^\pi \exp(f\cos\theta)\sin^3\theta d\theta}{2\int_0^\pi \exp(f\cos\theta)\sin\theta d\theta}. \qquad (2.26)
\end{aligned}$$

$$\begin{aligned}
\mathbb{E}\left[(\sin\theta\sin\varphi)^2\right] &= \mathbb{E}\left[\sin^2\theta\right]\mathbb{E}\left[\sin^2\varphi\right] \\
&= \frac{\int_0^\pi \exp(f\cos\theta)\sin^3\theta d\theta \int_0^{2\pi}\sin^2\varphi d\varphi}{2\pi\int_0^\pi \exp(f\cos\theta)\sin\theta d\theta} \\
&= \frac{\int_0^\pi \exp(f\cos\theta)\sin^3\theta d\theta}{2\int_0^\pi \exp(f\cos\theta)\sin\theta d\theta}. \qquad (2.27)
\end{aligned}$$

$$\mathbb{E}\left[\cos^2\theta\right] = \frac{\int_0^\pi \exp(f\cos\theta)\sin\theta\cos^2\theta d\theta}{\int_0^\pi \exp(f\cos\theta)\sin\theta d\theta}. \qquad (2.28)$$

The following fact is used in (2.26) and (2.27),

$$\int_0^{2\pi} \cos^2\varphi d\varphi = \int_0^{2\pi} \sin^2\varphi d\varphi = \pi.$$

The sum of the three expectations above yields

$$\begin{aligned}
&\mathbb{E}\left[(\sin\theta\cos\varphi)^2\right] + \mathbb{E}\left[(\sin\theta\sin\varphi)^2\right] + \mathbb{E}\left[\cos^2\theta\right] \\
&= \frac{\int_0^\pi \exp(f\cos\theta)\sin\theta\left(\sin^2\theta + \cos^2\theta\right)d\theta}{\int_0^\pi \exp(f\cos\theta)\sin\theta d\theta} \\
&= 1.
\end{aligned} \tag{2.29}$$

It remains to compute the last expectation in (2.25),

$$\begin{aligned}
\mathbb{E}[\cos\theta_j\cos\theta_k] &= \mathbb{E}[\cos\theta_j]\mathbb{E}[\cos\theta_k] \\
&= (\mathbb{E}[\cos\theta])^2 \\
&= \left(\frac{\int_0^\pi \exp(f\cos\theta)\sin\theta\cos\theta d\theta}{\int_0^\pi \exp(f\cos\theta)\sin\theta d\theta}\right)^2,
\end{aligned} \tag{2.30}$$

where θ_j and θ_k are replaced with θ since they are independent. The two integrals in (2.30) have been computed in Section 2.2.1, i.e., we normalize the force $\mathbf{f}$ to the nondimensional force f in (2.8) and (2.9):

$$\begin{aligned}
\int_0^\pi \exp(f\cos\theta)\sin\theta d\theta &= \frac{2\sinh f}{f}, \\
\int_0^\pi \exp(f\cos\theta)\sin\theta\cos\theta d\theta &= \frac{2}{f}\left(\cosh f - \frac{\sinh f}{f}\right).
\end{aligned}$$

Their ratio yields the Langevin function

$$\frac{\int_0^\pi \exp(f\cos\theta)\sin\theta\cos\theta d\theta}{\int_0^\pi \exp(f\cos\theta)\sin\theta d\theta} = \coth f - \frac{1}{f} =: \mathcal{L}(f). \tag{2.31}$$

Therefore, we obtain the following expression for $\mathbb{E}[r_n^2]$:

$$\begin{aligned}\mathbb{E}[r_n^2] &= n + 2\sum_{j<k}[\mathcal{L}(f)]^2 \\ &= n + (n^2 - n)[\mathcal{L}(f)]^2.\end{aligned} \tag{2.32}$$

Taking the square root of $\mathbb{E}[r_n^2]$ gives r_{RMS} in (2.19).

We remark on the limiting behavior of r_{RMS}. Note that the Taylor expansion of the Langevin function is

$$\coth x - \frac{1}{x} = \frac{x}{3} - \frac{x^3}{45} + \frac{2x^5}{945} - \frac{x^7}{4725} + \cdots, \quad |x| < \pi. \tag{2.33}$$

This gives

$$\lim_{f\to 0}\mathcal{L}(f) = 0. \tag{2.34}$$

When there is no pulling force ($f = 0$), the equilibrium length of a polymer chain assumes the root-mean-square value,

$$r_0 = \sqrt{n}. \tag{2.35}$$

When the force is very large ($f \to \infty$), $\mathcal{L}(f)$ approaches 1 and the chain will be nearly vertical, approaching its contour length n.

2.3.2 Derivation of the root-mean-square displacement

We consider the same setting for a freely-jointed chain as in the previous section. The root-mean-square (RMS) displacement in the direction of the force is defined by

$$z_{\mathrm{RMS}} := (\mathbb{E}[z_n^2])^{\frac{1}{2}}, \tag{2.36}$$

where z_n is the displacement of the chain along the direction of the z-axis (see Fig. 2.5). By using the spherical coordinates, $\mathbb{E}[z_n^2]$ can be written as

$$\begin{aligned}
\mathbb{E}[z_n^2] &= \mathbb{E}\left[\left(\sum_{j=1}^{n}\cos\theta_j\right)^2\right] \\
&= \mathbb{E}\left[\sum_{j=1}^{n}(\cos\theta_j)^2 + 2\sum_{j<k}\cos\theta_j\cos\theta_k\right] \\
&= n\mathbb{E}\left[\cos^2\theta\right] + 2\sum_{j<k}\mathbb{E}[\cos\theta_j\cos\theta_k].
\end{aligned} \tag{2.37}$$

The two expectations in (2.37) have been computed in Section 2.3.1. The cross term $\mathbb{E}[\cos\theta_j\cos\theta_k]$ is given by (2.30) and (2.31), i.e.,

$$\mathbb{E}[\cos\theta_j\cos\theta_k] = [\mathcal{L}(f)]^2, \tag{2.38}$$

where $\mathcal{L}(f)$ is the Langevin function defined in (2.13). The other expectation $\mathbb{E}\left[\cos^2\theta\right]$ is given by (2.28), i.e.,

$$\mathbb{E}\left[\cos^2\theta\right] = \frac{\int_0^\pi \exp(f\cos\theta)\sin\theta\cos^2\theta d\theta}{\int_0^\pi \exp(f\cos\theta)\sin\theta d\theta},$$

but it remains to evaluate the two integrals in it.

The denominator of (2.28) has been computed in Section 2.2.1, i.e.,

$$\int_0^\pi \exp(f\cos\theta)\sin\theta d\theta = \frac{2\sinh f}{f}. \tag{2.39}$$

We recall another integral computed in Section 2.2.1 which will be used in evaluating the numerator of (2.28),

$$\int_0^\pi \exp(f\cos\theta)\sin\theta\cos\theta d\theta = \frac{2}{f}\left(\cosh f - \frac{\sinh f}{f}\right).$$

Then we compute the numerator of (2.28) by integrating by parts:

$$\begin{aligned}
&\int_0^\pi \exp(f\cos\theta)\sin\theta\cos^2\theta d\theta \\
&= -\frac{1}{f}\left[\exp(f\cos\pi)\cos^2\pi - \exp(f\cos 0)\cos^2 0 + 2\int_0^\pi \exp(f\cos\theta)\sin\theta\cos\theta d\theta\right] \\
&= \frac{2}{f}\left[\sinh f - \frac{2}{f}\left(\cosh f - \frac{\sinh f}{f}\right)\right].
\end{aligned} \tag{2.40}$$

Dividing (2.40) by (2.39), we obtain

$$\mathbb{E}\left[\cos^2\theta\right] = 1 - \frac{2}{f}\left(\coth f - \frac{1}{f}\right) = 1 - \frac{2\mathcal{L}(f)}{f}, \tag{2.41}$$

where $\mathcal{L}(f)$ is the Langevin function (2.13). Finally, substituting (2.38) and (2.41) into

(2.37), we obtain the following expression for $\mathbb{E}[z_n^2]$:

$$\begin{aligned}\mathbb{E}[z_n^2] &= n\left[1 - \frac{2\mathcal{L}(f)}{f}\right] + 2\sum_{j<k}[\mathcal{L}(f)]^2 \\ &= n\left[1 - \frac{2\mathcal{L}(f)}{f}\right] + (n^2 - n)[\mathcal{L}(f)]^2. \end{aligned} \tag{2.42}$$

Taking the square root of $\mathbb{E}[z_n^2]$ gives z_{RMS} in (2.20).

In the limit of zero force, we derive the initial displacement in the direction of the force. We have shown that the Langevin function $\mathcal{L}(f)$ approaches 0 as the force $f \to 0$. The limiting behavior of $\mathcal{L}(f)/f$ as $f \to 0$ can be determined in the same way. It follows from the Taylor expansion (2.33) that

$$\frac{\mathcal{L}(x)}{x} = \frac{1}{3} - \frac{x^2}{45} + \frac{2x^4}{945} - \frac{x^6}{4725} + \cdots, \quad |x| < \pi. \tag{2.43}$$

This gives

$$\lim_{f\to 0} \frac{\mathcal{L}(f)}{f} = \frac{1}{3}. \tag{2.44}$$

By letting $f \to 0$ in (2.42) and taking the square root, the initial displacement in the direction of the force obtained from z_{RMS} is

$$z_0 = \sqrt{\frac{n}{3}}. \tag{2.45}$$

Moreover, it can be easily checked that z_{RMS} approaches the contour length n in the limit of $f \to \infty$. That is, the n Kuhn segments are aligned nearly vertically when the force is very large.

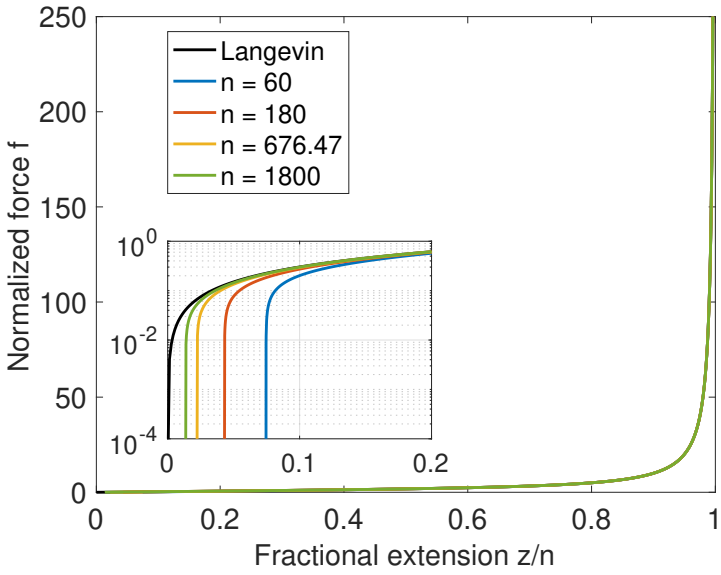

Figure 2.8: Normalized force f versus fractional extension z/n. Black curve: classical Langevin function (2.13). Colored curves: graphs of z_{RMS} given by (2.20) for various values of n. The inset shows that the behavior of z_{RMS} near the equilibrium length approaches the Langevin function as n increases.

2.3.3 Inversion and approximation

The two J-shaped force-extension curves described above, z_{RMS} and modified z_{RMS}, express the displacement of a polymer chain as a function of the applied pulling force f. Inversion of these RMS displacements is needed to obtain stress-stretch relationships of the form $f = f(z, n)$ where n is the number of Kuhn segments per chain.

We take the inversion of z_{RMS} for illustration. The behavior of (2.20) approaches the Langevin function $z/n = \mathcal{L}(f)$ for sufficiently large n, see Fig. 2.8. We thus seek to find the inversion of z_{RMS} using the inverse Langevin function $f = \mathcal{L}^{-1}\left(\frac{z}{n}\right)$. However, the inverse Langevin function cannot be represented in a closed form. It can only be found by numerically solving the inverse problem or making approximations. The numerical method is not commonly used in practice because it is inapplicable for further analytical

studies. A more practical solution is to find a simple and highly accurate approximant. Existing standard approximations of the inverse Langevin function are summarized in [32]. These approximants generally take two forms: Taylor series expansion and rational (Padé) approximation. The Taylor series is not a good option since it converges slowly near the singular point. We choose the most popular Padé approximation [3/2] given by Cohen [33],

$$\mathcal{L}^{-1}(y) = y\frac{3 - \frac{36}{35}y^2}{1 - \frac{33}{35}y^2}, \tag{2.46}$$

which is referred to as the Cohen approximation.

We then devise a close approximation for the inversion of z_{RMS} based on the Cohen approximation above. As seen in Fig. 2.8, the characteristic of the J-shaped force-extension curve is that the force is low for a large range of extension when the chain is not fully stretched (i.e. entropic regime), and grows steeply to a blow up only within a small range of extension (i.e. energetic regime). We prescribe a constant breaking force f_b on the chain to represent the strength of covalent bonds. If the force on a chain exceeds f_b, the chain breaks and the force drops down to zero. We set $f_b = 200$ which is measured from breaking a single PNIPAM chain [23]. Moreover, we divide the entropic regime (i.e. low-force region) into two subphases: phase 1 where the force is almost zero, and phase 2 where the force starts to grow fast but is still much below the breaking force f_b. An illustration for the division of entropic regime 1, entropic regime 2, and energetic regime is shown in Fig. 2.9. The upper bounds of the force in entropic regimes are denoted by f_{e_1} and f_{e_2} respectively. Their values are to be determined by the recipe below. Different approximations for the inversion of z_{RMS} in the three regimes of force growing are designed as follows.

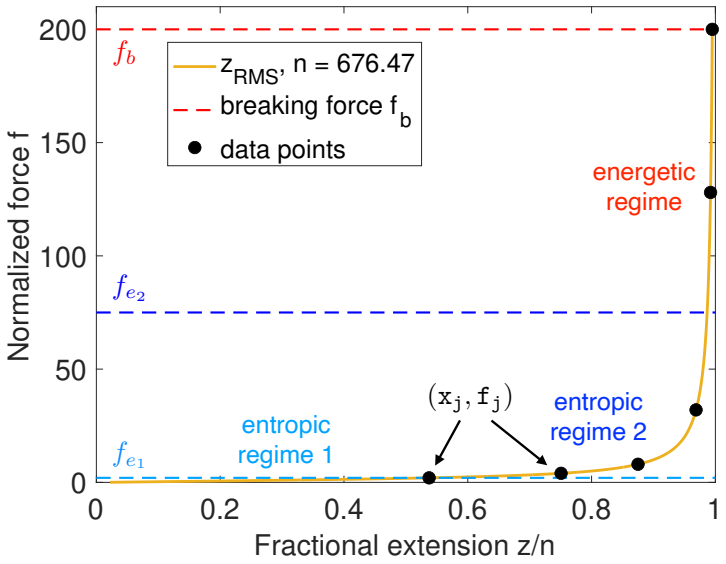

Figure 2.9: An illustration for the three regimes of force growing along the curve of z_{RMS}. The breaking force is $f_b = 200$ [23]. Yellow curve: z_{RMS} given by (2.20) for $n = 676.47$. Black dots: data points $\{(\mathtt{x_j}, \mathtt{f_j})\}_{\mathtt{j=1}}^{\mathtt{6}}$ used to construct the rational interpolation of the form (2.49) in entropic regime 2.

- **Entropic regime 1:** $0 < f < f_{e_1}$, where f_{e_1} is close to 0. As we have mentioned, the Cohen approximation (2.46) has high accuracy for $y \in [0, 0.66]$ where the force is almost zero. The force is zero at zero extension of the chain, $\mathcal{L}^{-1}(0) = 0$. Recall that for a polymer chain of n Kuhn segments, the initial displacement in the direction of the force obtained from z_{RMS} takes the root-mean-square value, $z_0 = \sqrt{\frac{n}{3}}$. To match this nonzero equilibrium length, we construct the approximation $f_1(z, n)$ by slightly shifting down the Cohen formula:

$$f_1(z, n) = \mathcal{L}^{-1}\left(\frac{z}{n}\right) - \mathcal{L}^{-1}\left(\frac{z_0}{n}\right), \tag{2.47}$$

where $\mathcal{L}^{-1}(\cdot)$ is given by (2.46).

- **Entropic regime 2:** $f_{e_1} < f < f_{e_2}$, where f_{e_2} is much below the breaking force f_b. The Cohen approximation is less accurate as f grows faster. Motivated by this Padé approximant of order [3/2], we approximate the inversion of z_{RMS} with a rational function of the same order. Note that the curves of z_{RMS} for different values of n, where the force f is plotted as a function of the fractional extension z/n, almost coincide with each other in this regime (see Fig. 2.8). Thus the approximation $f_2(z, n)$ is assumed to depend only on the ratio z/n:

$$f_2(z, n) = R\left(\frac{z}{n}\right), \tag{2.48}$$

where $R(\cdot)$ is a rational function of the form

$$R(x) = \frac{a_0 + a_1 x + a_2 x^2 + a_3 x^3}{1 + b_1 x + b_2 x^2}. \tag{2.49}$$

The coefficients a_i and b_i are determined by interpolating 6 data points $(\mathtt{x_j}, \mathtt{f_j})$ on the graph of z_{RMS}, as illustrated in Fig. 2.9. Here $\mathtt{x_j}$ and $\mathtt{f_j}$ denote the fractional extension and the normalized force, respectively. The data points are chosen to be denser in the low-force region such that the characteristic J-shaped curve is better fitted. We solve the following linear system for the unknowns a_i and b_i,

$$a_0 + a_1\mathtt{x_j} + a_2\mathtt{x_j}^2 + a_3\mathtt{x_j}^3 - b_1\mathtt{f_j}\mathtt{x_j} - b_2\mathtt{f_j}\mathtt{x_j}^2 = \mathtt{f_j}, \quad \mathtt{j} = 1, ..., 6. \tag{2.50}$$

An example of the rational interpolant for z_{RMS}, including the location of data points and the values of coefficients, will be provided later in this section (Table 2.1).

- **Energetic regime:** $f_{e_2} < f < f_b$, where $f_b = 200$ is the normalized breaking force. The rapid growth of the energetic force is nearly linear for a narrow range of chain extension. To reduce computational cost, we approximate the force-extension curve in this regime by a linear segment between points (x_{e_2}, f_{e_2}) and (x_b, f_b):

$$f_3(z, n) = \frac{f_b - f_{e_2}}{x_b - x_{e_2}} \left(\frac{z}{n} - x_b \right) + f_b, \tag{2.51}$$

where x_{e_2} and x_b denote the fractional extension at two endpoints.

Finally, a piecewise smooth approximation $f(z, n)$ is obtained by joining the above three branches given by (2.47), (2.48) and (2.51). The upper bounds f_{e_1} and f_{e_2} are determined by forces at intersections of neighboring curves. A graph of $f(z, n)$ which closely approximates the inversion of z_{RMS} for $n = 676.47$ [23] is plotted in Fig. 2.10(a). Another approximation for the inversion of modified z_{RMS} follows the same manner and is shown in Fig. 2.10(b). Details for the construction of these two approximations are given in Table 2.1.

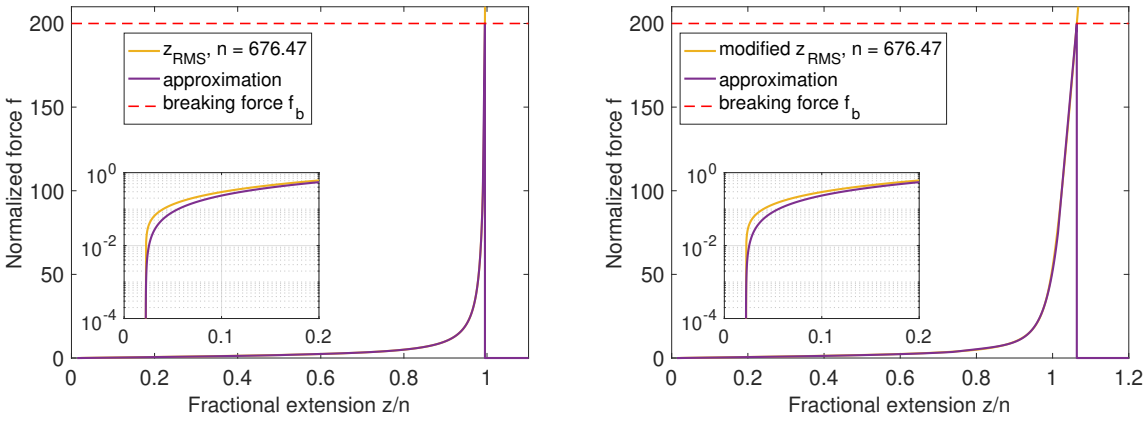

Figure 2.10: Close approximations for the inversion of two RMS displacements: (a) z_{RMS} given by (2.20) and (b) modified z_{RMS} given by (2.22). The number of Kuhn segments is $n = 676.47$, the measurement of PNIPAM in [23]. The breaking force is $f_b = 200$.

Table 2.1: The construction of the piecewise approximation $f(z,n)$ for the inversion of two RMS displacements, z_{RMS} and modified z_{RMS}, where $n = 676.47$ [23].

	z_{RMS}	modified z_{RMS}
$f_1(z,n)$	$0 < z/n < 0.503$ $0 < f < 1.742$	$0 < z/n < 0.737$ $0 < f < 3.624$
$f_2(z,n)$	$0.503 < z/n < 0.990$ $1.742 < f < 100$ Coefficients: $a_0 = 1.283,\ a_1 = -3.314,$ $a_2 = 0.954,\ a_3 = -0.337,$ $b_1 = -3.415,\ b_2 = 2.415.$	$0.737 < z/n < 1.014$ $3.624 < f < 74.96$ Coefficients: $a_0 = -24.73,\ a_1 = 91.32,$ $a_2 = -109.9,\ a_3 = 43.62,$ $b_1 = -1.879,\ b_2 = 0.885.$
$f_3(z,n)$	$0.990 < z/n < 0.995$ $100 < f < 200$ Slope: $\dfrac{f_b - f_{e_2}}{x_b - x_{e_2}} = 2.000 \times 10^4$	$1.014 < z/n < 1.064$ $74.96 < f < 200$ Slope: $\dfrac{f_b - f_{e_2}}{x_b - x_{e_2}} = 2.536 \times 10^3$
Data points $\{(\mathtt{x_j}, \mathtt{f_j})\}_{\mathtt{j=1}}^{\mathtt{6}}$	$(0.538, 2)$ $(0.969, 32)$ $(0.751, 4)$ $(0.992, 128)$ $(0.875, 8)$ $(0.995, 200)$	$(0.752, 4)$ $(0.979, 32)$ $(0.877, 8)$ $(1.036, 128)$ $(0.943, 16)$ $(1.064, 200)$

2.4 Length distribution for polymer chains

A real polymer network consists of polymer chains of different lengths. Coexistent in the network are short chains, long chains, and dangling chains. A recent experimental work [10] points out that network imperfection, i.e., scatter in lengths of polymer chains that constitute the network, profoundly affects the mechanical properties of polymer materials. The key finding of this work shows that the ultimate properties (strength, extensibility, and work of fracture) of hydrogels have narrow scatter from sample to sample, but are orders of magnitude lower than those of a perfect network. Recall that the covalent bond force for a single chain is on the level of 10^{-9} N, which is about two orders of magnitude greater than the entropic force (on the level of 10^{-11} N). However, the experimental strength of a polymer network is measured within the entropic regime. This indicates that when the network is stretched near rupture, only a small fraction of polymer chains are stressed to the covalent bond strength, and other chains still carry entropic forces. Hence the load per chain is small.

The distribution of chain lengths has been incorporated into the mechanics models which study various aspects of J-shaped stress-stretch relationships [24–26]. Due to this characteristic shape of the force-extension curve, chains with fewer links attain the breaking force and rupture at smaller extensions, while chains with more links still have very low forces that are almost zero. As a result, the average force per chain at rupture is in the entropic regime of the force-extension curve. This explains the observed phenomenon that the measured strength of a polymer network is entropic, although the breaking force for an individual chain is energetic.

In this work, we introduce the scatter in chain lengths by assuming a statistical distribution for the number of Kuhn segments per chain, n. Chains of different lengths will carry different tensile forces under the same macroscopic deformation, which enables the large reduction in strength. The distribution of chain lengths in a polymer network has been rarely measured. It has been estimated from the following experiment. For a polymer network of chemiluminescent crosslinks, which emit light upon rupture, the intensity of luminescence is measured as a function of the stretch of the polymer network [18]. Assuming that all chains have the same stretch, the distribution of chain lengths is proportional to the intensity of luminescence [28]. Estimated by this method, the chain length distribution in a polymer network is found to be similar to the Weibull distribution, as shown in Fig. 2.11. The Weibull distribution has an analytical form with well-studied statistical characteristics, which gives a reasonable choice for scattering the number of Kuhn segments per chain, n. Below we remind basic facts about the Weibull distribution.

2.4.1 The Weibull distribution

Let n be the number of Kuhn segments per chain. The Weibull distribution has the probability density function (PDF)

$$p(n; m, n_0) = \begin{cases} \frac{m}{n_0} \left(\frac{n}{n_0}\right)^{m-1} \exp\left[-\left(\frac{n}{n_0}\right)^m\right], & n \geq 0, \\ 0, & n < 0. \end{cases} \tag{2.52}$$

The parameters $m > 0$ and $n_0 > 0$ describe, respectively, the shape and the scale of the Weibull distribution (see Fig. 2.12(a)). The form of the Weibull PDF changes drastically

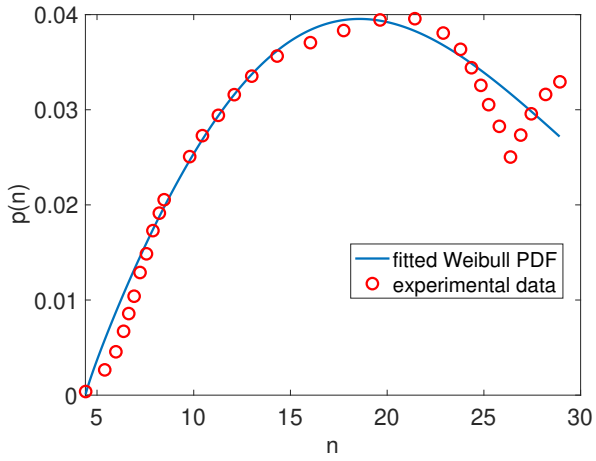

Figure 2.11: Fitting a shifted Weibull distribution to the chain length distribution which is estimated from light emission [18,28]. The size of the shift is 4.4 Kuhn segments per chain. The fit is obtained with the shape parameter $m = 1.9$ and the scale parameter $n_0 = 21$. The dip in the data occurs because three unload-reload cycles are performed at this point before the stretch is further increased.

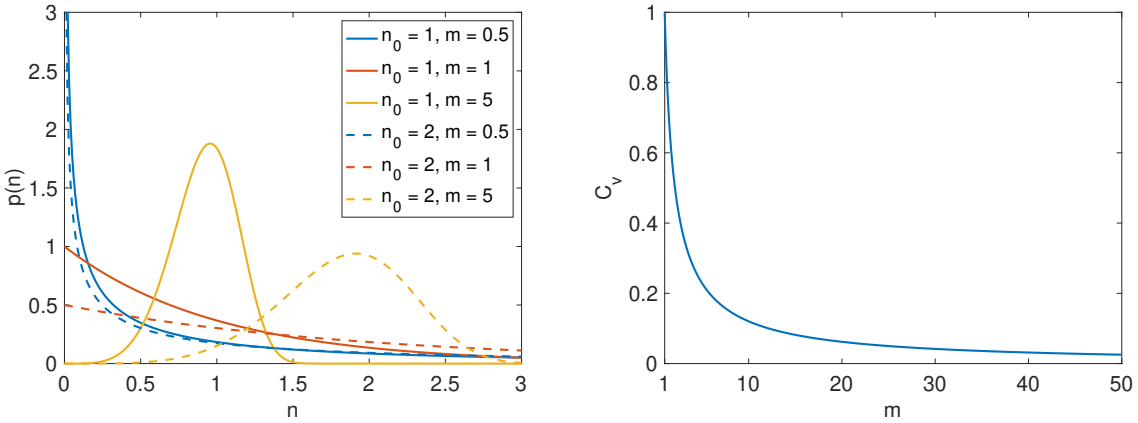

(a) (b)

Figure 2.12: The Weibull distribution is characterized by the scale parameter n_0 and the shape parameter m. (a): Probability density function (PDF). (b): The coefficient of variation, $C_v = \sigma/\mu$, as a function of the shape parameter m.

with the value of the shape parameter, m. For $m = 1$, the Weibull distribution reduces to the exponential distribution. In this study, we restrict the shape parameter in the range $1 \leq m < \infty$. For the chain length distribution estimated from light emission data shown in Fig. 2.11, the fitting parameters are $m = 1.9$ and $n_0 = 21$.

The mean μ and the standard deviation σ are respectively given by

$$\mu = n_0 \Gamma\left(1 + \frac{1}{m}\right), \tag{2.53}$$

$$\sigma = n_0 \sqrt{\Gamma\left(1 + \frac{2}{m}\right) - \left[\Gamma\left(1 + \frac{1}{m}\right)\right]^2}, \tag{2.54}$$

where $\Gamma(\cdot)$ is the gamma function. The coefficient of variation, i.e., the ratio of the standard deviation to the mean

$$C_v := \sigma/\mu, \tag{2.55}$$

is a dimensionless measure of the scatter. For the Weibull distribution, the coefficient of variation depends only on the shape parameter m. As shown by Fig. 2.12(b), C_v decreases from 1 to 0 as m increases ($m \geq 1$). The parameters m and n_0 can be uniquely determined given the mean μ and standard deviation σ. By solving (2.53) and (2.54) for m, we have

$$\frac{\Gamma\left(1 + \frac{2}{m}\right)}{\left[\Gamma\left(1 + \frac{1}{m}\right)\right]^2} - \left(\frac{\sigma}{\mu}\right)^2 - 1 = 0. \tag{2.56}$$

Equation (2.56) is implicit with respect to m, which can be solved numerically. Then it follows from (2.53) that

$$n_0 = \frac{\mu}{\Gamma\left(1 + \frac{1}{m}\right)}. \tag{2.57}$$

Chapter 3: A parallel chain model

The work presented in this chapter is published in [34].

Imagine the following experimental setup. A box-shaped sample of a material has its opposite sides attached to two parallel plates. The distance between these plates is slowly increasing and the elastic force acting upon these plates due to the presence of the material sample between them is being continuously measured. This process is continued until the complete fracture of the material sample. The maximum value of the force measured in this process divided by the cross-sectional area of the sample is *strength*.

A polymer network fractures by breaking covalent bonds, but the experimentally measured strength of a polymer network is orders of magnitude lower than the strength of covalent bonds [10, 11]. In this chapter, we investigate the effect of statistical variation in lengths of polymer chains on strength using a *parallel chain model*. Each polymer chain is represented by a freely-jointed chain, with a characteristic J-shaped force-extension curve. Polymer chains with a statistical distribution of the number of Kuhn segments per chain are pulled between two rigid parallel plates, as illustrated in Fig. 3.1. A full description of the parallel chain model is provided in Section 3.1.

Indeed, we came up with this parallel chain model after some experimentation work on a more realistic network model (see Chapter 4). Nevertheless, the parallel chain model

demonstrates a large reduction in strength, by about two orders of magnitude. Moreover, it exhibits a power law dependence of the strength on the coefficient of variation of the length distribution for polymer chains as the network model does. The simplicity of the parallel chain model allows us to derive the power law analytically using a series of approximations, relying on the fact that the force exerted by each polymer chain varies significantly only for a narrow range of the extension.

The experimental setup for simulations of the parallel chain model is described in Section 3.2. We consider three types of parallel chain models: type one assumes a linear force-extension relationship, and the other two feature J-shaped force-extension curves based on the Langevin function [22] and the modified Langevin function [23], respectively. We compute the applied force on the rigid plates as a function of the extension of chains. The strength of the parallel chain model is defined as the maximum force divided by the total number of chains.

With the J-shaped force-extension relationship, even a small scatter in the number of Kuhn segments per chain greatly reduces the strength of the parallel chain model. The scatter leads to a reduction in strength by up to two orders of magnitude, see Section 3.3. We further show that the strength of the parallel chain model relates to the scatter in the number of Kuhn segments per chain according to a power law.

An analytical derivation of the power law between the strength and the scatter in the number of Kuhn segments per chain (i.e. chain length) is presented in Section 3.4. We show that the strength is approximately inversely proportional to the scatter in chain lengths, provided that the force-extension curve is J-shaped and the probability distribution for the lengths of polymer chains satisfies a certain nonrestrictive technical assumption.

Finally, we test the analytical argument derived in Section 3.4 by taking a piecewise linear approximation of the J-shaped force-extension curve. The approximation is made in the sense that the resulting power law between the strength of the parallel chain model and the scatter in chain lengths provides a good match to the empirical power law shown in Section 3.3. We then test this simple piecewise linear approximation in a different setting where the lengths of polymer chains are scattered according to the Gaussian distribution. Comparison is again made between the resulting power law and the empirical power law. Numerical results are given in Section 3.5.

3.1 Model setup

The polymer network has polymer chains with different numbers of Kuhn segments per chain. When the network is stretched near rupture, only a small fraction of polymer chains are stressed to the covalent bond strength, and other polymer chains still carry entropic forces. Recall that the covalent bond energy is several eV, and the thermal energy is on the order of $k_B T = 1/40$ eV at room temperature, where k_B is the Boltzmann constant and T is the absolute temperature. The two types of energy differ by about two orders of magnitude. For either entropic force or energetic force, the force scales with energy divided by the atomic bond length.

We hypothesize that the large reduction in the strength of polymer networks is caused by statistical variation in lengths of polymer chains and a J-shaped force-extension curve. We test this hypothesis using an idealized parallel chain model. Because the measured strength of a polymer network is unaffected by small crack-like flaws, we ignore any effect

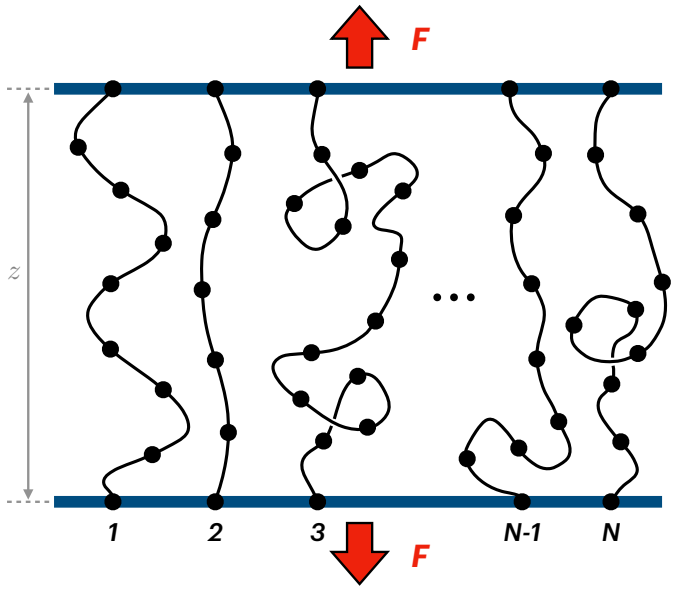

Figure 3.1: The parallel chain model. A large number of polymer chains are arranged in parallel and attached to two rigid plates. Each polymer chain consists of a random number of Kuhn segments. When the two rigid plates are pulled apart by a pair of forces F, all polymer chains are stretched to the same end-to-end distance z.

of stress concentration and adopt a model in which all polymer chains are stretched in parallel between two rigid plates (see Fig. 3.1). In this parallel chain model, crack-like flaws do not concentrate stress in nearby polymer chains.

We represent each polymer chain as a freely-jointed chain consisting of a number of Kuhn segments. The number of Kuhn segments per chain, n, is a random variable, which we assume to obey the Weibull distribution. The choice of the chain length distribution is discussed in Section 2.4. Note that calculations involving evaluations of the force-extension relationship $f = f(z, n)$ for different values of n are simplified in the parallel chain model, since effects of stress concentration and interchain interaction are ignored. Thus, we assume that n follows the continuous Weibull distribution rather than the shifted and discretized version that we will use in the network model in Chapter 4. Moreover, for every polymer

chain, we prescribe a constant breaking force f_b to represent the strength of covalent bonds, which is much larger than the entropic force.

We identify a feature of the force-extension curve of a freely-jointed chain, which has a significant effect on reducing the strength of the parallel chain model. When a single chain is stretched, the force-extension curve is J-shaped. The force is much below the covalent bond strength for a large range of extension (i.e. entropic regime), and grows rapidly to the covalent bond strength only within a small range of extension (i.e. energetic regime), see Fig. 2.4. As a result, the statistical distribution of the number of Kuhn segments per chain causes only a small fraction of polymer chains to be highly stressed, and therefore the average force per chain at rupture is in the entropic regime of the force-extension curve.

3.2 Simulations

In this section, we describe in detail the experimental setup for simulations of the parallel chain model. This includes the settings for the statistical distribution of the number of Kuhn segments per chain (i.e. representing the chain length), the types of force-extension curves, and calculation of some of the important mechanical quantities.

3.2.1 Settings for the scatter in chain lengths

We consider the parallel chain model depicted in Fig. 3.1, in which N polymer chains are arranged in parallel and attached to two rigid plates. The number N is assumed to be large. Each polymer chain consists of a random number of Kuhn segments, denoted by n. As mentioned above, we assume that n follows the continuous Weibull distribution, with

the probability density function (PDF) given by (2.52). This choice is motivated by the distribution of chain lengths estimated based on experimental data of chain rupture [18,28], as discussed in Section 2.4.

To study the effect of the scatter in chain lengths on strength, different sizes of scatter are introduced into the parallel chain model. We fix the mean of the Weibull distribution, $\mu = 50$, and vary the standard deviation σ in the range $0 \leq \sigma \leq \mu$. We characterize the scatter in the number of Kuhn segments per chain using the coefficient of variation, $C_v = \sigma/\mu$, which is a dimensionless measure. The values of σ used in the simulations and corresponding values of C_v are displayed in Fig. 3.2. Note that for the Weibull distribution, the coefficient of variation C_v depends only on the shape parameter m, as evident from (2.55) and (2.56). The shape parameter $m = 1.9$ estimated by fitting experimental data in Fig. 2.11 corresponds to a coefficient of variation $C_v = 0.55$.

Each polymer chain has a force-extension curve of the form $f = f(z, n)$ where f is the force pulling the chain at two ends, and z is the extension in the direction of the applied force. The force-extension curve depends on the number of Kuhn segments per chain, n. We experiment with three types of force-extension curves (see Fig. 3.3) to study the effect of the shape of the force-extension curve on reducing the strength of the parallel chain model. Type one is linear, and the other two are J-shaped curves respectively derived from the Langevin function [22] and the modified Langevin function [23]. For the remainder of this chapter, we will use the following names to refer to these three types of parallel chain models based on their force-extension curves.

- **Linear model:** The linear force-extension relationship takes the form:

$$\frac{z}{n} = \frac{f}{f_b}, \tag{3.1}$$

where f_b is the breaking force. The linear force-extension relationship terminates when the force reaches the breaking force $f = f_b$ at extension $z = n$.

- **Langevin model:** The Langevin force-extension relationship is given by the classical Langevin function

$$\frac{z}{n} = \coth f - \frac{1}{f} =: \mathcal{L}(f). \tag{3.2}$$

- **Modified Langevin model:** The modified Langevin force-extension relationship is given by the modified Langevin function

$$\frac{z}{n} = \left(1 + \frac{f k_B T}{K I_k^2}\right) \mathcal{L}(f), \tag{3.3}$$

where K is the segment elasticity, k_B is the Boltzmann constant, I_k is the Kuhn length, T is the temperature, and $\mathcal{L}(f)$ is the Langevin function defined in (3.2).

Moreover, we set the normalized breaking force to $f_b = 200$ which is the representative strength of covalent bonds, measured from breaking an individual polyacrylamide chain [23]. The breaking force is on the order of 1 nano-Newton, which is orders of magnitude larger than the entropic force. This breaking force is assigned to every polymer chain.

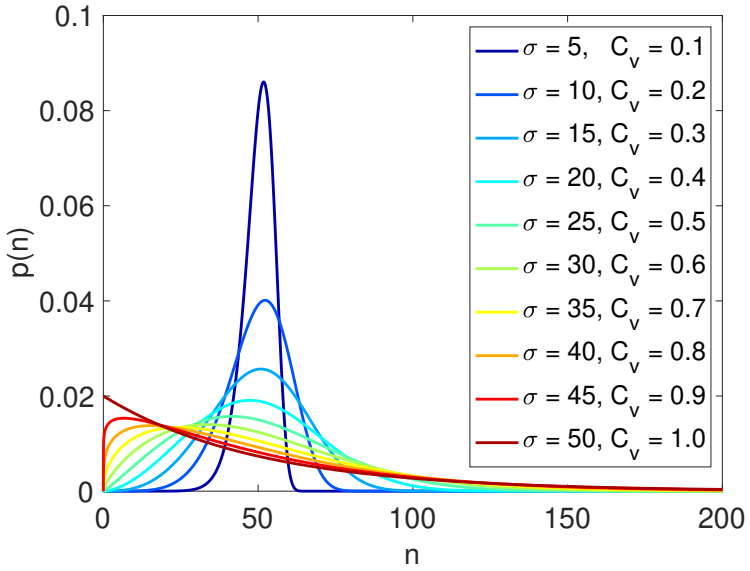

Figure 3.2: Probability density function (PDF) of the Weibull distribution given by (2.52) for mean $\mu = 50$ and various values of standard deviation σ. The shape parameter m and scale parameter n_0 are given by (2.56) and (2.57), respectively. The coefficient of variation is defined as the ratio of the standard deviation to the mean, $C_v = \sigma/\mu$.

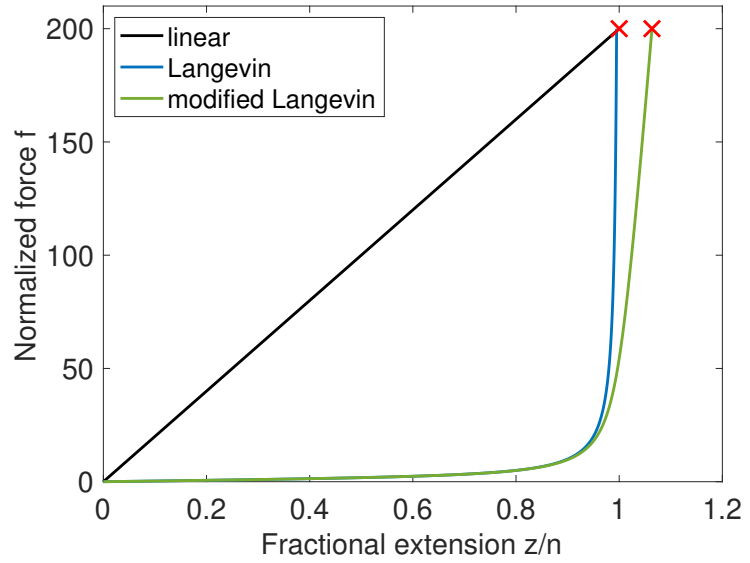

Figure 3.3: Three types of force-extension curves: linear (black), Langevin (blue), and modified Langevin (green) force-extension relationships given by (3.1), (3.2) and (3.3), respectively. All curves terminate at the breaking force $f_b = 200$ [23].

3.2.2 Calculation of mechanical quantities

We compute the force F applied on the rigid plates as a function of the extension of polymer chains, z, as the rigid plates are pulled apart (see Fig. 3.1). The mean force exerted by polymer chains is

$$F(z) = \frac{1}{N} \sum_{j=1}^{N} f(z, n_j) p(n_j), \tag{3.4}$$

where N is the number of parallel chains, n_j is the number of Kuhn segments in the jth polymer chain, $f(z, n)$ is the force-extension relationship, and $p(n)$ is the probability density function (PDF) given by (2.52). The number of parallel chains N is assumed to be large so that the mean force of the parallel chain model is given by

$$F(z) = \int_0^\infty f(z, n) p(n) dn. \tag{3.5}$$

We will evaluate this integral for the three types of force-extension relationships.

As the distance between two rigid plates increases, more and more polymer chains break, and the force-extension curve (3.5) reaches its peak. We interpret the peak force divided by the number of polymer chains as the strength of the parallel chain model, and the extension at the peak force as the extensibility of the parallel chain model, i.e.

$$F_{\max} := \max_z F(z), \tag{3.6}$$

$$z_{\max} := \arg\max_z F(z). \tag{3.7}$$

Note that in experiments of rupturing a polymer network, the strength is defined by the maximum stress, i.e. the maximum force per unit area. In the parallel chain model, the area is constant, and we define the strength by the maximum force per polymer chain.

An ideal parallel chain model is considered for comparison, in which all polymer chains have the same number of Kuhn segments, deform at the same stretch, and break simultaneously. The strength of the ideal model equals the breaking force $f_b = 200$ [23].

3.3 Results

In this section, we present the simulation results of the parallel chain model, which provide valuable insights into its mechanical behavior. In particular, we are interested in the reduction in strength and extensibility compared to the ideal model. Furthermore, a power law relationship between the strength and the scatter in the number of Kuhn segments per chain is found.

3.3.1 Strength

As discussed in Section 3.2.1, we investigate the effects of the following two factors on reducing the strength of the parallel chain model:

(i) *The scatter in the number of Kuhn segments per chain, n.* We use the coefficient of variation $C_v = \sigma/\mu$ to characterize this scatter in chain lengths.

(ii) *The type of the force-extension relationship, $f(z, n)$.* We refer to the parallel chain model with the aforementioned three types of force-extension relationships as the linear model, the Langevin model, and the modified Langevin model, respectively.

We normalize the quantities in (3.5) by changing the variable of integration from n to n/n_0, where n_0 is the scale parameter of the Weibull distribution. This allows us to express the force-extension curve for the parallel chain model in a dimensionless form that relates the normalized mean force F as a function of the fractional extension z/n_0.

The integration of (3.5) gives the normalized force-extension curves for various values of the coefficient of variation C_v for the three types of parallel chain models (i.e. linear, Langevin, and modified Langevin force-extension relationships), as displayed in Fig. 3.4. In all these cases, as the extension z increases, the force starts at zero, reaches a peak, and asymptotically decreases to zero. For small values of C_v, where the scatter in the number of Kuhn segments per chain is small, the mean force exhibits a high peak and a small tail. As C_v increases, the number of Kuhn segments per chain scatters more, the mean force has a lower peak and a fatter tail, and the peak force moves to a lower extension.

Comparing Figs. 3.4(a) and 3.4(b), we observe that the Langevin force-extension relationship leads to much lower peak forces for the parallel chain model than the linear force-extension relationship. In the Langevin force-extension relationship, for most of the range of the extension, the force is relatively low and is primarily governed by entropy. This feature is absent in the linear force-extension relationship so the predicted peak force is much higher. This comparison highlights the importance of the J-shaped force-extension relationship in reducing strength.

The modified Langevin force-extension relationship leads to somewhat higher peak forces than the Langevin force-extension relationship, as shown in Figs. 3.4(b) and 3.4(c). At the largest scatter characterized by $C_v = 1$, the strength of the linear model is about 50, while the modified Langevin force-extension relationship reduces the strength to around 5.

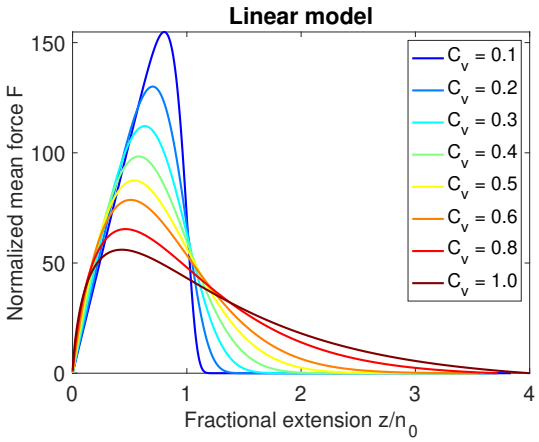

(a)

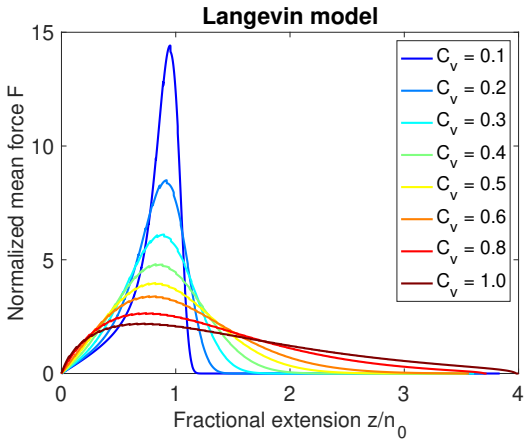

(b)

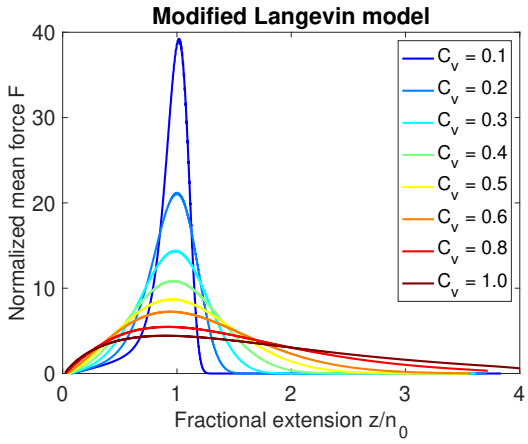

(c)

Figure 3.4: Force-extension curves given by (3.5) for various values of the coefficient of variation C_v for the three types of parallel chain models with (a) linear, (b) Langevin, and (c) modified Langevin force-extension relationships, respectively.

Notably, the Langevin force-extension relationship further reduces the strength to about 2. We remark that the modified Langevin force-extension relationship introduces elasticity of Kuhn segments resulting from the distortion of covalent bonds at high forces. The segment elasticity is characterized by the parameter K.

The scatter in the number of Kuhn segments per chain, characterized by the coefficient of variation C_v, has a significant effect on reducing the strength of the parallel chain model, as demonstrated in Fig. 3.5. When $C_v = 0$, all polymer chains have the same number of Kuhn segments, so the normalized strength is equal to the breaking force $f_b = 200$ [23]. With the Langevin force-extension relationship, introducing a small amount of scatter in the number of Kuhn segments per chain creates a sharp reduction in strength. For instance, for $C_v = 0.1$ there is more than an order of magnitude reduction in strength compared to the ideal model where all chains have the same number of Kuhn segments. Increasing the scatter further reduces the strength. For the Weibull distribution, the largest scatter is $C_v = 1$, at which the strength decreases by about two orders of magnitude compared to the ideal strength.

The reason for this large reduction is that the freely-jointed chain has a J-shaped force-extension curve, in which the force is large only within a narrow range of extension near rupture. Thus, most of the strength comes from a small fraction of polymer chains. As C_v increases, the maximum of the probability distribution decreases, so that strength comes from fewer chains.

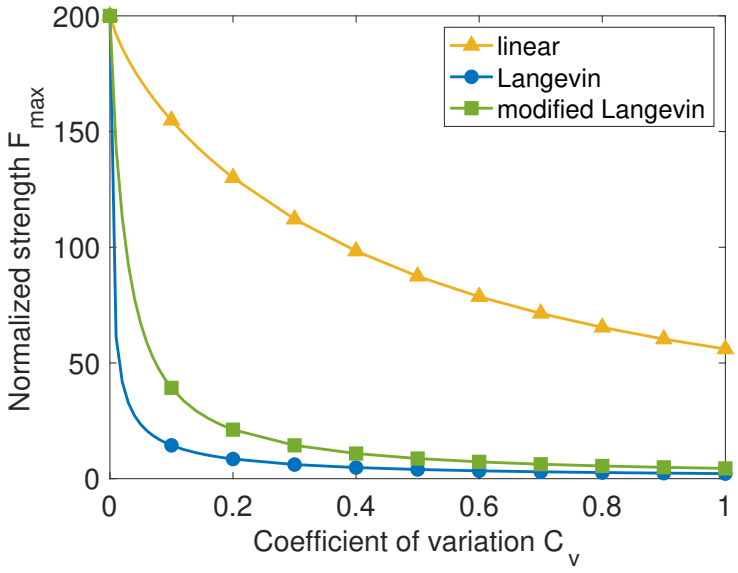

Figure 3.5: The effect of the scatter in chain lengths, characterized by the coefficient of variation $C_v = \sigma/\mu$, on the maximum force (i.e. strength) $F_{\max}$ of the parallel chain model with three types of force-extension relationships (linear, Langevin, and modified Langevin).

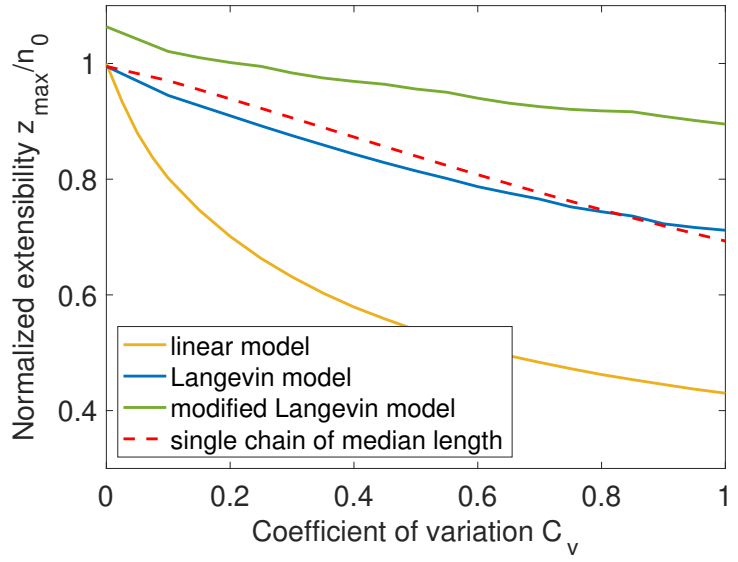

Figure 3.6: The effect of the scatter in chain lengths, characterized by the coefficient of variation $C_v = \sigma/\mu$, on the extensibility $z_{\max}$ of the parallel chain model with three types of force-extension relationships (linear, Langevin, and modified Langevin). The red dashed curve is shown for comparison. It corresponds to a single freely-jointed chain with the median number of Kuhn segments.

3.3.2 Extensibility

We define the extensibility $z_{\max}$ by the extension at which the mean force $F(z)$ peaks. In Fig. 3.6, we plot the normalized extensibility $z_{\max}/n_0$ of the parallel chain model versus the coefficient of variation C_v of the number of Kuhn segments per chain for the three types of force-extension relationships (linear, Langevin, and modified Langevin). It can be seen that the extensibility decreases as the number of Kuhn segments per chain scatters more. However, comparing Figs. 3.5 and 3.6, we note that the scatter in the number of Kuhn segments per chain reduces extensibility much less than it reduces strength.

We note a fact about the Weibull distribution. The median is given by

$$n_{\text{med}} = n_0(\ln 2)^{\frac{1}{m}}, \tag{3.8}$$

where m is the shape parameter and n_0 is the scale parameter. The median moves to lower values of n as m decreases, or as C_v increases. Although (3.8) is specific to the Weibull distribution, the fact that the median decreases with increasing C_v is expected for any one-sided distribution with $p(0) = 0$. Balancing the fatter tail associated with larger C_v requires the median to shift to smaller n.

We find that the extensibility of the Langevin model (i.e. parallel chain model with the Langevin force-extension relationship) is correlated with the extension where a single freely-jointed chain with the median number of Kuhn segments is stretched to rupture. Approximating the extensibility as the extension where the chain with the median number

of Kuhn segments achieves the breaking force f_b gives

$$\frac{z_{\text{med}}}{n_0} = (\ln 2)^{\frac{1}{m}} \mathcal{L}(f_b). \tag{3.9}$$

This equation is also plotted in Fig. 3.6. The right-hand side of (3.9) as a function of the coefficient of variation C_v deviates from the normalized extensibility of the Langevin model by less than 7% over the entire range $C_v \in [0, 1]$.

3.3.3 Power law relationship

We take a second look at Fig. 3.5 and seek to quantify the effect of the scatter in the number of Kuhn segments per chain on the strength of the parallel chain model. Graphs of the normalized strength $F_{\max}$ as a function of the coefficient of variation C_v for the three types of force-extension relationships are plotted in Fig. 3.7, on the log-log scale. The curves for the Langevin and modified Langevin force-extension relationships are nearly linear on the log-log scale and hence suggest a power law between the strength $F_{\max}$ and the coefficient of variation C_v:

$$F_{\max} = A \cdot (C_v)^q, \tag{3.10}$$

where A and q are constants that need to be determined. The empirical power laws obtained by least squares fit are shown in Table 3.1. The power law relationship is also derived analytically via a series of approximations in the next section.

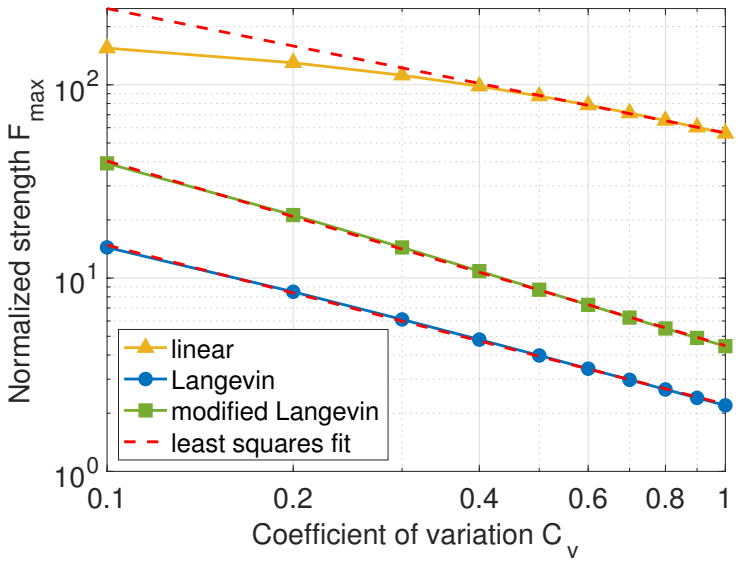

Figure 3.7: The empirical power law relationship between the strength $F_{\max}$ of the parallel chain model and the coefficient of variation C_v of the number of Kuhn segments per chain for the three types of force-extension relationships (linear, Langevin, and modified Langevin). The red dashed line is the least squares fit to the empirical power law relationship.

Table 3.1: The empirical power law relationship between the strength $F_{\max}$ and C_v.

Force-extension relationship	Least squares fit to $F_{\max} = A \cdot (C_v)^q$
Langevin	$2.22 \cdot C_v^{-0.824}$
modified Langevin	$4.47 \cdot C_v^{-0.955}$
linear, $C_v \geq 0.5$	$56.40 \cdot C_v^{-0.643}$

3.4 Heuristic derivation of the power law relationship

In this section, we provide an analytical derivation that explains the origin of a power law relationship between the strength $F_{\max}$ of the parallel chain model and the coefficient of variation C_v of the number of Kuhn segments per chain. The power law relationship is in the form of (3.10). The key component of the derivation is that the force-extension relationship is significantly different from zero only within a narrow interval near rupture.

We will show that the strength of the parallel chain model is approximately inversely proportional to the coefficient of variation C_v due to the following two factors. First, the force-extension relationship predicts nonzero force values only within a small interval near the fracture point. Second, the Weibull family of distributions and some other suitable families of distributions possess the property that $\max_z [zp(z)]$ is approximately inversely proportional to the coefficient of variation C_v. Thus, we make the following assumptions.

Assumption 1. The force-extension relationship $f(z, n)$, where n is the number of Kuhn segments per chain, can be approximated by a function of the form

$$\hat{f}(z,n) = \begin{cases} 0, & 0 < \frac{z}{n} < \xi_1, \\ \left(\frac{z}{n} - \xi_1\right) g\left(\frac{z}{n}\right), & \xi_1 < \frac{z}{n} < \xi_2, \\ 0, & \frac{z}{n} > \xi_2, \end{cases} \tag{3.11}$$

where $g(\xi)$ is a smooth slowly changing function on the interval $\xi_1 < \xi < \xi_2$, and the length of the interval (ξ_1, ξ_2), $l := \xi_2 - \xi_1$, is small in comparison with ξ_1. Assumption 1 holds for the Langevin and modified Langevin force-extension relationships.

Assumption 2. The family of probability distributions $p(n;\mu,\sigma)$, where μ and σ are, respectively, the mean and the standard deviation, has the property that the maximum of $np(n;\mu,\sigma)$ is approximately inversely proportional to the coefficient of variation, $C_v = \sigma/\mu$:

$$\max_n np(n;\mu,\sigma) \approx BC_v^{-q}, \tag{3.12}$$

where B is a constant and q is close to 1. Note that this assumption holds for a family of distributions with the probability density function of the form

$$p(n;\mu,\sigma) \approx \frac{1}{\sigma}\rho\left(\frac{n-\mu}{\sigma}\right), \tag{3.13}$$

provided that μ is much larger than σ, by at least a factor of 3. The function $\rho(\cdot)$ represents a unimodal distribution. Then the maximum of the product $np(n;\mu,\sigma)$ is achieved near the mean, i.e. $n = \mu$. Hence, we have

$$\max_n \frac{n}{\sigma}\rho\left(\frac{n-\mu}{\sigma}\right) \approx \frac{\mu}{\sigma}\rho(0) = \rho(0)C_v^{-1}. \tag{3.14}$$

Our goal is to show that the maximum of the mean force relates to the coefficient of variation C_v according to a power law, i.e.

$$\max_z \int_0^\infty f(z,n)p(n)dn \approx AC_v^{-q}, \tag{3.15}$$

where A is a constant and q is close to 1. To derive the power law, we take a series of approximations as follows.

First, according to Assumption 1, for a fixed z, the approximation $\hat{f}(z,n)$ to the force-extension relationship $f(z,n)$ is nonzero only within the interval

$$\frac{z}{\xi_2} < n < \frac{z}{\xi_1}. \tag{3.16}$$

For further calculations of the mean force, it is convenient to introduce a parameter r and a small parameter ϵ such that

$$\begin{aligned} \xi_1 &= \frac{r}{1+\epsilon}, \\ \xi_2 &= \frac{r}{1-\epsilon}. \end{aligned} \tag{3.17}$$

It is easy to check that such parameters r and ϵ are given by

$$\begin{aligned} r &:= \frac{2\xi_1\xi_2}{\xi_1+\xi_2}, \\ \epsilon &:= \frac{\xi_2-\xi_1}{\xi_1+\xi_2}. \end{aligned} \tag{3.18}$$

Then the mean force $F(z)$ of the parallel chain model can be approximated by

$$\begin{aligned} F(z) &= \int_0^\infty f(z,n)p(n)dn \\ &\approx \int_0^\infty \hat{f}(z,n)p(n)dn \\ &= \int_{\frac{z}{\xi_2}}^{\frac{z}{\xi_1}} \left(\frac{z}{n}-\xi_1\right) g\left(\frac{z}{n}\right) p(n)dn \\ &= \int_{\frac{z(1-\epsilon)}{r}}^{\frac{z(1+\epsilon)}{r}} \left(\frac{z}{n}-\frac{r}{1+\epsilon}\right) g\left(\frac{z}{n}\right) p(n)dn. \end{aligned} \tag{3.19}$$

Next, we rescale the integral in (3.19) to the interval $[-z/r, z/r]$ by introducing a new variable

$$u := \frac{n - z/r}{\epsilon}.$$

Noting that $dn = \epsilon du$ and $n = \frac{z}{r} + \epsilon u$, we continue the calculation in (3.19):

$$F(z) = \int_{-\frac{z}{r}}^{\frac{z}{r}} \left(\frac{z}{\frac{z}{r} + \epsilon u} - \frac{r}{1+\epsilon} \right) g\left(\frac{z}{\frac{z}{r} + \epsilon u} \right) p(\tfrac{z}{r} + \epsilon u) \epsilon du. \tag{3.20}$$

Then we take into account the fact that ϵ is a small parameter in comparison with 1, while $\frac{z}{r} \approx 1$, and that, by Assumption 1, g is slowly changing. Furthermore, since ϵ is small, the expression in the first parenthesis in (3.20) can be simplified to

$$\begin{aligned} \frac{z}{\frac{z}{r} + \epsilon u} - \frac{r}{1+\epsilon} &= \frac{r}{1 + \frac{r\epsilon u}{z}} - \frac{r}{1+\epsilon} \\ &\approx r\left(1 - \frac{r\epsilon u}{z}\right) - r(1-\epsilon) \\ &= r\epsilon\left(1 - \frac{ru}{z}\right). \end{aligned} \tag{3.21}$$

We simply ignore the small parameter ϵ in the functions g and p in (3.20).

Therefore, we obtain the following approximation for the mean force of the parallel chain model:

$$\begin{aligned} F(z) &\approx \epsilon g(r) p\left(\frac{z}{r}\right) \int_{-\frac{z}{r}}^{\frac{z}{r}} r\epsilon \left(1 - \frac{ru}{z}\right) du \\ &= 2\epsilon^2 g(r) z p\left(\frac{z}{r}\right) =: \hat{F}(z). \end{aligned} \tag{3.22}$$

The strength of the parallel chain model is the maximum of the mean force, $\max_z F(z)$. Assumption 2 and (3.22) imply that

$$\begin{aligned}\max_z F(z) &\approx 2\epsilon^2 r g(r) \max_z \left[\frac{z}{r} p\left(\frac{z}{r}\right)\right] \\ &\approx 2\epsilon^2 r g(r) \max_{z'} \left[z' p(z')\right] \\ &\approx 2\epsilon^2 r g(r) B C_v^{-q} \\ &= A C_v^{-q}, \end{aligned} \tag{3.23}$$

where $A := 2\epsilon^2 r g(r) B$ is a constant, B is the constant in (3.12), and q is close to 1. Thus, the strength of the parallel chain model depends on the coefficient of variation C_v according to a power law.

We now derive the power law relationship for two particular families of probability distributions: the Weibull distribution and the Gaussian distribution. In order to find the maximizer of $zp(z)$, i.e.

$$z_{\max} := \arg\max_z \left[z p(z)\right], \tag{3.24}$$

we differentiate $zp(z)$ and set its derivative to zero. This results in the following equation for the maximizer $z_{\max}$:

$$z = -\frac{p(z)}{p'(z)}. \tag{3.25}$$

3.4.1 The Weibull distribution

The derivative of the Weibull probability density function (PDF) given by (2.52) is

$$p'(z) = \left[\frac{m(m-1)}{n_0^m} z^{m-2} - \frac{m^2}{n_0^{2m}} z^{2m-2}\right] \exp\left(-\frac{z^m}{n_0^m}\right). \tag{3.26}$$

Hence, (3.25) becomes

$$z = -\frac{z}{(m-1) - \frac{m}{n_0^m} z^m}. \tag{3.27}$$

The solution to this equation is

$$z_{\max} = n_0. \tag{3.28}$$

Plugging $z = n_0$ and the Weibull PDF (2.52) into (3.22), we obtain

$$\max_z F(z) \approx \hat{F}(n_0) = 2\epsilon^2 r g(r) m \exp(-1). \tag{3.29}$$

The shape parameter m of the Weibull distribution can be uniquely determined given the coefficient of variation, $C_v = \sigma/\mu$, using equation (2.56). In particular, for $0.1 \leq C_v \leq 1$, the parameter m can be closely approximated by

$$m \approx 0.9871 \cdot C_v^{-1.0961}, \quad 0.1 \leq C_v \leq 1. \tag{3.30}$$

Substituting the expression for m from (3.30) into (3.29), we obtain the following power law relationship:

$$\max_z F(z) \approx 0.9871 \cdot 2\epsilon^2 r g(r) \exp(-1) \cdot C_v^{-1.0961}. \tag{3.31}$$

Table 3.1 shows that the empirical values of the power of C_v in the power law for the Langevin and modified Langevin force-extension relationships are different from -1.0961, and the discrepancy is larger for the Langevin model than the modified Langevin model. These discrepancies result from the errors committed due to the use of the midpoint rule and due to ignoring the tail of the Weibull distribution.

3.4.2 The Gaussian distribution

The Gaussian distribution has the probability density function (PDF)

$$p(z) = \frac{1}{\sigma\sqrt{2\pi}} \exp\left[-\frac{1}{2}\left(\frac{z-\mu}{\sigma}\right)^2\right]. \tag{3.32}$$

Equation (3.25) for the Gaussian distribution becomes

$$z^2 - \mu z - \sigma^2 = 0. \tag{3.33}$$

The positive solution to this equation is given by

$$z_{\max} = \frac{\mu + \mu\sqrt{1+4C_v^2}}{2}, \tag{3.34}$$

where $C_v = \sigma/\mu$ is the coefficient of variation. We assume that $C_v \leq 1/3$ so that negative values of z are extremely unlikely, based on the fact that 99.7% of the values following the Gaussian distribution lie within 3σ of the mean μ. Then $z_{\max}$ is approximated by

$$z_{\max} \approx \mu(1 + C_v^2). \tag{3.35}$$

Plugging (3.35) and the Gaussian PDF (3.32) into (3.22), we obtain

$$\begin{aligned}\max_z F(z) &\approx \hat{F}(\mu(1+C_v^2)) \\ &= 2\epsilon^2 r g(r) \frac{\mu(1+C_v^2)}{\sigma\sqrt{2\pi}} \exp\left(-\frac{1}{2}C_v^2\right) \\ &\approx \frac{2\epsilon^2 r g(r)}{\sqrt{2\pi}} C_v^{-1}. \end{aligned} \tag{3.36}$$

Therefore, the power law dependence of the strength on the coefficient of variation is not specific to the Weibull distribution, but can be expected for any distribution of chain lengths that is approximately Gaussian near its maximum. The power laws for the Langevin and modified Langevin models are given in Tables 3.2 and 3.3, respectively. Although the J-shaped force-extension relationships are not in the same form as approximation (3.11), this idealized approximation allows us to provide a simple derivation of the power law.

3.5 Piecewise linear approximation of the J-shaped curve

The J-shaped force-extension curve is of particular importance due to its characteristic behavior where the force is almost zero for a large range of extension, and is significantly different from zero only within a small range of extension. The task in this section is to test the analytical argument for the power law by taking a piecewise linear approximation of the J-shaped force-extension curve, see Fig. 3.8. This approximation method is chosen because it provides a simplified representation of the sophisticated J-shaped curve. Our goal is to show that the exact shape of the force-extension curve is *not* necessary for deriving the power law between the strength of the parallel chain model and the scatter in chain lengths.

3.5.1 Least squares approximation

We approximate the force-extension relationship $f(z/n)$ by a piecewise linear function

$$\hat{f}(\xi) = \begin{cases} M_1(\xi - \xi_0), & 0 < \xi < \xi_1, \\ M_2(\xi - \xi_1) + f_1, & \xi_1 < \xi < \xi_2, \\ 0, & \xi > \xi_2, \end{cases} \tag{3.37}$$

where $\xi = z/n$ is the fractional extension. The parameters in (3.37) are defined as follows.

- ξ_0 denotes the fractional extension at zero force $f = 0$. Its value is chosen to be either $\xi_0 = 0$, as derived from the Langevin function (2.13), or the root-mean-square value

$$\xi_0 = \frac{z_0}{n} = \frac{1}{\sqrt{3n}}, \tag{3.38}$$

  where z_0 is the equilibrium chain length given by (2.21).

- ξ_2 denotes the fractional extension at the breaking force $f_b = 200$ [23]. Its value is found to be $\xi_2 = 0.995$ for the Langevin force-extension relationship, and $\xi_2 = 1.064$ for the modified Langevin force-extension relationship. We set $\hat{f}(\xi_2) = f(\xi_2) = f_b$.

- The constants M_1 and M_2 represent the slopes of the linear segments in the entropic regime and the energetic regime, respectively. Their values can be determined from ξ_1 and f_1. Here M_2 is much larger than M_1 for the J-shaped force-extension curve.

- The point (ξ_1, f_1), where $f_1 = \hat{f}(\xi_1)$, is the glue point that needs to be determined.

The best least squares approximation to the force-extension relationship $f(z/n)$ by the piecewise linear function $\hat{f}(z/n)$ is obtained in the following way. First, we approximate the mean force $F(z)$ defined in (3.5) by

$$\hat{F}(z) = \int_0^\infty \hat{f}(z/n)p(n)dn, \tag{3.39}$$

where $p(n)$ is the Weibull probability density function (PDF) given by (2.52). We denote by $\hat{F}_{\max}$ the approximated value of the strength, i.e., the maximum of $\hat{F}(z)$

$$\hat{F}_{\max} := \max_z \hat{F}(z). \tag{3.40}$$

Next, we obtain the power law relationship between the approximated strength $\hat{F}_{\max}$ and the coefficient of variation C_v:

$$\hat{F}_{\max} = \hat{A} \cdot (C_v)^{\hat{q}}, \tag{3.41}$$

where $\hat{A}$ and $\hat{q}$ are constants determined by least squares fit. By varying the location of the glue point (ξ_1, f_1) in (3.37), we compare the constants $\hat{A}$ and $\hat{q}$ obtained from (3.41) with the empirical values of A and q given in Table 3.1.

Finally, we choose the glue point (ξ_1, f_1) such that the resulting values of $\hat{A}$ and $\hat{q}$ are as close as possible to the empirical values of A and q. This is achieved by minimizing the sum of squared errors $S = (\hat{A} - A)^2 + (\hat{q} - q)^2$, which allows us to determine the best piecewise linear approximation $\hat{f}(z/n)$ to the J-shaped force-extension relationship $f(z/n)$. We will test this best approximation in a different setting for the parallel chain model.

3.5.2 Numerical results

Below we compare the power law relationship (3.41), which is obtained using the piecewise linear approximation of the J-shaped force-extension curve, with the empirical power law relationship shown in Table 3.1. The comparison will be made for the Langevin and modified Langevin force-extension relationships. Note that the empirical power law between the strength and the coefficient of variation is observed for the parallel chain model in which the number of Kuhn segments per chain (i.e. chain length) follows the continuous Weibull distribution. We will show that similar results can be obtained in a different setting where we assume a truncated Gaussian distribution for the lengths of polymer chains.

Modified Langevin model. We first implement the piecewise linear approximation for the modified Langevin model, which refers to the parallel chain model with the modified Langevin force-extension relationship. In this case, the J-shaped force-extension curve has a finite slope in the energetic regime, which allows for a more accurate approximation. As illustrated in Fig. 3.8, the best least squares approximation to the modified Langevin force-extension relationship by a piecewise linear function of the form (3.37) yields

$$\hat{f}(\xi) = \begin{cases} 5.144(\xi - \xi_0), & 0 < \xi < 0.972, \\ 2130.8(\xi - 0.972) + 5.0, & 0.972 < \xi < 1.064, \\ 0, & \xi > 1.064, \end{cases} \tag{3.42}$$

where $\xi = z/n$ is the fractional extension and ξ_0 is the fractional extension at zero force. The number of Kuhn segments per chain, n, is assumed to follow the continuous Weibull

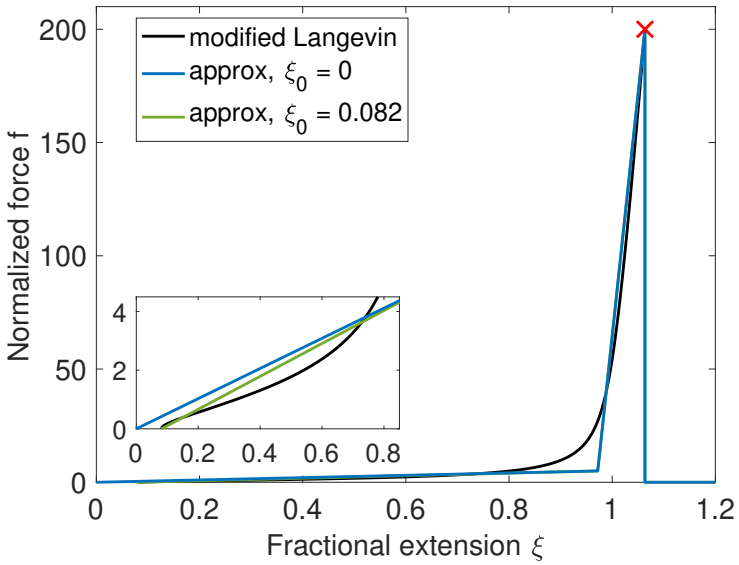

Figure 3.8: Approximation of the modified Langevin force-extension relationship by the piecewise linear function (3.42) for two values of the equilibrium fractional extension ξ_0. The inset shows that the value of ξ_0 affects the approximation only in the low-force region.

distribution in the simulations. The mean of the Weibull distribution for n is set to $\mu = 50$. We consider two different values of ξ_0 for numerical experiments: $\xi_0 = 0$ and

$$\xi_0 = \frac{1}{\sqrt{3\mu}} \approx 0.082, \tag{3.43}$$

where we replace n in (3.38) with the mean value $\mu = 50$. Graphs of the piecewise linear approximation (3.42) for $\xi_0 = 0$ and $\xi_0 = 0.082$ are plotted in Fig. 3.8. The inset shows the discrepancy in the low-force region.

The corresponding graphs of the approximated strength $\hat{F}_{\max}$ as a function of the coefficient of variation C_v are shown in Fig. 3.9(a) on the log-log scale. The match between these graphs and the black graph which corresponds to the exact strength is very close. The resulting power laws obtained by least squares fit are given in Table 3.2 for the Weibull

distribution of chain lengths. Comparison is made with the empirical power law observed for the parallel chain model with the modified Langevin force-extension relationship. For both values of ξ_0, the constants $\hat{A}$ and $\hat{q}$ in the resulting power law (3.41) give good agreement with their empirical values. This suggests that the piecewise linear approximation method can capture the essential characteristic of the J-shaped force-extension curve, which is appropriate for estimating the power law relationship.

To demonstrate the robustness of this simple approximation method, we implement the piecewise linear function (3.42) in a different setting for the parallel chain model. Instead of assuming the Weibull distribution for the lengths of polymer chains, we consider a truncated Gaussian distribution. To obtain the power law relationship that is comparable to the case of the Weibull distribution, we set the same mean value for the Gaussian distribution, $\mu = 50$. The standard deviation σ is varied and assumed to be small enough so that negative values are extremely unlikely, i.e. $\sigma/\mu \leq 1/3$. The coefficient of variation $C_v = \sigma/\mu$, varying in the range $0 \leq C_v \leq 0.3$, is relatively small.

In Fig. 3.9(b), the approximated strength $\hat{F}_{\max}$ of the parallel chain model is plotted against the coefficient of variation C_v for the case of the Gaussian distribution. The results obtained using the piecewise linear approximation (3.42) for the two values of ξ_0 are in good agreement with the exact strength (black graph), which is similar to the case of the Weibull distribution. Least squares fits to the resulting power laws are shown in Table 3.2. The estimated decay rate $|\hat{q}|$ in (3.41) is slightly higher than the empirical value $|q| = 0.821$, but lower than the power decay rate in the Weibull distribution case. The estimated value of the prefactor $\hat{A}$ is smaller than its empirical value but comparable to the Weibull case.

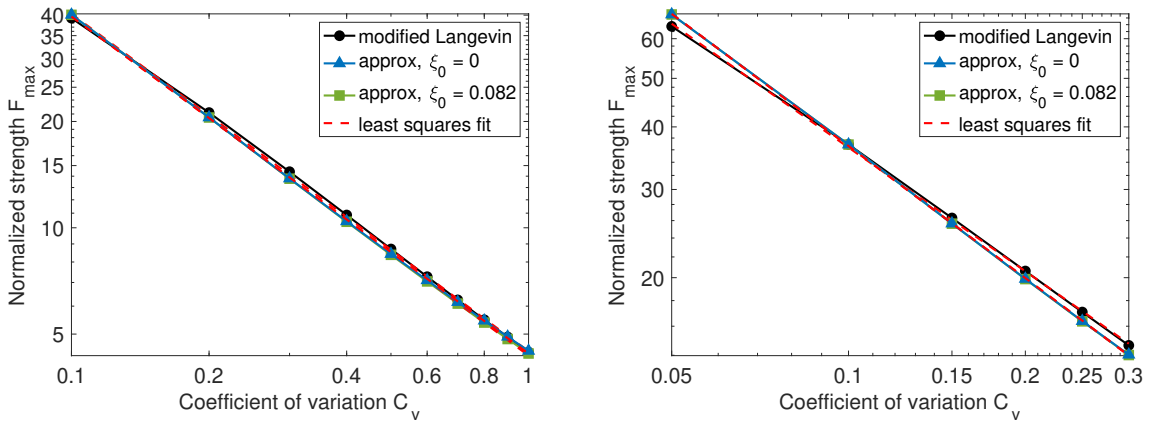

(a) The Weibull distribution

(b) The Gaussian distribution

Figure 3.9: The power law between the strength $F_{\max}$ and the coefficient of variation C_v, obtained using the modified Langevin force-extension relationship (black) and its piecewise linear approximation (3.42) with $\xi_0 = 0$ (blue) and $\xi_0 = 0.082$ (green). The red dashed line is the least squares fit to the power law. The statistical distribution for the number of Kuhn segments per chain: (a) the Weibull distribution and (b) the Gaussian distribution.

Table 3.2: Comparison between the empirical power law and the power law obtained using the piecewise linear approximation of the modified Langevin force-extension relationship.

Chain length distribution	Force-extension relationship	Least squares fit to $F_{\max} = A \cdot (C_v)^q$
Weibull distribution	Empirical, modified Langevin	$4.47 \cdot C_v^{-0.955}$
	Approximation (3.42), $\xi_0 = 0$	$4.40 \cdot C_v^{-0.954}$
	Approximation (3.42), $\xi_0 = 0.082$	$4.34 \cdot C_v^{-0.962}$
Gaussian distribution	Empirical, modified Langevin	$5.50 \cdot C_v^{-0.821}$
	Approximation (3.42), $\xi_0 = 0$	$4.87 \cdot C_v^{-0.876}$
	Approximation (3.42), $\xi_0 = 0.082$	$4.86 \cdot C_v^{-0.877}$

Langevin model. We now present the numerical results for the Langevin model. The best piecewise linear approximation of the Langevin force-extension relationship is given by

$$\hat{f}(\xi) = \begin{cases} 4.461(\xi - \xi_0), & 0 < \xi < 0.964, \\ 6302.4(\xi - 0.964) + 4.3, & 0.964 < \xi < 0.995, \\ 0, & \xi > 0.995, \end{cases} \tag{3.44}$$

where $\xi = z/n$ is the fractional extension and ξ_0 is the fractional extension at zero force. In this case, the ratio of the slopes in the energetic regime and the entropic regime is very large, i.e. $M_2/M_1 = 1413$, which captures the significant difference in the stiffness of the force-extension curve between the two regimes. Graphs of the approximation (3.44) for $\xi_0 = 0$ and $\xi_0 = 0.082$ are shown in Fig. 3.10.

Then, similar to the modified Langevin model, we implement the piecewise linear function (3.44) in the two settings for the chain length distribution. Corresponding graphs of the approximated strength $\hat{F}_{\max}$ as a function of the coefficient of variation C_v for the Weibull distribution and the Gaussian distribution are plotted in Figs. 3.11(a) and 3.11(b), respectively. For the Weibull distribution, the results obtained from the piecewise linear approximation closely match the exact strength (black graph). However, the match between these graphs is less accurate for the Gaussian distribution, especially when C_v is close to 0. The discrepancy is primarily due to the error introduced by approximating the steep slope of the Langevin force-extension relationship. Least squares fits to the resulting power laws for both types of distributions of chain lengths are provided in Table 3.3. The close match to the empirical power law highlights the robustness of the power law relationship.

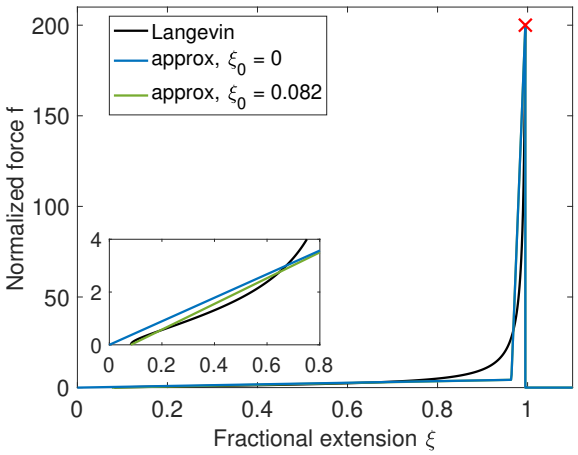

Figure 3.10: Approximation of the Langevin force-extension relationship by the piecewise linear function (3.44) for two different values of the equilibrium fractional extension ξ_0. The inset shows that the value of ξ_0 affects the approximation only in the low-force region.

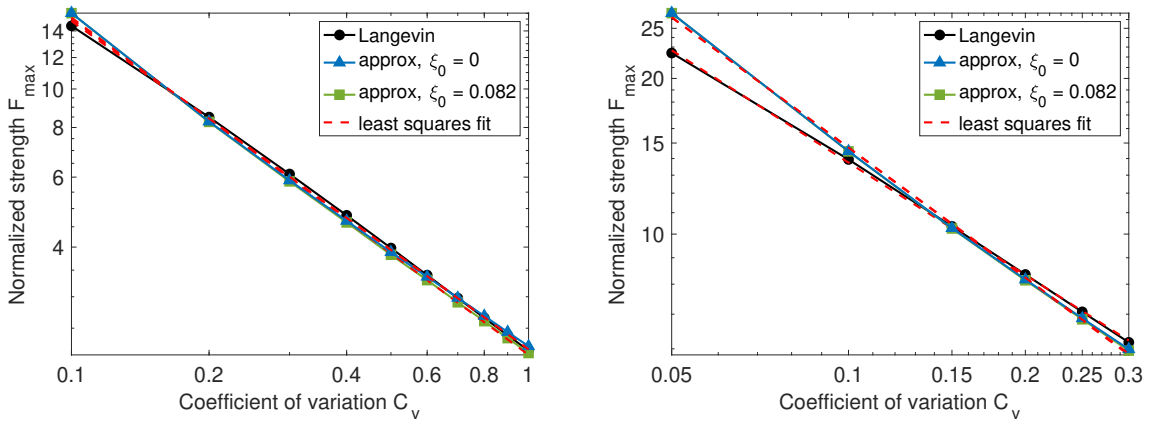

(a) The Weibull distribution

(b) The Gaussian distribution

Figure 3.11: The power law between the strength $F_{\max}$ and the coefficient of variation C_v, obtained using the Langevin force-extension relationship (black) and its piecewise linear approximation (3.44) with $\xi_0 = 0$ (blue) and $\xi_0 = 0.082$ (green). The red dashed line is the least squares fit to the power law relationship. The statistical distribution for the number of Kuhn segments per chain: (a) the Weibull distribution and (b) the Gaussian distribution.

Table 3.3: Comparison between the empirical power law and the power law obtained using the piecewise linear approximation of the Langevin force-extension relationship.

Chain length distribution	Force-extension relationship	Least squares fit to $F_{\max} = A \cdot (C_v)^q$
Weibull distribution	Empirical, Langevin	$2.22 \cdot C_v^{-0.824}$
	Approximation (3.44), $\xi_0 = 0$	$2.26 \cdot C_v^{-0.820}$
	Approximation (3.44), $\xi_0 = 0.082$	$2.19 \cdot C_v^{-0.836}$
Gaussian distribution	Empirical, Langevin	$2.61 \cdot C_v^{-0.721}$
	Approximation (3.44), $\xi_0 = 0$	$2.15 \cdot C_v^{-0.836}$
	Approximation (3.44), $\xi_0 = 0.082$	$2.13 \cdot C_v^{-0.839}$

3.6 Discussion

We compare the simulation results with the experimental data for the polyacrylamide hydrogel [10]. In the experiment, the strength is measured by dividing the breaking force of a sample by its initial cross-sectional area. The measured strength is 30.5 kPa in [10]. During deformation, the hydrogel does not change the volume. At breaking, the stretch is about 11 [10], so the initial cross-sectional area is about 11 times the cross-sectional area at breaking. The area per monomer is taken to be 2.2×10^{-19} m^2. The hydrogel consists of both polymer and water, and the volume fraction of polymer is 0.128. Consequently, at breaking, the average force per polymer chain is

$$30.5 \text{ kPa} \cdot 2.2 \times 10^{-19} \text{ m}^2 \cdot 11/0.128 \approx 6 \times 10^{-13} \text{ N}.$$

The rupture force of a carbon-carbon bond is a few nanoNewtons, e.g. 1.2 nN [23]. Thus, the ratio of the theoretical strength to the experimental strength is 2,000. By comparison, the parallel chain model with the Langevin force-extension relationship predicts the ratio to be 75 at the maximum amount of scatter, $C_v = 1$.

Moreover, the measured extensibility is also much lower than that of an ideal network. In [10], the measured extensibility is 10.1, and the ideal extensibility is estimated to be about 41. Consequently, the ratio of the ideal extensibility to the measured extensibility is about 4. The parallel chain model predicts the ratio to be about 2 at the largest scatter, $C_v = 1$. It can be seen that, in each case, the parallel chain model explains a portion of the discrepancy between the ideal strength and extensibility. However, even pushing the

coefficient of variation C_v to the limiting value is not sufficient to completely explain the giant discrepancy between the theoretical and experimental values.

We understand this shortcoming as follows. In the parallel chain model where all polymer chains have the same extension, it is not possible to consider concentration of stress and deformation around defects. Although, the parallel chain model is chosen since it is believed that the network structure of polymer materials deconcentrates stress [35], it alone is not sufficient to describe the large reduction in strength. This suggests that, although polymer networks deconcentrate stress around defects when compared with silica, concentration of stress and localization of deformation still play a role. We will investigate these phenomena using a network model in Chapters 4 and 5.

Chapter 4: A polymer network model

In this chapter, we develop a network model based on a diamond grid structure, which is an idealized representation of a polymer network. Each polymer chain is represented by a freely-jointed chain that features a J-shaped stress-stretch relationship. We incorporate network imperfection (see Fig. 4.1) into the model by assuming a statistical distribution for the lengths of polymer chains. Numerical simulations are performed on networks of different sizes and of various amounts of scatter in chain lengths. The objective of our work is to understand the effect of the scatter in chain lengths on the fracture properties of polymer networks.

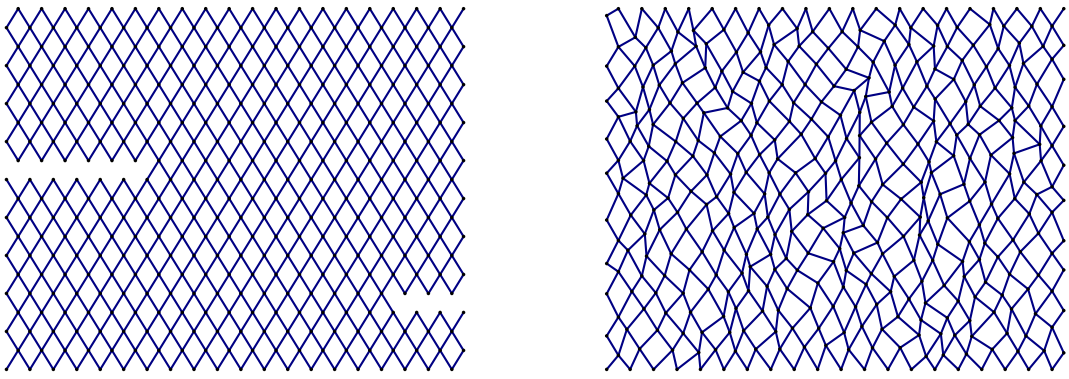

(a) Crack-like flaws (b) Scatter in chain lengths

Figure 4.1: Examples of network imperfection: (a) cracks and (b) scatter in chain lengths.

4.1 Model setup

Setting up a polymer network model, our goal is twofold: first, we aim to show that some of the mechanical properties observed in fracture of hydrogels [10], i.e., a small scatter in strength from sample to sample and a large reduction in strength compared to the ideal network, can be demonstrated using a simple lattice structure; second, the model should be amenable for numerical experiments.

A two-dimensional network refers to an array of nodes connected into a diamond grid by links. Each link represents a polymer chain consisting of a number of Kuhn segments. The nodes at the ends of links represent the crosslinkers that connect neighboring polymer chains to form a network. We denote by $M \times N$ the size of a network with M nodes in the x-direction and N nodes in the y-direction. In simulations, the network is assumed to have the bottom boundary fixed, and the top boundary being pulled up via a series of small increments until the network completely breaks.

As an idealized model, we use a network of lattice structure to represent a polymer network. The choice of the shape and boundary conditions for the network is discussed in Section 4.1.1. Two key factors are taken into account: (i) elimination of the boundary effect and (ii) reduction in computation time. After experimentation, we have settled on the following network model. The shape of the network is rectangular in a diamond grid structure. The lateral boundaries are assumed to have x-coordinates fixed, which eliminates the boundary effect. We incorporate the two components described in Chapter 2 into the network, i.e., scatter in lengths of polymer chains and a J-shaped stress-stretch relationship. A complete description of our network model is provided in Section 4.1.2.

4.1.1 Geometry and boundary conditions

Choosing the shape and the boundary conditions for the network model requires some experimentation. We first consider two-dimensional rectangular networks of different sizes: 20×20 (square), 20×80 (slim and tall), and 80×20 (wide and low), where all links are of the same length. The bottom boundary is fixed and the top boundary is controlled by us. We experiment with free lateral boundaries. The network is stretched in a quasi-stationary manner until a complete fracture, i.e., the nodes on the top and bottom boundaries belong to different connected components of the network. In all these cases, breaking scenarios and mechanical properties such as strength, extensibility, and work of fracture, are highly affected by the fact that the lateral boundaries are free. Upon stretching, the stress increases at a slightly faster rate near the corners which causes the polymer chains there to rupture first, and then a cascade of chain breakage starting from two opposite corners takes place. Its development depends on the dimension of the network. This phenomenon is known as the boundary effect.

One way to eliminate the boundary effect is to make the network cylindric in three dimensions. We consider cylindric networks of sizes 20×20, 40×40, and 80×20 (wide) and stretch them by pulling up the top boundaries. It is observed that the work values for them are affected by the reduction of the diameter of the mid-section accompanying vertical elongation. Moreover, small defects are introduced into the network model to study the effect of network imperfection. We find that complete fracture of imperfect cylindric networks takes significantly more time than that of rectangular networks due to additional degrees of freedom.

Finally, we have settled on rectangular networks of size $N \times N$ in which boundary conditions are applied to create a pure shear deformation [36]. In other words, the left and right lateral boundaries are constrained in the x-direction while the network is being stretched in the y-direction. This setting eliminates the boundary effect, renders values of work of fracture for ideal networks that are consistent with simple theoretical predictions, and leads to reasonable runtime.

4.1.2 Our network model

In this dissertation, we have chosen a two-dimensional network model where a polymer network is idealized to a diamond grid structure, as illustrated in Fig. 4.2. The diamond cells in an ideal network would have two angles of 60 degrees and two angles of 120 degrees.

Each link connecting two neighboring nodes represents a polymer chain which consists of a number of Kuhn segments, n. The equilibrium length of each link is given by (2.21), i.e.

$$l_0 = I_k \sqrt{\frac{n}{3}}, \tag{4.1}$$

where I_k is the Kuhn length [29, 30]. Here we set $I_k = 1$ for simplicity. An ideal network is a perfect network where all links are of equal equilibrium length. In other words, all polymer chains have the same number of Kuhn segments. The width W and the initial height H_0 of an ideal network are respectively set to

$$W = l_0(N-1) = \sqrt{\frac{n}{3}}(N-1), \tag{4.2}$$

$$H_0 = \frac{\sqrt{3}}{2} l_0(N-1) = \frac{\sqrt{n}}{2}(N-1). \tag{4.3}$$

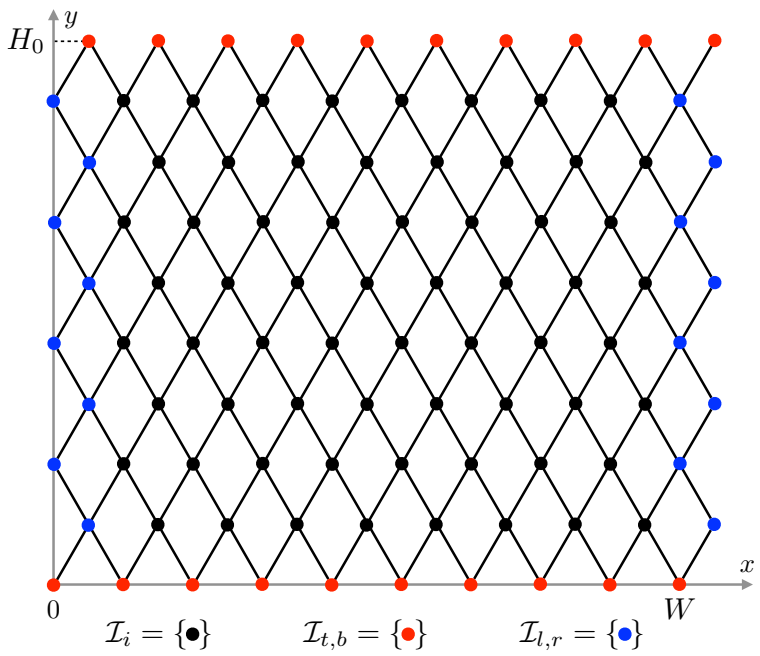

Figure 4.2: Notations for the sets of interior nodes (black) and boundary nodes (red, blue) for a two-dimensional network in a diamond grid structure.

We will denote the set of interior nodes of the network by $\mathcal{I}_i$, and the sets of its top, bottom, left, and right boundary nodes, respectively, by $\mathcal{I}_t$, $\mathcal{I}_b$, $\mathcal{I}_l$, and $\mathcal{I}_r$ (see Fig. 4.2).

In simulations, we introduce statistical variation in local properties by scattering the number of Kuhn segments per chain, n according to a shifted and discretized Weibull distribution (see Fig. 4.3). We assume that n takes only integer values. The probability for a polymer chain to have n Kuhn segments is

$$p(n; m, n_0) = \begin{cases} \exp\left[-\left(\frac{n-n_{\min}}{n_0}\right)^m\right] - \exp\left[-\left(\frac{n+1-n_{\min}}{n_0}\right)^m\right], & n \geq n_{\min}, \\ 0, & n < n_{\min}, \end{cases} \tag{4.4}$$

where $n_{\min}$ is the minimal admissible number of Kuhn segments. In simulations, we set $n_{\min} = 10$ and fix the mean of the Weibull distribution, $\mu = 50$. The standard deviation

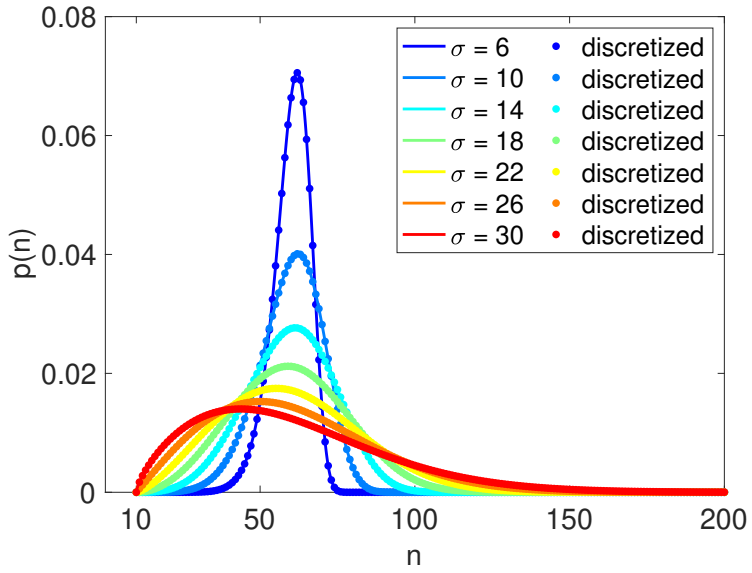

Figure 4.3: The shifted and discretized Weibull distribution given by (4.4) for $n_{\min} = 10$, mean $\mu = 50$, and various values of standard deviation σ.

σ varies in the range $0 \leq \sigma \leq \mu$. An ensemble of graphs of the shifted and discretized Weibull distribution for $n_{\min} = 10$, $\mu = 50$, and different values of σ are shown in Fig. 4.3.

The stress-stretch relationship on the links (i.e. representing polymer chains) is nonlinear and J-shaped. Each link possesses a force-extension relationship of the form $f = f(z, n)$ where f is the tensile force, z is the extension of the link, and n is the number of Kuhn segments per chain. In our network model, $f(z, n)$ is implicitly defined by

$$\text{modified } z_{\text{RMS}} = \left(1 + \frac{f k_B T}{K I_k^2}\right) \sqrt{n\left[1 - \frac{2\mathcal{L}(f)}{f}\right] + (n^2 - n)[\mathcal{L}(f)]^2}. \tag{4.5}$$

We employ the modified z_{RMS} as the J-shaped force-extension curve because a nonzero chain length at equilibrium is needed. A close approximation is designed for the inversion of modified z_{RMS} (see Section 2.3.3). Using the representative strength of covalent bonds, we set the normalized breaking force to $f_b = 200$ [23] for all links.

4.2 Simulations

In this section, we describe in detail the experimental setup for numerical simulations of our network model. The network is first initialized by scattering the lengths of polymer chains, and then stretched in a quasi-stationary manner until a complete fracture.

4.2.1 Initialization

The minimal admissible number of Kuhn segments is $n_{\min} = 10$. The mean of the Weibull distribution is set to $\mu = 50$, and the standard deviation σ is varied. The different values of σ used in the simulations are displayed in Fig. 4.3. Let $\bar{n}$ denote the mean of the shifted Weibull distribution for n, i.e.

$$\bar{n} = \mu + n_{\min} = 60. \tag{4.6}$$

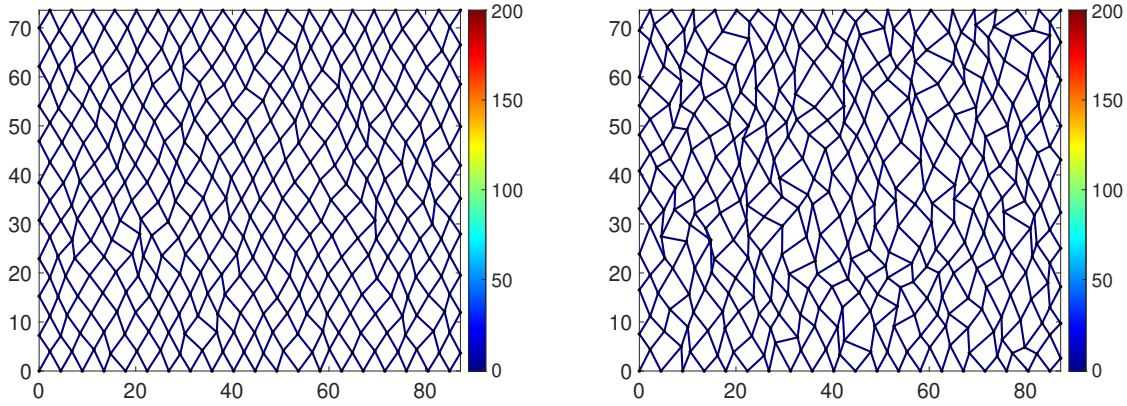

(a) $\sigma = 10$ (b) $\sigma = 30$

Figure 4.4: Initialization of 20×20 networks with two different scatters in chain lengths. The number of Kuhn segments per chain, n, is scattered according to the shifted and discretized Weibull distribution given by (4.4) for $n_{\min} = 10$, mean $\mu = 50$, and standard deviations of (a) $\sigma = 10$ and (b) $\sigma = 30$.

We set the width W and the initial height H_0 of the network respectively to

$$W = \sqrt{\frac{\bar{n}}{3}}(N-1), \tag{4.7}$$

$$H_0 = \frac{\sqrt{\bar{n}}}{2}(N-1). \tag{4.8}$$

This corresponds to an ideal network where all polymer chains consist of $\bar{n}$ Kuhn segments. Next, we allow the network to relax while holding the bottom boundary at $y = 0$ and the top boundary at $y = H_0$, as well as fixing the x-coordinates of the nodes on the left and right lateral boundaries. This means that we solve the following system of $2N^2 - 6N + 4$ nonlinear equations for a network of size $N \times N$:

$$\begin{cases} \displaystyle\sum_{k\sim j} f(\|\mathbf{r}_j - \mathbf{r}_k\|, n_{jk}) \frac{x_j - x_k}{\|\mathbf{r}_j - \mathbf{r}_k\|} = 0, \quad j \in \mathcal{I}_i, \\ \displaystyle\sum_{k\sim j} f(\|\mathbf{r}_j - \mathbf{r}_k\|, n_{jk}) \frac{y_j - y_k}{\|\mathbf{r}_j - \mathbf{r}_k\|} = 0, \quad j \in \mathcal{I}_i \cup \mathcal{I}_l \cup \mathcal{I}_r, \end{cases} \tag{4.9}$$

where $\mathbf{r}_j = (x_j, y_j)$ represents node j, $k \sim j$ denotes that node k is connected to node j by a polymer chain, n_{jk} is the number of Kuhn segments in that chain, and $f = f(z, n)$ is the force-extension relationship. The sets of interior and boundary nodes (i.e. $\mathcal{I}_i$, $\mathcal{I}_l$, $\mathcal{I}_r$) are illustrated in Fig. 4.2. The nonlinear system (4.9) is large and poorly scaled, and therefore requires numerical methods for its solution (see Section 4.3). Graphs of 20×20 networks initialized with two different scatters in chain lengths are shown in Fig. 4.4. The scatter is characterized by the standard deviation σ of the number of Kuhn segments per chain.

4.2.2 Stretching experiments

As we have mentioned, we stretch the network in a quasi-stationary manner. Thus, after the initial relaxation, we perform a sequence of very small stretch steps with a fixed increment of the total height ΔH. The stretching is stopped when the network completely breaks, i.e., after the final stretch step, the top and bottom layers of nodes belong to different connected components. At each stretch step, we increase the y-coordinates of the top layer of nodes by ΔH, and then allow the network to relax by solving the nonlinear system (4.9). Note that this system is nonlinear even for a linear stress-stretch relationship.

We have conducted a series of numerical simulations of stretching networks up to a complete fracture. The networks are of four different sizes, 20×20, 40×40, 60×60, and 80×80. The number of Kuhn segments per chain, n, follows the shifted and discretized Weibull distribution defined by (4.4) for $n_{\min} = 10$, mean $\mu = 50$, and standard deviations of $\sigma = 6$, 10, 14, 18, 22, 26, and 30. The stress-stretch relationship is J-shaped, based on the modified z_{RMS} given by (2.22). Ideal networks where all links have the same equilibrium length are also studied for comparison.

In each setting, we compute the force at the top of the network during the stretching process. This allows us to capture and analyze important mechanical properties, including strength, extensibility, and work of fracture. Moreover, a power law relationship between the strength and the scatter in chain lengths is observed in our network model, which is similar to the findings in the parallel chain model discussed in Chapter 3. By comparison, the power decay in the network model is slower than that found in the parallel chain model.

4.2.3 Choosing numerical methods

In this dissertation, we will use Nesterov's accelerated gradient descent (NAGD) [37] to solve the nonlinear system (4.9). NAGD has shown itself to be highly reliable and robust. A description of the NAGD algorithm is given in Section 4.3.

We have also implemented other iterative methods to solve the system (4.9), including regular gradient descent (GD), Levenberg-Marquardt (LM) [38], and adaptive moment estimation (ADAM) [39]. However, it turns out that all of these methods are not suitable for solving the system (4.9). GD takes a large number of iterations for convergence that would not finish, and is considerably slower than NAGD. The Levenberg-Marquardt (LM) algorithm suffers from an issue of the trust region radius shrinking to machine epsilon since the Jacobian matrix for system (4.9) is poorly conditioned. The GD and LM algorithms are both getting stalled as chains start to break.

On the other hand, the performance of ADAM is comparable to NAGD, but ADAM is slightly worse as it requires more adjustments of parameters. ADAM is an adaptive optimization algorithm that computes adaptive learning rates for each parameter based on their first and second moments. ADAM has gained popularity in machine learning due to its robustness to a wide range of non-convex optimization problems. However, we find that ADAM does not have obvious advantages over NAGD when solving (4.9). Hence we do not proceed with implementation of ADAM.

4.2.4 Computational difficulties

The runtime of simulations significantly increases with the size of the network. Larger networks require more computational resources and time compared to smaller networks. Simulations of complete fracture of 20×20 and 40×40 networks take only 30 to 40 minutes and 12 to 15 hours, respectively. By contrast, the runtime for 60×60 networks increases to about 3 weeks, and it takes around 5 to 6 weeks for simulations of 80×80 networks.

The long runtime for large networks is a consequence of the increased complexity of numerically solving the large system of nonlinear equations (4.9). The nonlinearity of the system is compounded by the J-shaped stress-stretch relationship. To solve the nonlinear system (4.9), iterative numerical methods are commonly used. These methods iteratively update the positions of nodes and recompute the forces until convergence is achieved. However, the nonlinearity of the J-shaped stress-stretch relationship makes the convergence slower and more computationally demanding.

Furthermore, the scatter in chain lengths adds to the computational complexity of simulations. Recall from Section 2.3.3 that our approximation of the J-shaped stress-stretch relationship, $f(z, n)$, depends on the number of Kuhn segments per chain, n. Therefore, chains of different lengths may experience different stages of stretching under the same macroscopic deformation. This can lead to much more complicated convergence patterns when solving the system (4.9) and hence additional calculations are required to reach the equilibrium state.

Due to these challenges, the network model by Lavoie and Suo [40] considered only the linear force-extension curve. They used ABACUS software and were able to introduce

scatter only in the breaking force (i.e. strength) of network links, but not in the lengths of polymer chains. The numerical simulations in [40] were performed on networks of size 80×80, which is also the maximum size of our network model. In this dissertation, we address the computational difficulty arising from the J-shaped force-extension relationship and focus on the effect of the scatter in chain lengths on the network strength.

To reduce the computational cost of solving the system (4.9), it is intuitive to consider taking a simple approximation of the J-shaped force-extension curve that provides cheaper function evaluations. We have implemented the piecewise linear approximation of the modified Langevin function, as described in Section 3.5. However, it turns out that this approach does not lead to a significant reduction in runtime for our network model.

4.3 Nesterov's accelerated gradient descent

In this section, we describe Nesterov's accelerated gradient descent (NAGD) [37], the iterative method that we use for solving the nonlinear system (4.9). In particular, we make the learning rate adaptive at each update step to avoid artificial chain breakage, and employ a restarting technique [41] for fast and reliable convergence.

4.3.1 The algorithm and convergence rate

Given an objective function $f : \mathbb{R}^d \to \mathbb{R}$ that is convex and smooth, we consider the unconstrained minimization problem

$$\min_{x \in \mathbb{R}^d} \; f(x). \tag{4.10}$$

The simplest and most common optimization approach is gradient descent (GD),

$$x_{t+1} = x_t - \eta_t \nabla f(x_t), \tag{4.11}$$

where $\eta_t > 0$ is the learning rate and the gradient $\nabla f : \mathbb{R}^d \to \mathbb{R}^d$ is Lipschitz continuous with constant $L > 0$. For a sufficiently small step size $0 < \eta_t \leq \frac{1}{L}$, the GD algorithm has the convergence rate $O\left(\frac{1}{t}\right)$. While GD is universally popular, alternative methods such as classical momentum (MOM) [42] and Nesterov's accelerated gradient descent (NAGD) [37] can result in significantly faster convergence to the optimal value.

NAGD algorithm. Nesterov proposed an accelerated gradient descent (NAGD) method in 1983 [37], which aims to improve the convergence rate of regular gradient descent approaches. The NAGD algorithm takes the following form: starting with an initial point $x_0 \in \mathbb{R}^d$ and setting $y_0 = x_0$, it iteratively updates the sequences

$$\begin{aligned} &\text{(gradient update)} \quad y_{t+1} = x_t - \eta_t \nabla f(x_t), \\ &\text{(extrapolation)} \qquad x_{t+1} = y_{t+1} + \theta_t (y_{t+1} - y_t), \end{aligned} \tag{4.12}$$

where $\eta_t > 0$ is the learning rate and $0 \leq \theta_t \leq 1$ is the extrapolation weight. In other words, NAGD performs a gradient descent step from the current point x_t to an intermediate point y_{t+1}, and then moves slightly beyond y_{t+1} in the direction given by the previous point y_t. The gradient update step can be viewed as performing a look-ahead gradient evaluation. The subsequent extrapolation step adjusts the update direction by taking into account the momentum accumulated from the previous update.

Recently, Sutskever et al. [43] derived an alternative scheme for NAGD that resembles

a momentum method. They showed that by defining $v_{t+1} := x_{t+1} - x_t$, the original NAGD algorithm (4.12) can be rewritten as:

$$\begin{aligned} v_{t+1} &= \theta_t v_t - \eta_t \nabla f(x_t + \theta_t v_t), \\ x_{t+1} &= x_t + v_{t+1}. \end{aligned} \tag{4.13}$$

Although NAGD is not typically thought of as a momentum method, this formulation reveals its close relation to classical momentum (MOM) [42]. In both cases, the algorithm tends to continue updating the sequences along the previous update direction. The only difference lies in the update of the velocity vector v_t: MOM evaluates the gradient ∇f at the current point x_t, while NAGD evaluates ∇f at the extrapolated point $x_t + \theta_t v_t$.

In practice, the choice of the learning rate η_t and the extrapolation weight θ_t (also referred to as the momentum coefficient) has a significant impact on the performance of NAGD. Appropriate tuning of these parameters can improve convergence and stability [43]. Techniques such as line search and adaptive strategies can be employed to find suitable parameter values. Nesterov [37] proposed the schedule $\theta_t = \frac{t}{t+3}$, which we adopt in the experiments. Moreover, we make the learning rate η_t adaptive at each update step and use a restarting technique [41]. Our particular schedule for η_t is described in Section 4.3.2.

Convergence rate. We discuss below the convergence rate of the NAGD algorithm with the following schedule for the learning rate η_t and the momentum coefficient θ_t:

$$\begin{aligned} \eta_t &= \frac{1}{L}, \\ \theta_t &= \frac{t}{t+3}, \end{aligned} \tag{4.14}$$

where L is the Lipschitz constant of the gradient ∇f. Note that setting $\eta_t = \frac{1}{L}$ simplifies the original algorithm which chooses η_t at each update step using the bisection method.

Theorem 4.1 *Suppose the function $f : \mathbb{R}^d \to \mathbb{R}$ is convex and its gradient $\nabla f : \mathbb{R}^d \to \mathbb{R}^d$ is Lipschitz continuous with constant $L > 0$. Then the sequence $f(x_t)$ generated by the NAGD algorithm (4.12) with the parameter schedule (4.14) converges to the optimal value $f^* = f(x^*)$ at the rate $O\left(\frac{1}{t^2}\right)$ as*

$$f(x_t) - f^* \leq \frac{2L\|x_0 - x^*\|^2}{t^2}. \tag{4.15}$$

Nesterov proved that the convergence rate $O\left(\frac{1}{t^2}\right)$ is optimal among all first-order methods [37, 44]. This is in contrast to regular gradient descent methods, which have the same computational complexity but can only achieve a $O\left(\frac{1}{t}\right)$ convergence rate [38]. Moreover, while classical momentum (MOM) [42] (also known as heavy-ball method) has been shown to exhibit a faster convergence rate than regular gradient descent for quadratic problems, current analysis only gives a global convergence rate of $O\left(\frac{1}{t}\right)$ for MOM [45].

The improved convergence rate of NAGD is attributed to the introduction of the momentum term $v_{t+1} = x_{t+1} - x_t$ as well as the particularly tuned coefficient

$$\theta_t = \frac{t}{t+3} = 1 - \frac{3}{t} + O\left(\frac{1}{t^2}\right). \tag{4.16}$$

We note that the constant 3, derived from $(t+3)-t$ in (4.16), is a so-called magic number. In fact, it is the smallest constant that guarantees the $O\left(\frac{1}{t^2}\right)$ convergence rate for NAGD, as discussed by Su et al. [46]. They demonstrated that the constant 3 can be replaced

by any larger number, resulting in a generalized NAGD algorithm with the momentum coefficient defined by

$$\theta_t = \frac{t}{t+r}, \quad r \geq 3, \tag{4.17}$$

while maintaining the inverse quadratic convergence (see [46] for theoretical analysis).

In general, NAGD is not a descent algorithm, i.e. does not monotonically decrease the objective function value, due to the introduction of the momentum term. Oscillations or overshoots along the trajectory of iterates approaching the minimizer are often observed. This empirical observation can be modeled using an ordinary differential equation (ODE). Su et al. [46] derived a second-order ODE which is the continuous limit of the iterates of NAGD. This ODE exhibits approximate equivalence to the NAGD algorithm in terms of trajectory behaviors and convergence rates, which can serve as a tool for analysis. The observed oscillation phenomenon is interpreted by viewing the ODE as a damping system. Despite the presence of short-term fluctuations, the overall performance of the NAGD algorithm is highly reliable and robust.

Since the introduction of Nesterov's accelerated gradient, there has been significant research on the development of first-order accelerated methods. Theoretical developments of various convergence-rate theorems were given in Nesterov's subsequent works [44, 47, 48], and a unified analysis of these methods was provided by Tseng [49]. Many approaches have been developed to speed up the convergence of Nesterov's algorithm, such as adaptive learning rate methods [50–52], restarting techniques [41, 46], and other variants [48, 53, 54]. Notable applications can be found in a wide range of fields, including deep and recurrent neural networks [43], compressed sensing [55], and sparse linear regression [53, 56].

4.3.2 Adaptive learning rate and restarting

We now apply Nesterov's accelerated gradient descent (NAGD) [37] to solve the nonlinear system (4.9) and describe our particular schedule for an adaptive learning rate. Indeed, solving the system (4.9) can be formulated as an optimization problem, where the objective is to find the position of the network that minimizes the potential energy of this physical system. Below we present the application of the NAGD algorithm for solving (4.9) and provide an initial guess for the solution.

We rewrite the system (4.9) as a nonlinear equation

$$\mathbf{F}(\mathbf{p}) = \mathbf{0}, \tag{4.18}$$

where $\mathbf{F}$ denotes the left-hand side of (4.9) and $\mathbf{p}$ is the vector of coordinates of free nodes

$$\mathbf{p} = \begin{bmatrix} x_{j,\ j\in\mathcal{I}_i} \\ \\ y_{j,\ j\in\mathcal{I}_i\cup\mathcal{I}_l\cup\mathcal{I}_r} \end{bmatrix} \in \mathbb{R}^d. \tag{4.19}$$

The dimension of the space is $d = 2N^2 - 6N + 4$ where N is the network size. Note that the force $\mathbf{F}$ is the negative gradient of the potential energy U, i.e. $\mathbf{F} = -\nabla U$. Then the system (4.9) is equivalent to

$$\nabla U(\mathbf{p}) = -\mathbf{F}(\mathbf{p}) = \mathbf{0}. \tag{4.20}$$

Hence, the solution of (4.9) can be interpreted as the minimizer of the potential $U(\mathbf{p})$.

In this work, we use the NAGD algorithm (4.12) to minimize the potential $U(\mathbf{p})$. As mentioned in Section 4.3.1, we adopt the schedule proposed by Nesterov [37] for the

momentum coefficient, $\theta_t = \frac{t}{t+3}$, and design an adaptive schedule for the learning rate η_t. The NAGD update for the position vector $\mathbf{p}$ is given by

$$\begin{aligned} \mathbf{q}_{t+1} &= \mathbf{p}_t + \eta_t \mathbf{F}(\mathbf{p}_t), \\ \mathbf{p}_{t+1} &= \mathbf{q}_{t+1} + \frac{t}{t+3}(\mathbf{q}_{t+1} - \mathbf{q}_t), \end{aligned} \tag{4.21}$$

where the negative gradient $-\nabla U$ is replaced by the force $\mathbf{F}$. We describe below a suitable choice of the initial point $\mathbf{p}_0$ and the schedule for η_t, which can speed up the convergence.

Recall that the network is stretched by a sequence of small steps until a complete fracture. At each stretch step, we iterate the update formula (4.21) to find the equilibrium position of the network. For stretch step $k > 1$, an initial guess $\mathbf{p}_0^{(k)}$ for the solution of system (4.9) can be obtained using linear extrapolation from the previous two stretch steps:

$$\mathbf{p}_0^{(k)} = 2\mathbf{p}_*^{(k-1)} - \mathbf{p}_*^{(k-2)}, \quad k = 2, 3, ..., \tag{4.22}$$

where $\mathbf{p}_*^{(k)}$ denotes the solution of (4.9) found at stretch step k. It should be noted that when a link breaks, the initial guess (4.22) is not applicable and we simply use the previous solution $\mathbf{p}_*^{(k-1)}$ as the initial point. In this case, the NAGD algorithm requires much more iterations to converge, till the norm of the residual being less than 10^{-7} for 80×80 networks.

The stopping criterion for the update formula (4.21) is that, either the number of iterations exceeds 10^8, or the norm of the force $\mathbf{F}$ normalized by the network size N decays to a certain threshold:

$$\begin{aligned} \frac{\|\mathbf{F}\|}{N} &< 10^{-8}, \quad \text{for } N = 20, 40, \\ \frac{\|\mathbf{F}\|}{N} &< 10^{-7}, \quad \text{for } N = 60, 80. \end{aligned} \tag{4.23}$$

The convergence threshold is relaxed for large networks to reduce computation time.

In the original setting where we used a constant learning rate $\eta_t = 0.2$, scenarios of artificial chain breakage were observed. A number of network links ruptured simultaneously within a single stretch step, leading to a rapid and unrealistic fracture of the network. Such artificial breaking scenarios result in an underestimation of the ultimate properties (strength, extensibility, and work of fracture) of the network model. This entails the need for an adaptive learning rate that can recover the behavior of progressive chain breakage.

The learning rate η_t needs to be adapted to account for the J-shaped force-extension relationship. As seen in Fig. 2.4, the force grows rapidly only within a narrow range of extension before rupture. Even a small stretch step of the network can lead to a blow up of forces on many endangered chains that are highly stressed. It turns out that the constant learning rate $\eta_t = 0.2$ is too high to capture the sensitive changes in forces within the energetic regime, and therefore results in artificial chain breakage. To address this issue, we reduce the learning rate in situations where multiple chains may rupture simultaneously. This ensures that polymer chains rupture only when they should, in a progressive manner.

An adaptive schedule for the learning rate η_t is carefully designed for our network model. The default value for the learning rate is set to $\eta_t = 0.2$. At each stretch step, we allow the network to relax. The new equilibrium position is found using the update formula (4.21), which iteratively updates the position vector $\mathbf{p}$ and recomputes the force $\mathbf{F}$ on chains. A chain ruptures if the force acting on it exceeds the prescribed breaking force $f_b = 200$. The learning rate η_t is programmed to be reduced by half if more than one chain is predicted to rupture in the next update step, and it can be reduced up to the minimum value $\eta_{\min} = 10^{-5}$ if necessary.

We restart the NAGD algorithm whenever the learning rate η_t is reduced. Restarting the algorithm means that we start the algorithm again, taking the current iteration as the new starting point, i.e., (4.21) is restarted with $\mathbf{p}_0 = \mathbf{q}_0 := \mathbf{p}_t$ whenever it predicts that more than one chain will rupture. This erases the memory of previous iterations and resets the momentum back to zero, preventing the momentum coefficient $\theta_t = \frac{t}{t+3}$ from steadily decreasing over the iterations. By periodically resetting the momentum coefficient to zero, the restarting technique prevents the accumulation of too much momentum that may cause unnecessary oscillations or overshoots, and therefore leads to fast and reliable convergence. A heuristic analysis in [41] suggests that adaptively restarting the algorithm can recover the optimal linear rate of convergence in many cases.

Indeed, we have encountered other unfavorable situations where it is necessary to adapt the learning rate η_t and reset the momentum coefficient θ_t to zero. It is well-known that NAGD is not a descent algorithm, and the decay of the norm of the residual typically occurs in the form of oscillations with decreasing amplitude. In programming, we keep reducing η_t up to the minimum threshold $\eta_{\min} = 10^{-5}$ and restart the NAGD algorithm from the current iteration if any of the following conditions holds:

(i) More than one polymer chain is predicted to rupture in the next iteration, i.e., there are multiple chains with forces exceeding the breaking force, $f > f_b$. This motivates the need to avoid artificial chain breakage.

(ii) The number of iterations exceeds 5×10^4 while the norm of the residual $\|\mathbf{F}\|/N$ remains larger than 10^{-2}. This situation indicates that the iterates of NAGD may be overshooting the minimizer when the learning rate η_t is too high.

(iii) The norm of the residual exhibits an oscillation pattern where $\|\mathbf{F}\|/N$ first decreases but then starts to grow larger than its initial value. The oscillatory behavior may eventually lead to a blow up of the norm of the residual.

It has been empirically observed in [41, 46] that the restarting technique can significantly boost convergence by reducing bumps in the norm of the residual. Moreover, the minimum value of the learning rate is small enough so that $\|\mathbf{F}\|$ decays monotonously while it is still large or comparable to the breaking force, ensuring that chains break only if they should.

The NAGD algorithm has shown itself to be highly reliable and robust in simulations of our network model. Despite the nonlinear system (4.9) being large and poorly scaled, the solution can be found typically within a few thousand iterations for 80×80 networks, thanks to a suitable choice of the initial guess using information from previous iterations. When a polymer chain ruptures, the initial guess given by (4.22) is no longer applicable due to the J-shaped stress-stretch relationship, in which case NAGD requires significantly more iterations to converge. Most importantly, by employing an appropriate learning rate schedule, the NAGD algorithm always converges without getting stuck.

A pseudocode providing a template for Nesterov's accelerated gradient descent (NAGD) is outlined in Algorithm 1. It describes the solution of the nonlinear system (4.9) at each stretch step. In this dissertation, the numerical solver has been implemented using the C programming language. We have programmed everything from scratch, in particular, the design of the adaptive schedule for the learning rate, the choice of the minimum threshold for the learning rate that ensures progressive chain breakage, and the detection of poor convergence behavior that requires restarting. Our C codes are available upon request.

Algorithm 1: Nesterov's accelerated gradient descent (NAGD)

Initialization:

Set default learning rate $\eta_t = 0.2$ and minimum value $\eta_{\min} = 10^{-5}$;

Set stopping tolerance $tol = 10^{-8}$ for $N = 20, 40$ and $tol = 10^{-7}$ for $N = 60, 80$;

Set initial point $\mathbf{p}_0 := 2\mathbf{p}_*^{(k-1)} - \mathbf{p}_*^{(k-2)}$ if no chain breaks; otherwise $\mathbf{p}_0 := \mathbf{p}_*^{(k-1)}$;

Set $\mathbf{q}_0 := \mathbf{p}_0$ and $t := 0$;

while $\|\mathbf{F}(\mathbf{p}_t)\|/N < tol$ ***and*** *number of iterations* $< 10^8$ **do**

  $\mathbf{q}_{t+1} := \mathbf{p}_t + \eta_t \mathbf{F}(\mathbf{p}_t)$;

  $\mathbf{p}_{t+1} := \mathbf{q}_{t+1} + \frac{t}{t+3}(\mathbf{q}_{t+1} - \mathbf{q}_t)$;

  Compute forces f on polymer chains at position $\mathbf{p}_{t+1}$;

  while *more than one chain has force* $f > f_b$ ***and*** $\eta_t > \eta_{\min}$ **do**

    Reduce learning rate $\eta_t := \eta_t/2$ and reset $t := 0$;

    $\mathbf{q}_{t+1} := \mathbf{p}_t + \eta_t \mathbf{F}(\mathbf{p}_t)$;

    $\mathbf{p}_{t+1} := \mathbf{q}_{t+1} + \frac{t}{t+3}(\mathbf{q}_{t+1} - \mathbf{q}_t)$;

    Compute forces f on polymer chains at position $\mathbf{p}_{t+1}$;

  end

  Set $t := t + 1$;

  if *there exists a chain with* $f > f_b$ **then** that chain breaks and restart NAGD;

  if $\|\mathbf{F}(\mathbf{p}_t)\|/N > 10^{-2}$ ***and*** *number of iterations* $> 5 \times 10^4$ **then**

    Reduce learning rate $\eta_t := \eta_t/2$ and reset $t := 0$;

  end

  if $\|\mathbf{F}(\mathbf{p}_t)\|$ *grows larger than its initial value* $\|\mathbf{F}_0\|$ **then**

    Reduce learning rate $\eta_t := \eta_t/2$ and reset $t := 0$;

  end

end

4.4 Results

In this section, we present the simulation results of our network model. Specifically, stress-stretch curves are obtained during stretching experiments of the network model. The stretching experiments are categorized by two properties, the size of the network $N \times N$ and the scatter in chain lengths. The scatter in chain lengths is characterized by the standard deviation σ of the number of Kuhn segments per chain.

4.4.1 Calculation for the ideal network

We calculate the strength and extensibility of the ideal network, where all polymer chains consist of the same number of Kuhn segments, deform at the same stretch, and break simultaneously. We denote by F_{top} the force exerted at the top of the network and denote by λ the stretch of the network. The stretch is defined by the ratio of the current height of the network to its initial height, $\lambda = H/H_0$.

In experiments, the strength of a polymer network is defined by the maximum stress, i.e., the maximum force per unit area that the material can withstand before failure. In our two-dimensional network model, we define the strength as the maximum force divided by the width of the network, $F_{\max}/W$, where $F_{\max}$ is the maximum value of the force exerted at the top F_{top} during the deformation process. We interpret the stretch at the maximum force as the extensibility of the network model, denoted by $\lambda_{\max}$.

We consider an ideal network of size $N \times N$, in which all polymer chains have the same number of Kuhn segments, n. Since there is a single chain length, all chains will experience the same deformation and carry the same tensile force. If the force on individual chains exceeds the breaking force f_b, all chains break simultaneously. The force exerted at the top of the network reaches its maximum right before rupture. Note that there are $2N-1$ chains attached to the top of the network and each chain carries the breaking force f_b at this point. Thus, the strength of the ideal network, i.e. the maximum force at the top divided by the width of the network, is given by

$$F_{\max}/W = \frac{(2N-1) f_b \cos(\alpha^*)}{(N-1)\sqrt{n/3}}, \tag{4.24}$$

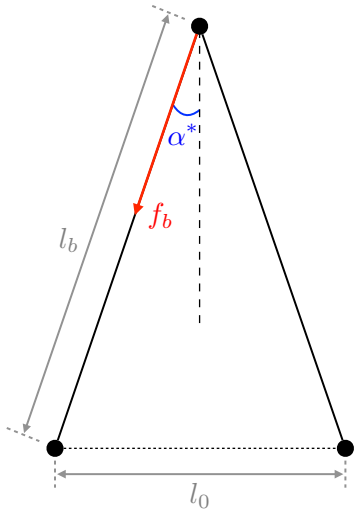

Figure 4.5: An illustration for the angle α^* between the polymer chain and the y-direction right before rupture. At this point, the polymer chain is stretched to length l_b while sustaining the breaking force f_b. The horizontal distance between two nodes equals the initial chain length l_0 at equilibrium.

where N is the network size, W is the width of the network given by (4.2), n is the number of Kuhn segments per chain, f_b is the breaking force, and α^* is the angle between the polymer chain and the y-direction right before rupture, as illustrated in Fig. 4.5. Here the breaking force is set to $f_b = 200$ for all chains.

We calculate the stretch of the network at the maximum force as follows. Initially, all polymer chains have the same equilibrium length $l_0 = \sqrt{n/3}$, where n is the number of Kuhn segments per chain. The initial height of the chain is $\sqrt{3}\, l_0/2$. At breaking, every chain is stretched to length l_b and its height becomes $l_b \cos(\alpha^*)$, where the angle α^* is displayed in Fig. 4.5. Then the extensibility of the ideal network, i.e. the stretch at the maximum force, is given by the ratio of the height at breaking to the initial height,

$$\lambda_{\max} = \frac{l_b \cos(\alpha^*)}{\sqrt{3}\, l_0/2} = \frac{l_b \cos(\alpha^*)}{\sqrt{n}/2}. \tag{4.25}$$

Finally, we calculate the angle α^* which represents the orientation of the polymer chain with respect to the y-direction right before rupture, as in Fig. 4.5. The distance between two nodes in the x-direction equals the equilibrium chain length $l_0 = \sqrt{n/3}$, where n is the number of Kuhn segments per chain. For the modified Langevin force-extension relationship, the fractional extension of the chain at breaking is found to be $l_b/n \approx 1.064$. In the ideal network, the number of Kuhn segments per chain, n, equals the mean of the shifted Weibull distribution, i.e. $\mu + n_{\min} = 60$. Thus, for the angle α^*, we have

$$\sin(\alpha^*) = \frac{0.5 l_0}{l_b} = \frac{0.5\sqrt{n/3}}{1.064\, n} \approx 0.0350, \tag{4.26}$$

$$\cos(\alpha^*) = \sqrt{1 - \sin^2(\alpha^*)} \approx 0.9994. \tag{4.27}$$

Then, for instance, the strength and extensibility of an ideal network of size 20×20 are respectively equal to

$$F_{\max}/W \approx \frac{39 \cdot 200 \cdot 0.9994}{19 \cdot \sqrt{60/3}} \approx 91.74,$$
$$\lambda_{\max} \approx \frac{60 \cdot 1.064 \cdot 0.9994}{\sqrt{60}/2} \approx 16.47.$$

The theoretical values of the strength $F_{\max}/W$ and extensibility $\lambda_{\max}$, respectively given by (4.24) and (4.25), for ideal networks of sizes 20×20, 40×40, 60×60, and 80×80, are provided in Tables 4.1 and 4.2. In addition, the computed values of the ideal strength and extensibility obtained from simulations are included for validation. We see that the computed values of the ideal strength are slightly lower than the theoretical values, and the discrepancy between them becomes smaller as the network size N increases.

Table 4.1: Theoretical and computed values of the strength $F_{\max}/W$ for ideal networks.

Network size	Theoretical $F_{\max}/W$	Computed $F_{\max}/W$
20×20	91.74	91.48
40×40	90.53	90.27
60×60	90.15	90.10
80×80	89.95	89.94

Table 4.2: Theoretical and computed values of the extensibility $\lambda_{\max}$ for ideal networks.

Network size	Theoretical $\lambda_{\max}$	Computed $\lambda_{\max}$
20×20	16.466	16.462
40×40	16.466	16.462
60×60	16.466	16.465
80×80	16.466	16.466

4.4.2 Stress-stretch curves and strength

We have obtained stress-stretch curves by conducting a series of numerical simulations of stretching networks up to complete fracture. Stress-stretch curves for small networks of sizes 20×20 and 40×40 were obtained by running 6 samples and 3 samples for each of the seven values of standard deviation σ, respectively. Due to the increased computational time required by simulations of large networks, we ran 2 samples for each setting of 60×60 networks and 1 sample for 80×80 networks.

In Fig. 4.6, we plot the force at the top normalized by the width of the network, F_{top}/W, versus the stretch λ for each of the four network sizes $N \times N$ and each of the seven values of standard deviation σ. In each plot, stress-stretch curves obtained using different samples for the same value of σ are shown in the same color, which allows for observation of sample-to-sample variations. In addition, stress-stretch curves for ideal networks are plotted for comparison (black graph).

In all these settings, stress-stretch curves for networks with scattered chain lengths exhibit much lower peak forces (i.e. strength) than that of the ideal network. For small values of σ, where the scatter in the number of Kuhn segments per chain is small, the force at the top drops down precipitously after it reaches the peak, indicating a cascade of chain breakage in the network. As σ increases, the number of Kuhn segments per chain scatters more, the force at the top has a lower peak and the peak force occurs at a lower stretch.

We observe a large reduction in strength, i.e. the maximum of the normalized force at the top, compared to the ideal network. With the J-shaped stress-stretch relationship, introducing a small amount of scatter in the number of Kuhn segments per chain greatly

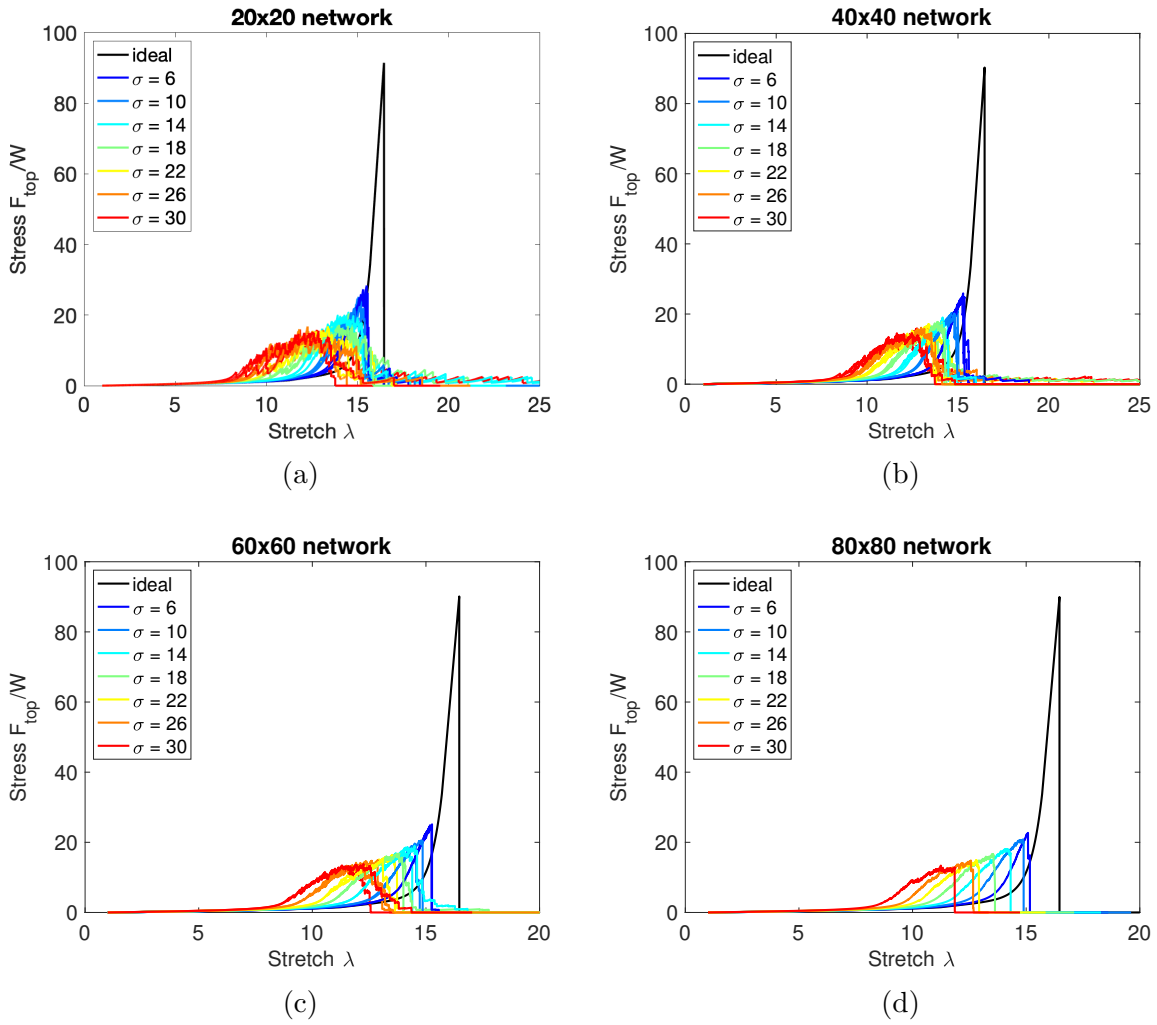

Figure 4.6: Force at the top normalized by the width (i.e. stress) F_{top}/W versus stretch λ for various values of standard deviation σ for (a) 20×20 networks, (b) 40×40 networks, (c) 60×60 networks, and (d) 80×80 networks. For each σ, stress-stretch curves were obtained using 5 samples, 3 samples, 2 samples, and 1 sample, respectively, for networks of the four sizes. Black graphs correspond to stress-stretch curves for ideal networks.

reduces strength. For instance, for a small scatter $\sigma = 6$ the strength is reduced to less than 30% of the strength of the ideal network. At the largest scatter $\sigma = 30$, the strength is further reduced to approximately 15% of the ideal strength. Moreover, we can see from Fig. 4.6 that the variation in strength from sample to sample is relatively small.

We extract the strength values from the stress-stretch curves in Fig. 4.6 and average them over different samples for each setting. Graphs of the strength $F_{\max}/W$ as a function of the standard deviation σ for networks of the four different sizes are plotted in Fig. 4.7. The variation in strength between samples is illustrated by the error bars. As the scatter in chain lengths increases, we observe a nonlinearly scaling reduction in strength compared to the ideal network with no scatter ($\sigma = 0$). This nonlinear effect is due to the use of the J-shaped stress-stretch relationship. On the other hand, we see that the strength is relatively consistent among different network sizes. There is a slight decrease in strength as the network size N increases.

Finally, we discuss the effect of the size of the network on the behavior of stress-stretch curves and the resulting breaking scenarios. As seen in Fig. 4.6, stress-stretch curves for small networks of sizes 20×20 and 40×40 exhibit a zig-zag pattern around peak forces, especially when the scatter in chain lengths is large. The force at the top remains high for a certain range of stretch before eventually collapsing. Moreover, a long tail of small forces is observed in stress-stretch curves of small networks. As the network size N increases, stress-stretch curves become smoother and the force at the top tends to drop down shortly after reaching the peak. In particular, we observe a cascade of chain breakage for all values of σ in 80×80 networks (see Fig. 4.6(d)).

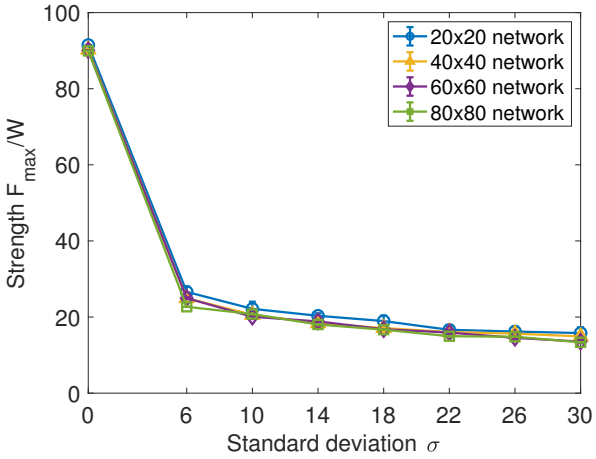

Figure 4.7: The effect of the scatter in chain lengths, characterized by standard deviation σ, on the maximum stress (i.e. strength) $F_{\max}/W$ of the network model for the four network sizes. The strength values obtained from multiple samples are averaged. The variation between samples is shown with the error bars.

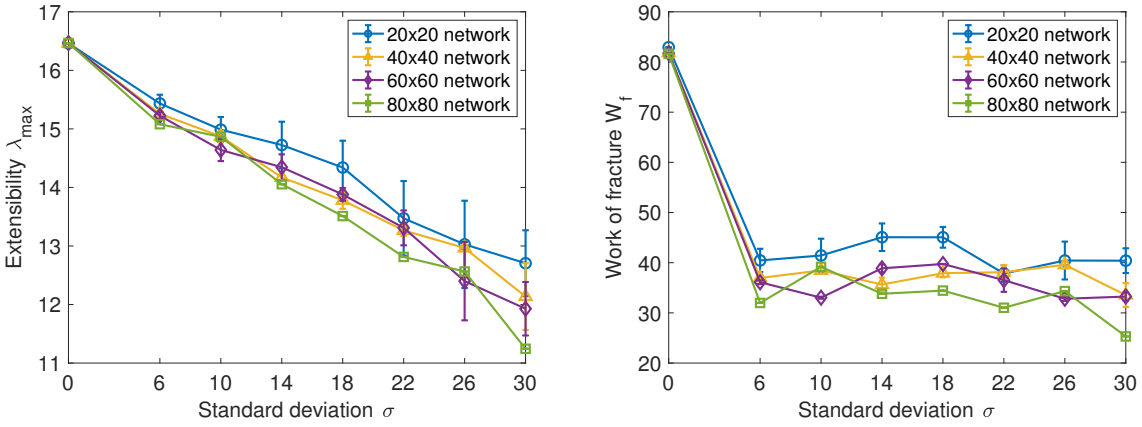

(a) (b)

Figure 4.8: The effect of the scatter in chain lengths, characterized by standard deviation σ, on the (a) extensibility $\lambda_{\max}$ and (b) work of fracture W_f of the network model for the four network sizes. The values of $\lambda_{\max}$ and W_f obtained from multiple samples are averaged. The variation between samples is shown with the error bars.

4.4.3 Extensibility and work of fracture

We define the extensibility $\lambda_{\max}$ by the stretch at which the stress-stretch curve peaks. In Fig. 4.8(a), the extensibility values averaged over multiple samples are plotted against the standard deviation σ of the number of Kuhn segments per chain for networks of the four sizes. The error bars represent the variation between samples. We observe a linearly scaling decrease in extensibility as the number of Kuhn segments per chain scatters more. Furthermore, the variation in extensibility between samples becomes larger as σ increases. This is related to the zig-zag behavior of stress-stretch curves for small networks and large values of σ, as in Fig. 4.6. Indeed, there exists a certain range of stretch at which the force at the top of the network remains high and close to the peak force.

Another important mechanical property is the work of fracture that measures the energy absorbed by the network before failure. In experiments, the work of fracture is defined by the area under the stress-stretch curve up to the point of failure. Here we focus on the mechanical behavior up to the peak of the stress-stretch curve, which corresponds to the strength, and ignore the long tail of small forces. We define the work of fracture W_f by integrating the area under the stress-stretch curve up to the extensibility $\lambda_{\max}$.

In Fig. 4.8(b) we plot the work of fracture W_f against the standard deviation σ for networks of the four different sizes. The work values are obtained from the stress-stretch curves shown in Fig. 4.6 and averaged over different samples for each σ. The variation between samples is illustrated by the error bars. Comparing Figs. 4.7 and 4.8(b), we obtain a similar reduction in work of fracture as we observe in the strength of the network model. The variation in work of fracture is also small from sample to sample.

4.4.4 Power law relationship

We now quantify the effect of the scatter in the number of Kuhn segments per chain on the strength of the network model. Specifically, we demonstrate a power law dependence of the strength $F_{\max}/W$ on the standard deviation σ of the number of Kuhn segments per chain. This finding will be compared to the power law relationship derived in the parallel chain model, as discussed in Chapter 3. Note that in the parallel chain model we use the coefficient of variation, $C_v = \sigma/\mu$, to characterize the scatter in chain lengths, whereas in the network model we simply use the standard deviation σ to characterize the scatter.

To compare the reduction in strength for networks of different sizes, we normalize the strength $F_{\max}/W$ by the ideal strength $F_{\max,\text{ideal}}/W$. The resulting ratio, $F_{\max}/F_{\max,\text{ideal}}$, is referred to as the normalized strength. In Fig. 4.9(a) we plot the normalized strength $F_{\max}/F_{\max,\text{ideal}}$ against the standard deviation σ on the log-log scale for networks of the four different sizes. The curves for large networks fluctuate due to the limited number of samples implemented in the simulations. Despite this fluctuation, all curves are nearly linear on the log-log scale. Hence, we seek to quantify a power law between the normalized strength $F_{\max}/F_{\max,\text{ideal}}$ and the standard deviation σ of the form

$$F_{\max}/F_{\max,\text{ideal}} = C\sigma^p, \tag{4.28}$$

where C and p are constants that need to be determined. Least squares fits to the power laws for networks of the four sizes are shown in Table 4.3, where the power p is the same for all network sizes and the constant C varies with the network size N (see Fig. 4.9(b)).

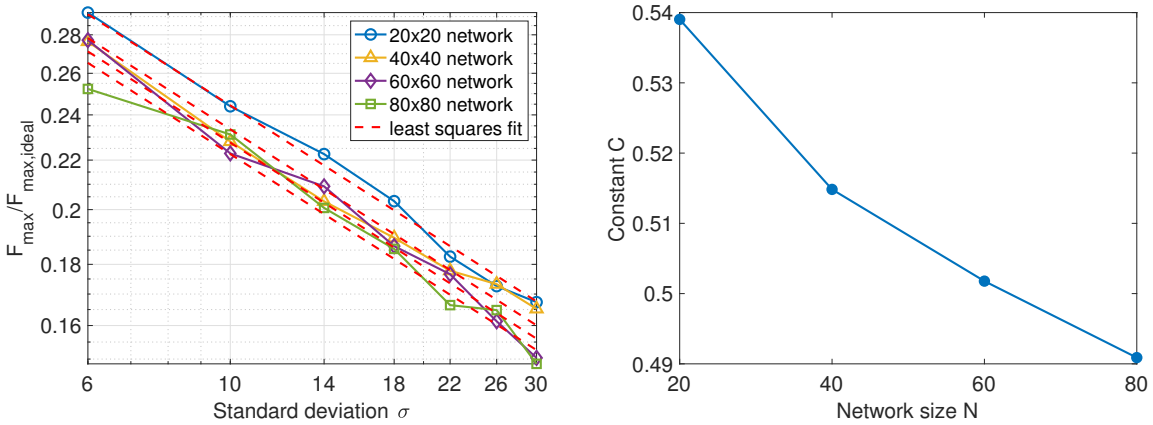

(a) (b)

Figure 4.9: (a): The power law between the normalized strength $F_{\max}/F_{\max,\text{ideal}}$ of the network model and the standard deviation σ of the number of Kuhn segments per chain for the four network sizes. The red dashed line is the least squares fit to the power law relationship. (b): The constant C as a function of the network size N.

Table 4.3: The power law between the normalized strength $F_{\max}/F_{\max,\text{ideal}}$ and the standard deviation σ for the network model, in comparison with the empirical power law observed for the parallel chain model with the modified Langevin force-extension relationship.

	Least squares fit to $F_{\max}/F_{\max,\text{ideal}} = C\sigma^p$
20×20 network	$0.539 \cdot \sigma^{-0.334}$
40×40 network	$0.515 \cdot \sigma^{-0.334}$
60×60 network	$0.502 \cdot \sigma^{-0.334}$
80×80 network	$0.491 \cdot \sigma^{-0.334}$
parallel chain model	$0.938 \cdot \sigma^{-0.955}$

4.5 Discussion

Our network model suggests that, the scatter in chain lengths combined with the J-shaped stress-stretch relationship leads to a significant reduction in strength compared to the ideal network, while keeping the variation in strength small from sample to sample. Specifically, we find that the strength of the network model can be reduced to as low as 15% of the strength of the ideal network. The use of the J-shaped stress-stretch relationship results in a nonlinearly scaling decrease in strength as the scatter in chain lengths increases.

We quantify the nonlinear effect of the scatter in chain lengths on the strength of the network model using a power law relationship. The scatter in chain lengths is characterized by the standard deviation σ of the number of Kuhn segments per chain. We obtain the following power law relationship between the normalized strength $F_{\max}/F_{\max,\text{ideal}}$ and the standard deviation σ for networks of different sizes:

$$F_{\max}/F_{\max,\text{ideal}} = C\sigma^{-0.334}. \tag{4.29}$$

The power of σ is consistent for all network sizes, indicating a universal behavior of the strength decay, while the constant C depends on the network size N.

We observe an interesting pattern in the lines of least squares fits to the power laws as in Fig. 4.9(a). The red dashed lines are almost equidistant from each other for network sizes larger than 40×40. This observation suggests that the constant C in the power law decreases nearly linearly as the network size N increases, as demonstrated in Fig. 4.9(b). Due to this fact, we cannot further extrapolate the power law to larger network sizes.

A comparison between the power laws observed for the network model and the parallel chain model in the same setting is presented in Table 4.3. In both models, each polymer chain is represented by a freely-jointed chain with the modified Langevin force-extension relationship, and the number of Kuhn segments per chain obeys the Weibull distribution. We see that the decay rate of the normalized strength $F_{\max}/F_{\max,\text{ideal}}$ with respect to the standard deviation σ in the parallel chain model is faster than that in the network model. The empirical values of the power of σ in the two models differ by about a factor of 3.

The discrepancy in the decay rate of strength between the network model and the parallel chain model originates from their underlying structural differences. The network model takes into account the interactions between polymer chains, which allows for load sharing and stress redistribution. Each individual chain in the network represents a small segment that is part of various paths traveling from the bottom to the top of the network. When a chain breaks, the stress carried by that segment is released, causing a redistribution of the load to the remaining chains in the network. As a result, the failure of a single chain contributes to a portion of the overall strength reduction.

By contrast, interchain interactions are ignored in the parallel chain model, where all polymer chains are stretched in parallel with their ends attached to two rigid plates. The entire chain between the rigid plates fails when any of its Kuhn segments breaks, and the failure of each chain is independent. Therefore, the presence of shorter chains breaking before longer chains has a more pronounced impact on the strength predicted by the parallel chain model, leading to a faster decay rate of strength compared to the network model. Despite this discrepancy, our findings suggest that the strength scaling with the scatter in chain lengths by a power law may be a universal behavior in polymer networks.

In addition to strength, we have also investigated the effect of the scatter in chain lengths on two other important mechanical properties: extensibility and work of fracture. We compare the simulation results with the experimental data for hydrogels [10]. In the experiment, the extensibility of an ideal network is estimated to be about 41, which is much larger than the measured extensibility of 10.1 for the polyacrylamide (PAAM) hydrogel. The sample of the hydrogel used in [10] has $n = 1786$ Kuhn segments per chain, whereas in our network model the average number of Kuhn segments per chain is $n = 60$.

The ideal extensibility of our network model is found to be 16.5, lower than the theoretical estimate of 41 given in [10]. This discrepancy is due to the much shorter chain lengths used in the simulations compared to the real polymer chains in the hydrogel sample. At the largest scatter characterized by the standard deviation $\sigma = 30$, the extensibility of our network model is reduced to about 11.2, which is comparable to the experimental measurement for the PAAM hydrogel [10]. However, the reduction in extensibility obtained by our network model is not large enough to account for the experimentally measured reduction by about a factor of 4 compared to the ideal network.

On the other hand, the work of fracture of the hydrogel sample is lower than that of an ideal network by about four orders of magnitude [10]. This reduction in work of fracture is interpreted as a measure of network imperfection, such as variation in chain lengths and chain entanglements. Our network model captures the large reduction in work of fracture even with a small amount of scatter in chain lengths introduced, thanks to the use of the J-shaped stress-stretch relationship. Although the magnitude of the reduction is far smaller than that observed in the experiment [10], our findings demonstrate the effect of network imperfection on the fracture properties of polymer networks.

Finally, we compare our network model to the stochastic network model developed by Lavoie and Suo [40]. The authors simulate a network model in which the constituents are linearly elastic members forming a periodic triangular lattice. The stochastic nature is introduced by assigning a random strength to each member of the network, which follows the Weibull distribution. In [40], it is shown that the strength of the stochastic network is an outcome of a competition between stress concentration at the crack tip and statistical distribution of member strength. When the member strength scatters narrowly, the stress concentration prevails, and the crack greatly reduces the strength of the network, indicating flaw sensitivity. As the scatter in member strength increases, the statistical distribution prevails, and the network strength becomes insensitive to the crack. These findings provide insight into the competing effects of flaws and stochastic member strength on reducing the overall strength of the network, which is indeed a manifestation of network imperfection.

The key difference between our network model and the stochastic network in [40] lies in the introduction of statistical variation in local properties. We assume that the breaking force (i.e. strength) is the same for all members, while the lengths of polymer chains are scattered according to the Weibull distribution. Nonlinear chain elasticity is incorporated into our model by considering a J-shaped stress-stretch relationship, which enables a significant reduction in the strength of the network. The mechanical response predicted by our network model is qualitatively similar to the findings from [40], providing further insight into the quantification of network imperfection.

Chapter 5: Breaking mechanism: shortest paths and holes

Thus far, we have investigated the effect of the scatter in chain lengths on the fracture properties of polymer networks using two different models: the parallel chain model and the network model. In both models, the reduction in strength obtained from simulations explains a portion of the giant discrepancy between the experimentally measured strength of hydrogels and the strength of covalent bonds [10]. The parallel chain model allows for simple calculations and is amenable for analysis by analytical tools. However, it does not take into account the effects of stress concentration and interchain interaction present in the real polymer network. On the other hand, the network model, designed to mimic the polymer skeleton of hydrogels, is only amenable for numerical simulations. One limitation of the network model is that we cannot extrapolate the power law between the strength and the scatter in chain lengths to larger network sizes, and simulations of larger networks are much more computationally demanding.

In this chapter, we shift our focus towards analyzing the microscopic characteristics and the breaking mechanism of the polymer network. Using the network model developed in Chapter 4, we analyze the topology of the network by computing the *shortest paths* between the top and bottom boundaries (see Fig. 5.1(a)). We find that chains are more likely to break on the global minimum shortest path, or on the shortest path with length

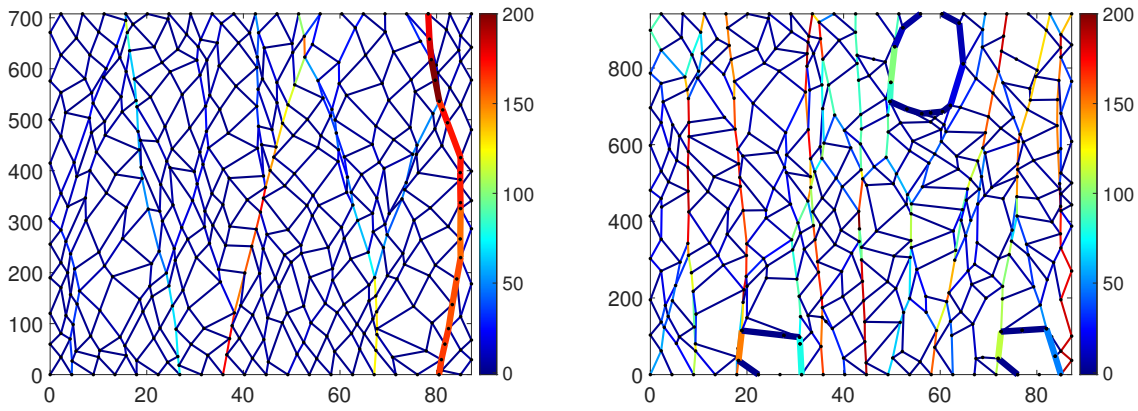

(a) The minimum shortest path

(b) Isolated holes

Figure 5.1: (a): The minimum shortest path (highlighted) between the top and bottom boundaries of the network. (b): The presence of isolated holes (highlighted) at peak force. The colorcode shows the stress of individual links.

very close to the global minimum. This finding suggests that, during the stretching process, broken links that concentrate stress can be characterized through a microstructural feature associated with the shortest paths in the network. We seek to understand the connection between concentration of stress and the microstructure of the network, which provides valuable insights into the underlying fracture mechanism. In addition, we demonstrate that the characterization of broken links through the shortest paths can serve as an amenable tool for predicting a subset of weak links that tend to break shortly.

The length distribution of shortest paths between well-separated crosslinks has been studied for bond-breaking events in multi-network elastomers [27]. The length of a path connecting two distant crosslinks is defined as the sum of the number of Kuhn segments per chain along the path. Among multiple paths connecting the two crosslinks, the path with the lowest total weight is defined as the shortest path. In [27], it is shown that the average shortest path length between far-away crosslinks is the key microstructural feature that controls both molecular-level bond-breaking events and the macroscopic mechanical

response of elastomers. In this work, we relate the strength (i.e. peak force) of our network model to the average shortest path length at initialization. We find that the peak force occurs when the shortest path with average length at initialization becomes the global minimum shortest path that concentrates the majority of the stress.

Furthermore, the presence of isolated holes is observed when the network model reaches the peak force, as illustrated in Fig. 5.1(b). To gain a better understanding of this phenomenon, we study the formation and growth of *holes* while keeping track of the force exerted at the top of the network throughout the stretching process. We demonstrate phase transitions in the network topology as the applied force grows, reaches the peak, and eventually drops down to zero.

5.1 Introduction

Elastomers are polymer materials that can sustain large reversible strain and are essential components for stretchable electronics. Their elasticity and stretchability make them suitable for the development of novel wearable and biological applications [57, 58]. The mechanical properties of unfilled elastomers can be improved by adding easier-to-break crosslinks [59], for instance, through a multi-network structure [18, 60]. The introduction of these crosslinks, however, also leads to strong stress-strain hysteresis that is similar to the Mullins effect [16], indicating strain-induced damage. The mechanism controlling the pattern of bond breaking in multi-network elastomers is *not* yet understood. In particular, identifying a microstructural parameter for the polymer network that explains the hysteretic stress-strain behavior is of critical importance for understanding the damage evolution.

Recently, Yin et al. [27] have investigated the strain-induced damage in multi-network elastomers using coarse-grained molecular dynamics (CGMD) simulations. By analyzing the topology of the elastomer network, they have examined multiple candidates for the microstructural parameter that controls the strain-induced damage evolution. Based on the results from CGMD simulations, the authors propose that a suitable microstructural parameter needs to satisfy three criteria: (i) be anisotropic, (ii) be hysteretic with strain, and (iii) controls the stress-strain response. The controlling microstructural parameter connects molecular-level bond-breaking events to the macroscopic mechanical behavior of elastomers, which can serve as a foundation for the development of physics-based models and the design of novel materials with tunable mechanical properties [61, 62].

In [27], the topological analyses of the elastomer network are performed by computing the shortest paths (SPs) between well-separated crosslinks and examining the distribution of SP lengths. As shown in Fig. 5.2, the authors define a network in which the crosslinked beads are represented as vertices and the polymer chains connecting the beads as edges. The weight of each edge equals the number of Kuhn segments per chain. For each pair of beads (e.g. A-A'), there are multiple paths connecting the two vertices in this network. The shortest path (SP) refers to the path with the minimum total length, where the length of a path is defined as the sum of the weights of its constituent edges.

Recall that the goal of [27] is to identify a *global* parameter of the network topology that characterizes the microstructure of strain-induced damage evolution. Thus, to serve as the controlling parameter, the shortest paths need to be computed between pairs of beads that are separated by a large distance. The length distribution of shortest paths is then tested against the three criteria given above.

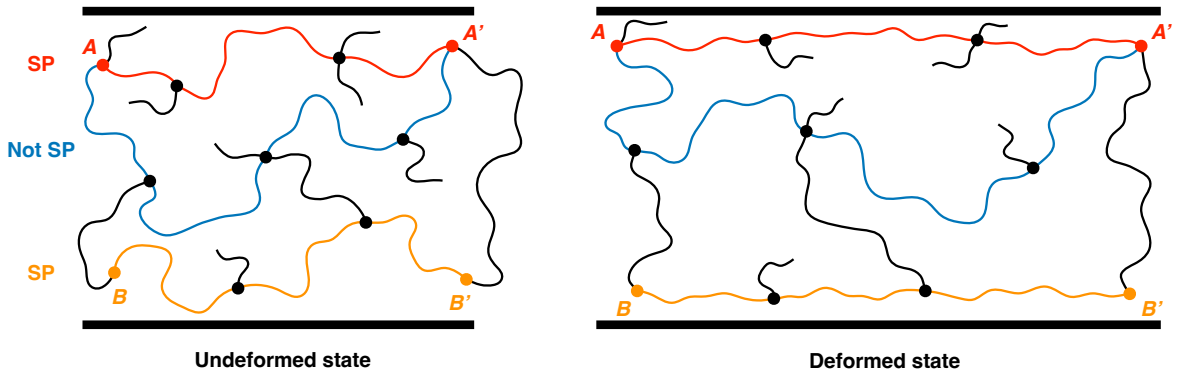

Figure 5.2: Schematic of the polymer network in the undeformed state and deformed state. A-A' and B-B' are example pairs of vertices separated by a large distance. Two different paths connecting A-A' are colored blue and red, and the red path is the shortest path (SP). The shortest path (SP) connecting B-B' is colored orange.

The key finding of [27] reveals that bond-breaking events in the elastomer network are governed by the evolution of the global shortest path length between well-separated crosslinks. It is shown that the length distribution of shortest paths is both anisotropic and hysteretic with strain, and it controls the mechanical response. The average shortest path length is identified as the controlling microstructural parameter for damage evolution. Furthermore, the authors demonstrate that bond breaking in the polymer network follows a predictable pattern, and specifically, they find that every bond-breaking event occurs on one or more shortest paths in the network. These findings establish an explicit connection between the molecular structure and the macroscopic mechanical behavior, and can be used to develop physics-based constitutive models capable of predicting the damage evolution with strain in highly stretchable materials.

The authors of [27] also note an interesting correlation between bond-breaking events and a topological property called *betweenness centrality* [63]. The betweenness centrality of a bond is determined by the number of shortest paths (SPs) passing through that bond.

The simulation results from [27] show that bond-breaking events tend to occur on bonds with a high betweenness centrality value. In other words, the bonds that are traversed by a large number of shortest paths are more likely to experience breakage. This correlation suggests a quantitative approach to characterize and predict bond breaking in the polymer network, which we will investigate in this chapter.

The primary goal of this chapter is to understand stress concentration in the polymer network by performing shortest path analyses for the network model discussed in Chapter 4. We are interested in characterizing the broken links during deformation through microscopic characteristics of the network in both qualitative and quantitative ways. The shortest paths in our network model are computed between the nodes on the top and bottom boundaries. At every breakage, we identify the minimum shortest path where the broken link occurs as well as the global minimum shortest path. First, we check whether these two paths are identical, that is, whether links break on the global minimum shortest path in the network. Then, to quantitatively characterize which links tend to break, we count the number of shortest paths passing through each individual link in the network, and determine whether broken links belong to significantly more shortest paths than other links. The statistics for shortest path analyses are summarized in Section 5.3.

The second question we seek to understand is how to determine the presence of the peak force (i.e. strength) through the microstructural evolution of the polymer network. We answer this question from two perspectives. One approach is to analyze the distribution of shortest path lengths as it evolves with deformation, and identify a parameter that relates to the peak force. Another perspective involves investigating the connection between the magnitude of the applied force and formation of holes in the network, see Section 5.4.

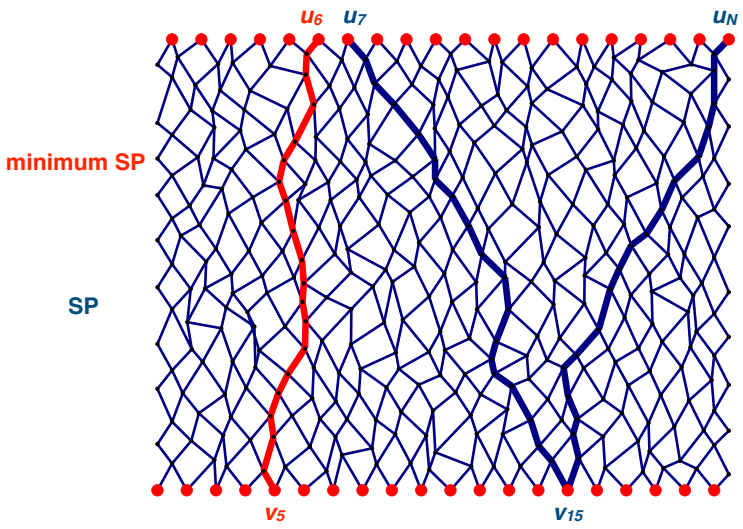

Figure 5.3: The shortest paths between the top and bottom boundary nodes. The red path is the minimum shortest path (SP). The blue paths are two samples of shortest paths.

5.2 Shortest paths in the network model

We consider the network model developed in Chapter 4, in which $N \times N$ nodes are connected into a diamond grid by links, as depicted in Fig. 5.3. Each link between the neighboring nodes represents a polymer chain consisting of a number of Kuhn segments. The network model is initialized with statistical variation in lengths of polymer chains. Specifically, the number of Kuhn segments per chain, n, follows the shifted and discretized Weibull distribution given by (4.4). The minimal admissible number of Kuhn segments (i.e. the shift) is $n_{\min} = 10$. The mean of the Weibull distribution is fixed, $\mu = 50$, while the standard deviation σ varies in the range $6 \leq \sigma \leq 30$. In the remainder of this chapter, we will investigate the microscopic characteristics of the network samples with the largest scatter in chain lengths, which corresponds to the standard deviation $\sigma = 30$. As suggested by [27], we will analyze the shortest paths between the top and bottom boundary nodes.

Below we introduce the definitions and notations related to the shortest paths in our network model. The shortest paths are computed between the top and bottom boundaries of the network. We denote the sets of top and bottom boundary nodes, respectively, by

$$\mathcal{I}_t = \{u_1, u_2, \ldots, u_N\},$$

$$\mathcal{I}_b = \{v_1, v_2, \ldots, v_N\}.$$

The shortest paths are defined in the same manner as in [27]. The network model can be represented as a weighted graph, where each polymer chain corresponds to an edge with weight equal to the number of Kuhn segments per chain, n. The length of a path P in the network is defined as the sum of the weights of the edges on the path, i.e.

$$l(P) = \sum_{e \in P} n_e,$$

where $e \in P$ is the edge on path P and n_e is the number of Kuhn segments in the edge. As seen in Fig. 5.3, there are multiple paths connecting each pair of nodes on the top and bottom boundaries. Among these paths, the one with the lowest total weight is defined as the shortest path (SP).

We denote by P_{ij} the shortest path between each pair of nodes u_i and v_j on the top and bottom boundaries, respectively. The distance between nodes u_i and v_j is the length of the shortest path connecting them, i.e. $d_{ij} = l(P_{ij})$. Moreover, we denote the set of shortest paths between all pairs of top and bottom boundary nodes by $\mathcal{P} = \{P_{ij}\}$, and denote the set of shortest path (SP) lengths by $D = \{d_{ij}\}$.

The minimum SP. We define the minimum shortest path (SP) in the network as the shortest path with the minimum length in the set $\mathcal{P}$, and denote it by

$$P_{\min} = \arg\min_{P_{ij} \in \mathcal{P}} \ l(P_{ij}).$$

We denote the length of the minimum SP, i.e. the minimum length in the set D, by

$$d_{\min} = \min_{d_{ij} \in D} \ d_{ij}.$$

The minimum SP in a 20×20 network at initialization is illustrated in Fig. 5.3 (red path).

When a link in the network breaks, we identify a subset of shortest paths that pass through the broken link. We denote by $\mathcal{P}^{br}$ the subset of $\mathcal{P}$ in which the shortest path contains the broken link, and by D^{br} the corresponding subset of shortest path lengths. Furthermore, we identify the minimum shortest path (SP) that contains the broken link. We denote the minimum SP in the subset $\mathcal{P}^{br}$ and its length, respectively, by

$$P^{br}_{\min} = \arg\min_{P_{ij} \in \mathcal{P}^{br}} \ l(P_{ij}),$$

$$d^{br}_{\min} = \min_{d_{ij} \in D^{br}} \ d_{ij}.$$

It is of interest to compare the two minimum paths, $P_{\min}$ and $P^{br}_{\min}$, and determine if they are the same path. For illustration, two breaking scenarios are presented in Fig. 5.4. If $P_{\min}$ and $P^{br}_{\min}$ are identical, it indicates that the broken link tends to occur on the global minimum SP. In the other case, we will quantify the difference in their path lengths.

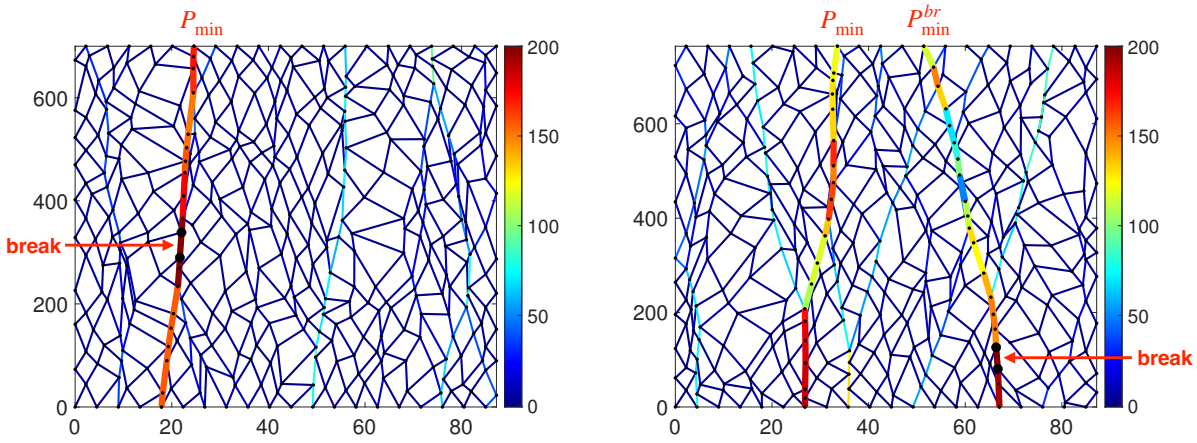

(a) $P_{\min} = P^{br}_{\min}$ (b) $P_{\min} \neq P^{br}_{\min}$

Figure 5.4: Breaking scenarios showing the comparison of two paths: the global minimum shortest path, $P_{\min}$, and the minimum shortest path passing through the broken link, $P^{br}_{\min}$. (a): $P^{br}_{\min}$ coincides with $P_{\min}$, i.e., the link breaks on the global minimum shortest path. (b): $P^{br}_{\min}$ (right) is different from $P_{\min}$ (left), but the lengths of two paths are very close.

Betweenness centrality. As mentioned above, betweenness centrality is a network measure that can be used to characterize the broken links during the deformation process. The betweenness centrality of an edge is defined as the number of shortest paths passing through that edge. In our network model, for each individual link, i.e. each edge $e \in E$, we count the number of shortest paths between pairs of nodes on the top and bottom boundaries that pass through the link:

$$c_e = \sum_{i,j=1}^{N} \sigma_{ij}(e),$$

where $\sigma_{ij}(e)$ represents the number of shortest paths between top boundary node u_i and bottom boundary node v_j that pass through e. Moreover, we denote the set of centrality values for all links in the network by $C = \{c_e\}_{e \in E}$. We will examine whether broken links have a significantly higher centrality value in the set C.

Table 5.1: Notations for shortest paths in the network model.

Notation	Meaning
$\mathcal{I}_t = \{u_i\}_{i=1}^N$	Nodes on the top boundary
$\mathcal{I}_b = \{v_j\}_{j=1}^N$	Nodes on the bottom boundary
$\mathcal{P} = \{P_{ij}\}$	Set of shortest paths between all pairs of node u_i and node v_j
$D = \{d_{ij}\}$	Set of shortest path lengths between node u_i and node v_j
$\mathcal{P}^{br} \subset \mathcal{P}$	Subset of shortest paths that pass through the broken link
$D^{br} \subset D$	Subset of shortest path lengths that contain the broken link
$P_{\min}$	The global minimum shortest path in the network
$d_{\min}$	Length of $P_{\min}$, i.e. the minimum length in D
$P_{\min}^{br}$	The minimum shortest path passing through the broken link
$d_{\min}^{br}$	Length of $P_{\min}^{br}$, i.e. the minimum length in D^{br}
n_e	Number of Kuhn segments in each link
c_e	Number of shortest paths passing through each link, i.e. centrality
$C = \{c_e\}_{e \in E}$	Set of centrality values for all links in the network
n_{br}	Number of Kuhn segments in the broken link
c_{br}	Number of shortest paths passing through the broken link

5.3 Statistics for shortest paths

In this section, we present the statistics and analyses of the shortest paths in the network model as it undergoes deformation. Our investigation focuses on the following two key questions:

(i) *Understanding where the stress tends to concentrate.* We seek to identify the weak links in the polymer network. Since the shortest paths concentrate most of the stress, we will focus on understanding the role of shortest paths in characterizing the broken links during deformation. We will investigate both qualitatively and quantitatively the characterization of broken links through analyses of shortest paths, which can serve as a tool for predicting the weak links in the network.

(ii) *Understanding when the peak force occurs.* The second question we seek to answer is how the microstructural evolution of the polymer network controls the macroscopic mechanical properties, such as strength and extensibility. We investigate this question by analyzing the evolution of the shortest path (SP) length distribution, as suggested by Yin et al. [27]. We will identify a microstructural parameter for the network model that indicates when the peak force (i.e. strength) is achieved during deformation.

We conduct analyses of shortest paths on various samples of the network model obtained from numerical simulations in Chapter 4. We take the four different network sizes $N \times N$ for $N = 20$, 40, 60, and 80. For each network size, we consider 2 samples with the largest scatter in chain lengths, corresponding to the standard deviation $\sigma = 30$.

5.3.1 The minimum shortest path

To understand the breaking mechanism of the polymer network, it is helpful to first determine whether broken links tend to occur on the global minimum shortest path (SP). In our network model, we compute the set of shortest paths between all pairs of top and bottom boundary nodes, $\mathcal{P}$, in which we identify the global minimum shortest path, $P_{\min}$. When a link in the network breaks, we find the minimum shortest path that contains the broken link, $P^{br}_{\min}$. The lengths of these two paths are denoted by $d_{\min}$ and $d^{br}_{\min}$ respectively.

It is of interest to examine whether the two minimum paths, $P_{\min}$ and $P^{br}_{\min}$, coincide for every broken link as the network undergoes deformation. In other words, we aim to address the question of how well the global minimum shortest path can capture the events of link breakage. We note that while the network is being stretched, links fluctuate in space, but the shortest paths defined here should remain unchanged if there were no link-breaking events to alter the topology of the network. The set of all-pairs shortest paths $\mathcal{P}$ needs to be recomputed after every breaking event.

We present the comparison of paths $P_{\min}$ and $P^{br}_{\min}$ for every broken link in Fig. 5.5. The red graph represents the evolution of the length of the global minimum shortest path, $P_{\min}$, as the number of broken links increases. The blue dots correspond to the length of path $P^{br}_{\min}$, and they are marked to indicate situations where $P_{\min}$ and $P^{br}_{\min}$ are *not* the same path. In other words, these are the cases where broken links do not occur on the global minimum shortest path $P_{\min}$. The results are shown for network samples of the four different sizes. Interestingly, we see that although many links do not break on the global minimum shortest path, the length of $P^{br}_{\min}$ is very close to that of $P_{\min}$ for all broken links.

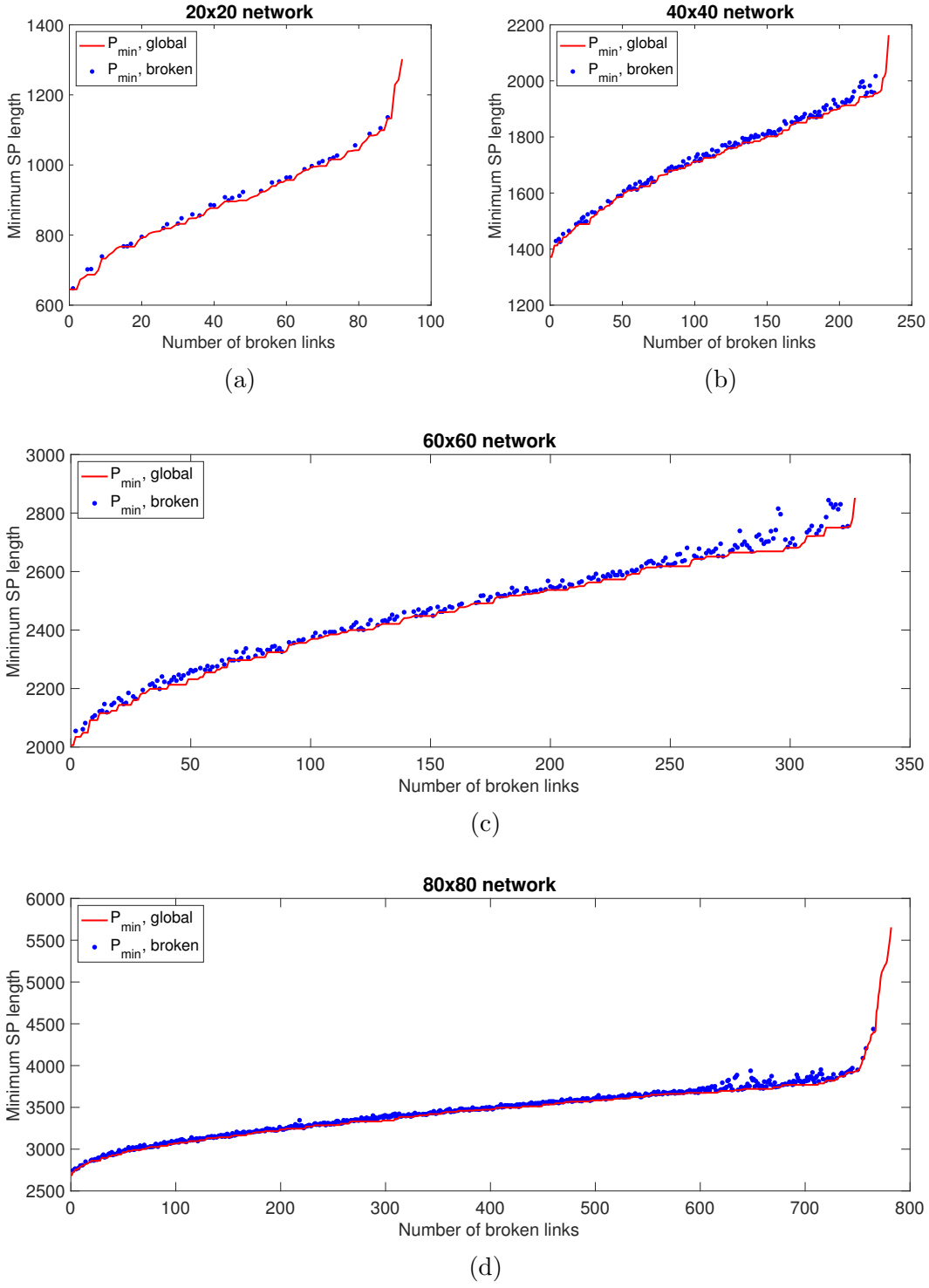

Figure 5.5: Comparison of the global minimum shortest path, $P_{\min}$, and the minimum shortest path that contains the broken link, $P^{br}_{\min}$, at every breakage during deformation. The red graph represents the evolution of the length of $P_{\min}$. The blue dots correspond to the length of $P^{br}_{\min}$, marked in situations where $P^{br}_{\min}$ is different from $P_{\min}$.

Furthermore, we measure how close it is between the path lengths of $P_{\min}$ and $P_{\min}^{br}$. For a network of size $N \times N$, the set $\mathcal{P}$ has a total number of N^2 shortest paths between all pairs of top and bottom boundary nodes. Let D denote the set of lengths of these N^2 shortest paths. The length of $P_{\min}$, denoted by $d_{\min}$, is the minimum length in the set D. To quantify the difference between $d_{\min}$ and $d_{\min}^{br}$, where $d_{\min}^{br}$ denotes the length of $P_{\min}^{br}$, we measure the percentile rank of $d_{\min}^{br}$ in the set D.

We define the percentile rank p for the shortest path $P_{\min}^{br}$ that contains the broken link by measuring the percentile rank of its length $d_{\min}^{br}$ in the set D at every breakage and taking the maximum value over all broken links. It quantifies the lowest $p\%$ of shortest paths in the set $\mathcal{P}$, whose lengths are below the shortest path passing through broken links. We identify these $p\%$ of shortest paths as the weak paths in the network. In other words, broken links tend to occur on the lowest $p\%$ of shortest paths with length very close to the global minimum length. The statistics for the percentile rank p are shown in Table 5.2.

Table 5.2: The percentile rank p for the shortest path $P_{\min}^{br}$ that contains the broken link. This quantity identifies the lowest $p\%$ of shortest paths where links are more likely to break.

Network size	Lowest $p\%$, Run 1	Lowest $p\%$, Run 2
20×20	4.25%	2.75%
40×40	6.50%	7.20%
60×60	11.53%	11.92%
80×80	10.25%	11.80%

5.3.2 Characterization of broken links

Thus far, we have confirmed that broken links tend to occur on the global minimum shortest path, or on the shortest path with length very close to the global minimum length. The lowest $p\%$ of shortest paths are identified as weak paths. We now seek to quantitatively characterize which links on these weak paths are more likely to break.

In our network model, for each individual link, i.e. each edge $e \in E$, we count the number of shortest paths passing through the link, denoted by c_e. This number represents the betweenness centrality of a link. Let C denote the set of centrality values for all links in the network, i.e. $C = \{c_e\}_{e \in E}$. It is of interest to examine whether the links that belong to a large number of shortest paths tend to break, or equivalently, whether broken links have a significantly higher centrality value in the set C.

During deformation, at every breakage, we find the number of shortest paths passing through the broken link, c_{br}, and compare it to the average number of shortest paths passing through each individual link, μ_C. In Fig. 5.6 we plot the centrality value c_{br} for every broken link throughout the stretching process. The blue circles indicate broken links that occur entirely on the interior of the network, while the blue dots indicate broken links with one end connected to the boundary nodes. We will refer to these two types of broken links as interior links and boundary links, respectively. Moreover, the average value μ_C and the standard deviation σ_C of the set C are plotted in Fig. 5.6 for comparison. The three red curves from bottom to top correspond to μ_C, $\mu_C + \sigma_C$, and $\mu_C + 2\sigma_C$, respectively.

We can see from Fig. 5.6 that the centrality value of broken links, c_{br}, is significantly higher than the average number of shortest paths passing through each individual link, μ_C.

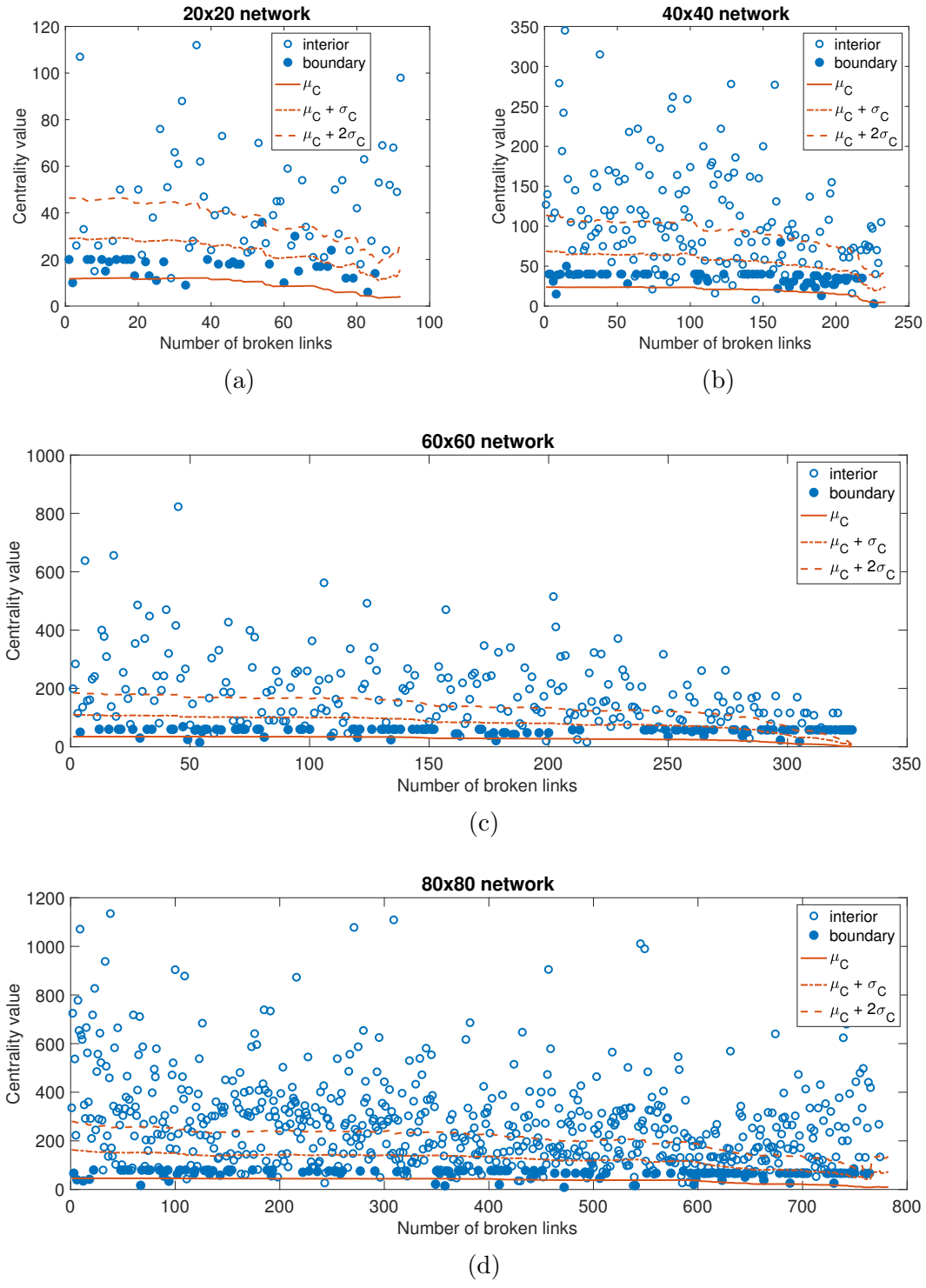

Figure 5.6: The centrality value of the broken link c_{br} at every breakage during deformation, defined as the number of shortest paths passing through the link. The blue circles indicate interior broken links, while the blue dots indicate boundary broken links. The red curves are shown for comparison, corresponding to μ_C, $\mu_C + \sigma_C$, and $\mu_C + 2\sigma_C$, respectively.

In particular, most of the broken links with centrality c_{br} near the curve of μ_C are boundary links, and most of the interior broken links have centrality c_{br} above the curve of $\mu_C + 2\sigma_C$. Hence we characterize the majority of broken links as (i) boundary links and (ii) interior links with centrality value c_{br} above 2 standard deviations (σ_C) from the average value μ_C. This result confirms our hypothesis that the links traversed by a large number of shortest paths are more likely to experience breakage.

Furthermore, we provide the statistics for the characterization of broken links based on betweenness centrality. As shown in Fig. 5.6, the broken links can be divided into the following four groups:

- Interior links with centrality value $c_{br} < \mu_C + \sigma_C$.
- Interior links with centrality value $\mu_C + \sigma_C < c_{br} < \mu_C + 2\sigma_C$.
- Interior links with centrality value $c_{br} > \mu_C + 2\sigma_C$.
- Boundary links (centrality value c_{br} close to μ_C).

The percentages of broken links in each of the four categories are given in Table 5.3 for various network samples. We see that as the network size N increases, more broken links fall into the third category, described by interior links with centrality $c_{br} > \mu_C + 2\sigma_C$.

It is important to note that broken links do not necessarily correspond to the shorter chains on weak paths, in terms of the number of Kuhn segments per chain. Our simulations show that shorter chains that belong to a small number of shortest paths are not more likely to break. The key feature that governs link-breaking events is the number of shortest paths passing through the link, which represents the betweenness centrality of a link.

Table 5.3: Percentages of broken links in the four categories for various network samples. Broken links are divided into interior and boundary links. Interior links are categorized into three groups based on the centrality value c_{br}: (i) c_{br} below 1 standard deviation (σ_C) from the average value μ_C, (ii) c_{br} between 1 and 2 standard deviations (σ_C) from μ_C, and (iii) c_{br} above 2 standard deviations (σ_C) from μ_C. Boundary links have c_{br} close to μ_C.

Sample	Interior, $< \sigma_C$	Interior, $1 \sim 2\sigma_C$	Interior, $> 2\sigma_C$	Boundary
$N = 20,$ Run 1	13.04%	14.13%	33.70%	39.13%
$N = 20,$ Run 2	7.22%	15.46%	36.08%	41.24%
$N = 40,$ Run 1	11.97%	17.95%	38.89%	31.20%
$N = 40,$ Run 2	10.17%	16.53%	38.98%	34.32%
$N = 60,$ Run 1	9.79%	14.07%	41.90%	34.25%
$N = 60,$ Run 2	11.06%	20.82%	42.08%	26.03%
$N = 80,$ Run 1	8.62%	21.07%	45.98%	24.33%
$N = 80,$ Run 2	13.43%	18.67%	48.47%	19.44%

5.3.3 Prediction of weak links

By analyzing the characteristics of link breakage, we find that broken links tend to occur on the lowest $p\%$ of shortest paths, where the percentile rank p ranges from 3 to 12. On these weak paths, the links that belong to a large number of shortest paths are more likely to break. Specifically, the events of link breakage can be characterized through the centrality value of the broken link c_{br}. It turns out that the majority of broken links are boundary links and interior links with centrality c_{br} above 2 standard deviations (σ_C) from the average number of shortest paths passing through each individual link, μ_C.

These findings serve as an amenable tool for predicting the weak links in the network. We identify the links that satisfy any of the following conditions as the weak links, which concentrate stress and tend to break shortly.

(i) Links on the global minimum shortest path $P_{\min}$.

(ii) Boundary links on the lowest $p\%$ of shortest paths.

(iii) Interior links on the lowest $p\%$ of shortest paths, whose centrality value c_{br} is above 2 standard deviations (σ_C) from the average value μ_C.

The statistics for the percentile rank p are given in Table 5.2 for various network samples. For illustration, multiple breaking scenarios are presented in Fig. 5.7, in which the stress of individual links is shown with the colorcode and the predicted weak links are highlighted. The left panel displays snapshots at the first breakage, while the right panel corresponds to breakage at the peak force. It can be seen that our prediction provides good agreement with those highly stressed links, especially for network samples of larger size (see Fig. 5.7(c)).

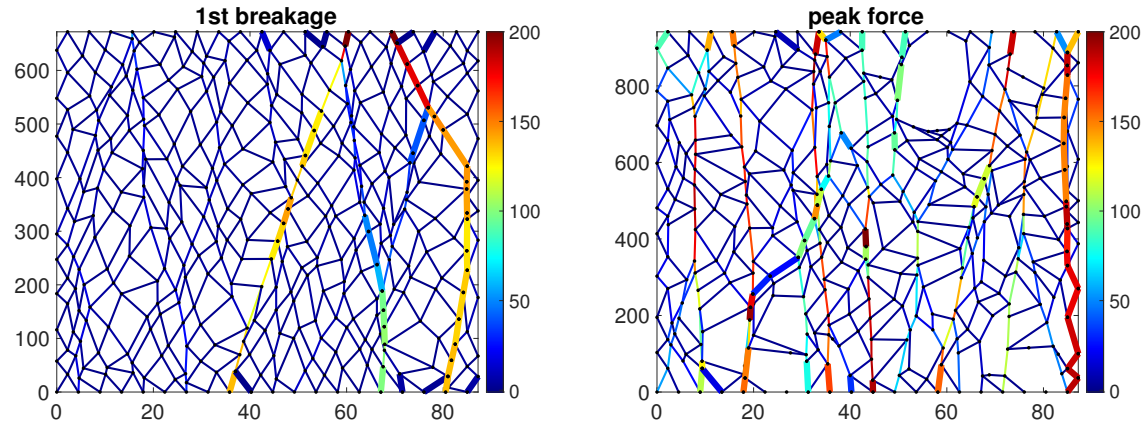

(a) 20×20 network

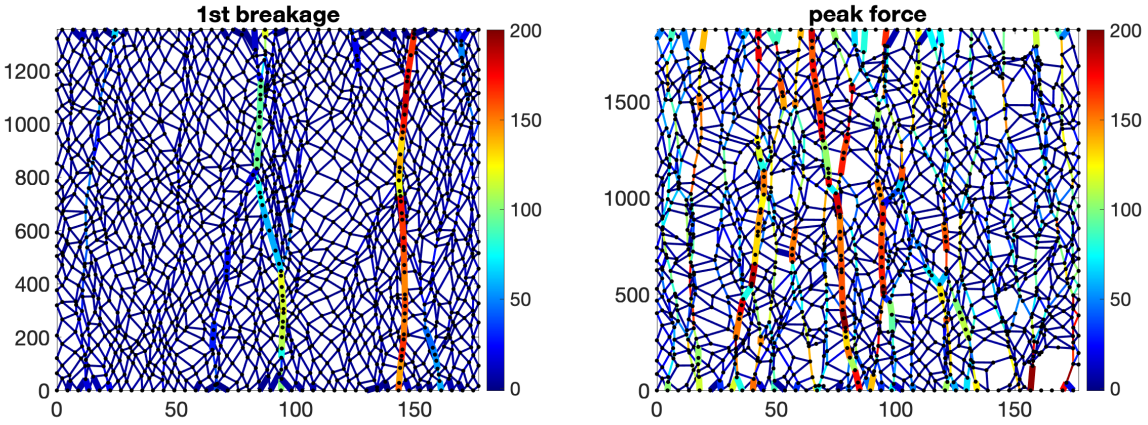

(b) 40×40 network

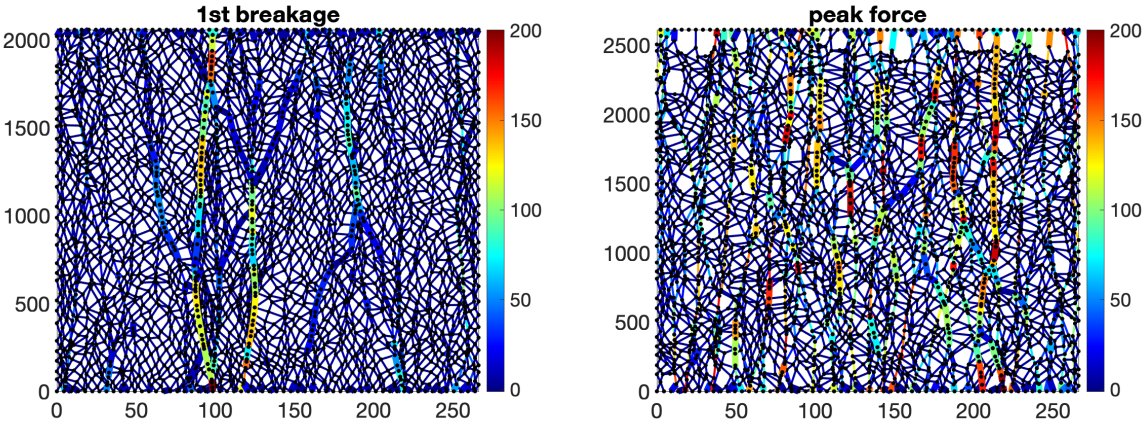

(c) 60×60 network

Figure 5.7: Illustrations for the predicted weak links (highlighted) in the network model. The left panel corresponds to the first breakage, while the right panel corresponds to the breaking scenario at peak force. The colorcode shows the stress of individual links.

Using the recipe above for the prediction of weak links, we are able to capture around 85% to 90% of the actual broken links in simulations, while keeping the number of predicted weak links small compared to the total number of links in the network. Notably, the subset of weak links predicted by the recipe above accounts for only 8% of the entire set of links. If we relax Condition (iii) by including interior links with centrality c_{br} above 1 standard deviation (σ_C) from the average μ_C, this allows us to capture 92% to 97% of the actual broken links, while the subset of predicted weak links is within 12% of the entire links.

We remark that there is a trade-off between the capture rate of broken links and the subset size of weak links. All the broken links can be captured if the prediction includes every link on the lowest p% of shortest paths. However, this increases the number of weak links by prediction to about 20% of the total number of links, yielding a rough estimate.

5.3.4 Evolution of shortest path lengths

In this section, we shift our focus towards investigating the second question proposed in Section 5.3. We seek to understand the connection between the microscopic events of link breakage and the macroscopic mechanical properties. In particular, we focus on the question of how the strength (i.e. peak force) of the polymer network is controlled by the microstructural evolution of the shortest paths in the network.

To address this question, we analyze the evolution of the shortest path (SP) length distribution in our network model, as suggested by [27]. The histograms of all SP lengths at initialization and at peak force are displayed in Fig. 5.8 for various network samples. The mean of the SP length distribution at initialization is shown for comparison.

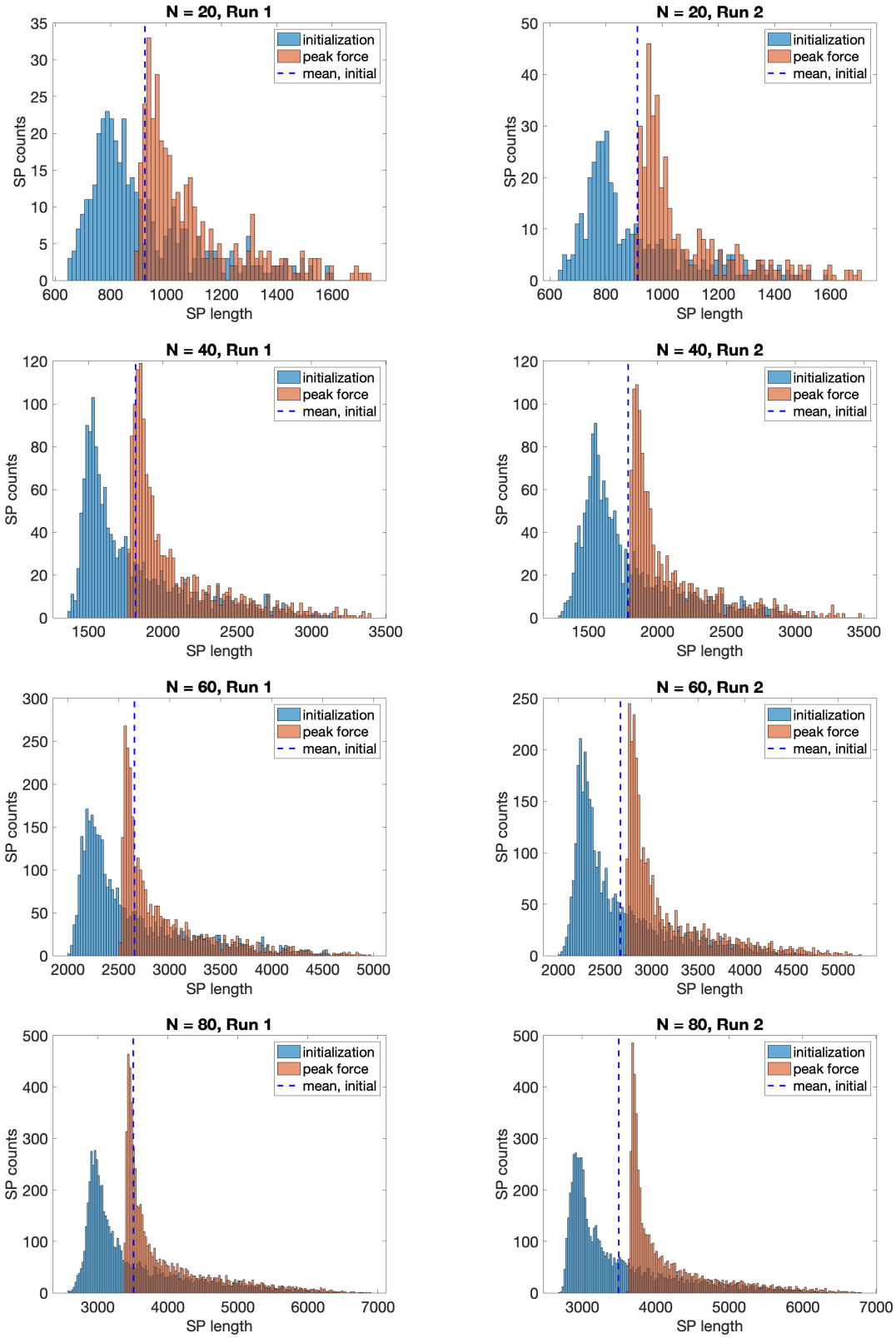

Figure 5.8: Histograms of shortest path (SP) lengths at initialization (blue) and at peak force (red). The blue dashed line represents the mean of the initial SP length distribution.

As seen in Fig. 5.8, the histograms of shortest path (SP) lengths exhibit a shape similar to the exponential distribution, especially for network samples of larger size $N = 80$. At the peak force, the SP distribution noticeably shifts to longer lengths. This behavior is attributed to the fact that every link-breaking event occurs on one or more shortest paths. After every breaking event, the shortest paths passing through the broken link are removed and replaced by new shortest paths with longer lengths, leading to the shift of histograms. Moreover, we notice that the SP length distribution at which strength is achieved exhibits a higher peak than the distribution at initialization.

Let D_0 and D_{pk} denote the set of shortest path (SP) lengths at initialization and at peak force, respectively. The mean of the set D_0 is shown in Fig. 5.8 with the dashed line. Among all the network samples, it is interesting to note that the minimum of SP lengths at peak force almost coincides with the mean of the initial SP length distribution, i.e.

$$\min\{D_{pk}\} \approx \text{mean}\{D_0\}.$$

This finding suggests that, during the evolution of shortest paths, the peak force occurs when the minimum SP length approximately reaches the average SP length at initialization. It establishes a direct connection between the microstructural evolution of the network and the macroscopic mechanical behavior.

Furthermore, we present the evolution of the average SP length and the minimum SP length in Fig. 5.9. Both curves grow almost linearly with increasing number of broken links. We note that the minimum SP length at peak force, indicated with the red marker, is very close to the initial average SP length (dashed line) for all network samples.

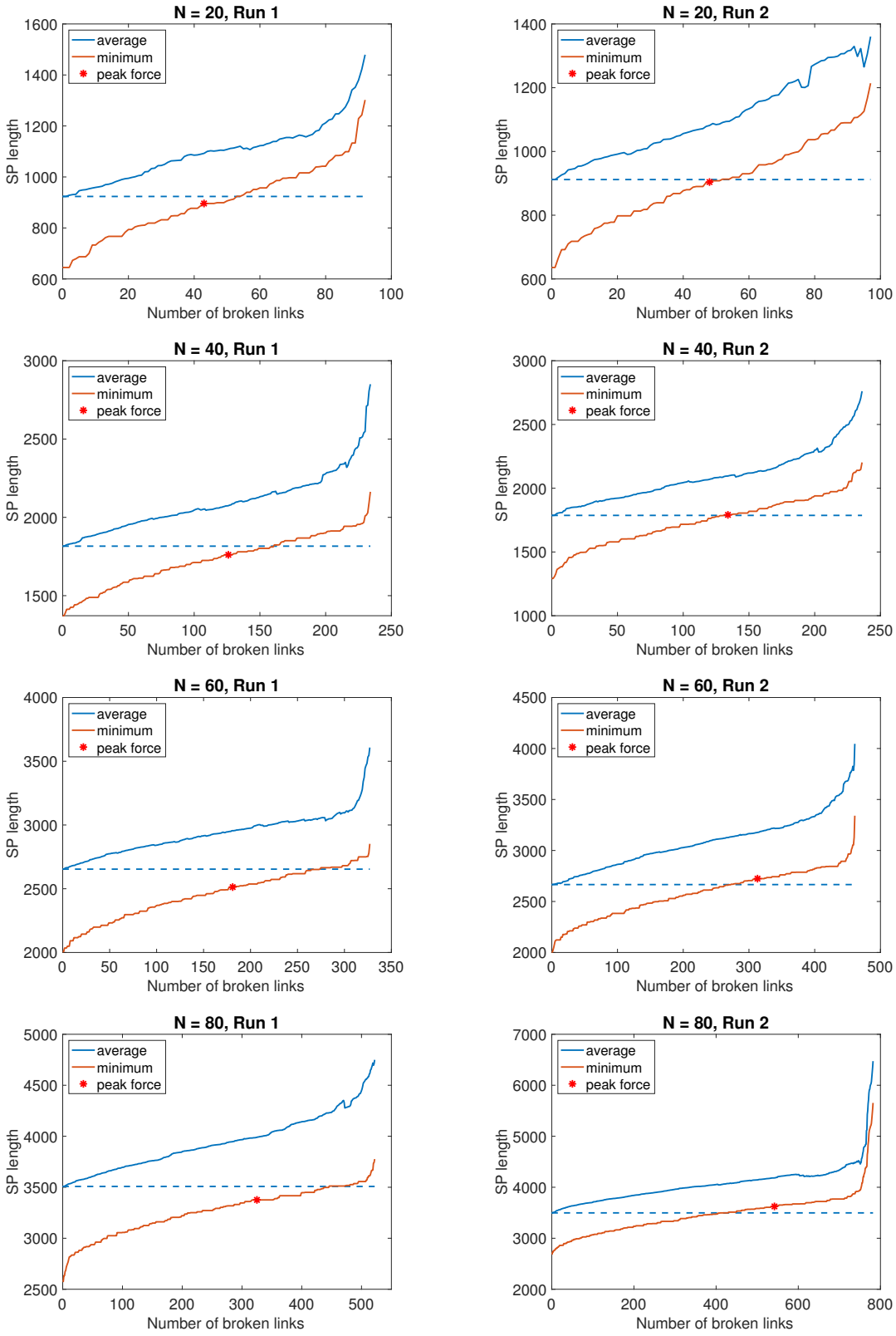

Figure 5.9: Evolution of the average SP length (blue) and the minimum SP length (red). The dashed line indicates the initial average length. The red marker indicates peak force.

5.4 Formation and growth of holes

In this section, we continue our study of the second question proposed in Section 5.3. That is, we investigate the question of when the strength of the polymer network is achieved with respect to the change of the network topology. We take an alternative perspective by studying the formation and growth of holes in the network.

5.4.1 Observations

We start with observations from breaking scenarios at different stages of deformation. We take one network sample of size 40×40 for illustration. The stress-stretch curve is shown in Fig. 5.10(a), in which we choose four different stretches. Breaking scenarios at the four stretches are displayed in Fig. 5.10. The second stretch λ_2 corresponds to the peak force. We have the following observations.

At stretch λ_1, where the force is low and starts to take off, broken links are separated and there is no essential change in the topology of the network. As the force grows and reaches the peak at stretch λ_2, a few isolated holes begin to emerge, while the entire network remains well connected to the top and bottom boundaries.

At stretch λ_3 where the force drops precipitously, the isolated holes are merged and two giant holes become noticeable. Nearly half of the boundary links are detached to the top of the network, hence the force required to stretch the network is considerably reduced. Once giant holes are developed, the subsequent broken links tend to be adjacent to them. The two giant holes in Fig. 5.10(d) continue to expand in size until reaching stretch λ_4, right before the point of complete fracture.

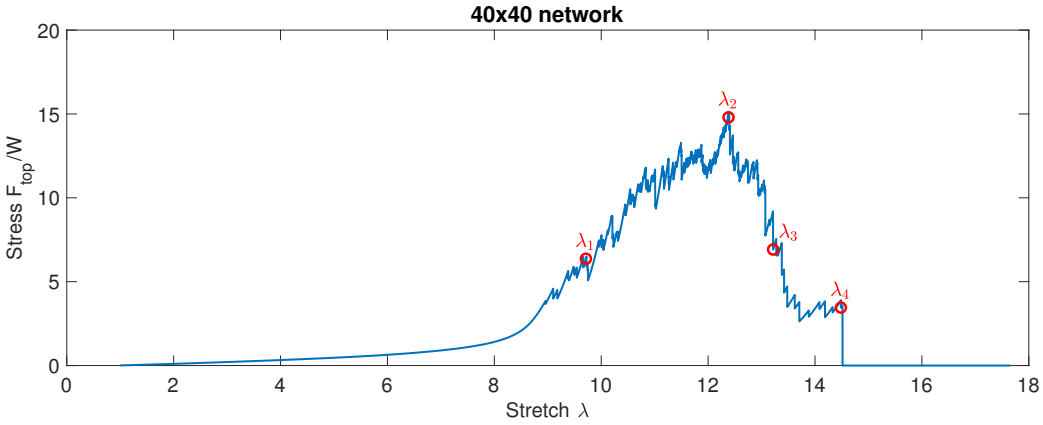

(a)

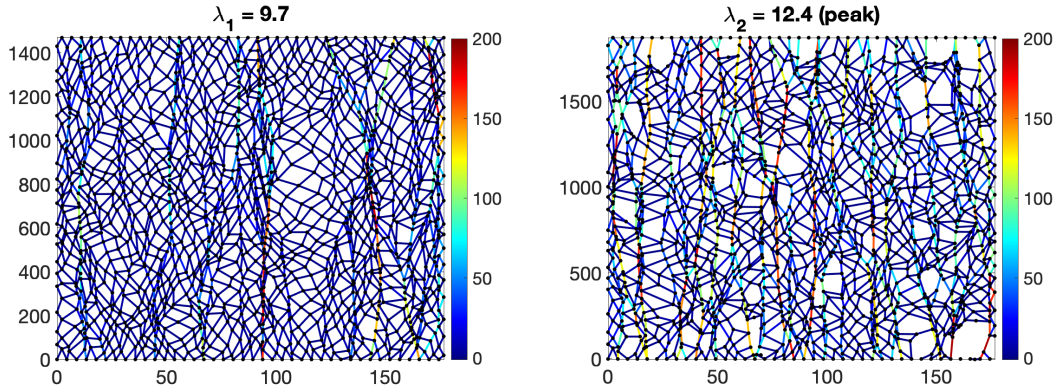

(b) (c)

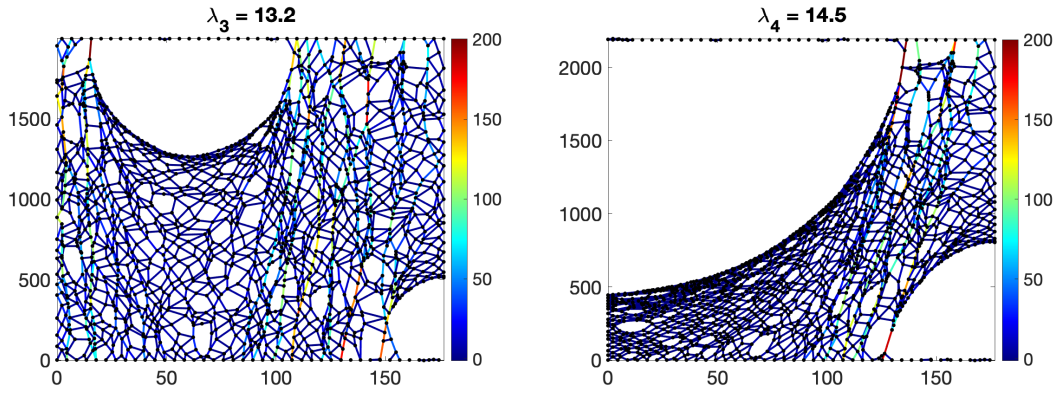

(d) (e)

Figure 5.10: (a): The stress-stretch curve for a 40×40 network sample. The force reaches the peak at stretch λ_2. (b,c,d,e): Breaking scenarios at the four stretches marked in (a).

We can see from Fig. 5.10 that the change in the magnitude of the applied force correlates to the development of holes. In particular, the maximum force (i.e. strength) is achieved when isolated holes are present. Once the isolated holes merge into a giant hole, the applied force drops down precipitously. These observations motivate us to investigate the formation and growth of holes that alter the topology of the network.

5.4.2 Phase transitions

In light of the observations above, we propose that there exist phase transitions in the network topology during deformation, as characterized by the development of holes:

- Stage (i): No noticeable holes (see Fig. 5.10(b)). At the initial stage, the force applied to the network is very low, and broken links are separated from each other.
- Stage (ii): Multiple isolated holes (see Fig. 5.10(c)). Each hole is created by at most a few adjacent broken links. The magnitude of the applied force is high and the peak force (i.e. strength) occurs at this stage.
- Stage (iii): One or two giant holes (see Fig. 5.10(d)). The isolated holes merge into one or two giant holes, and as a result the applied force drops down precipitously.

We provide the statistics for the development of holes during the deformation process. When a link breaks, it either creates a new hole, expand an existing hole, or merge two neighboring holes. We define the size of a hole by the number of missing links in the hole. The histograms of hole sizes at the three stages described above are presented in Fig. 5.11 for various network samples. For network samples of size larger than $N = 40$, we omit the holes of size 1 for which the number is considerably high.

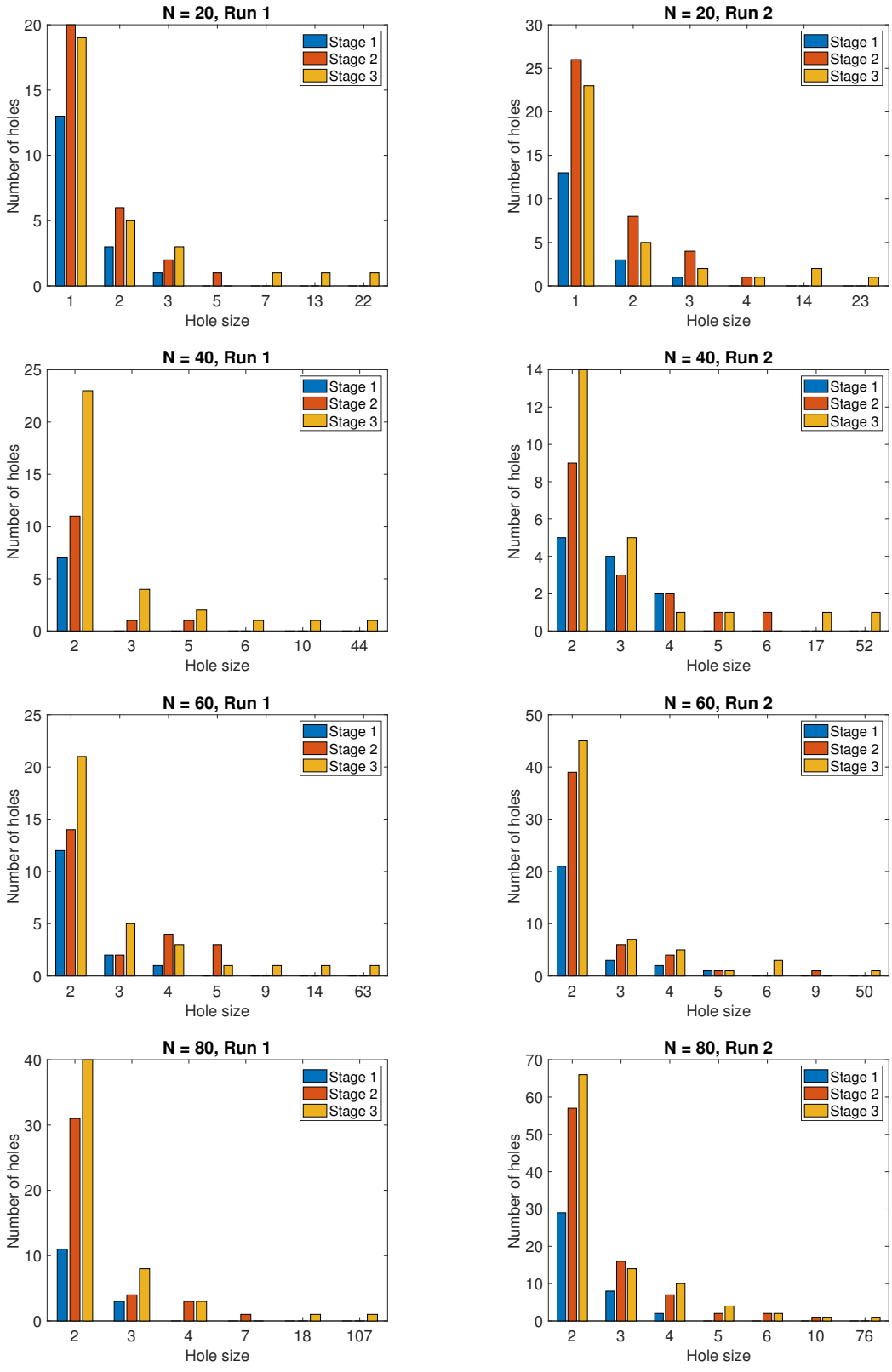

Figure 5.11: Histograms of hole sizes at the three stages showing phase transitions.

5.5 Discussion

We summarize the key findings of this chapter, which provide valuable insights into the breaking mechanism of the polymer network. Remarkably, our findings connect the microscopic characteristics of the network to the macroscopic mechanical properties.

By examining the shortest paths in the network model, we confirm that broken links tend to occur on the global minimum shortest path, or on the shortest path with length very close to the global minimum length. Furthermore, we find that the links traversed by a large number of shortest paths are more likely to experience breakage. These shortest paths are identified as the weak paths in the network, which concentrate the majority of the stress.

We quantitatively characterize the events of link breakage through a network measure called betweenness centrality, i.e., the number of shortest paths passing through each link. We find that weak links tend to be boundary links and interior links with centrality value above 2 standard deviations from the average number of shortest paths passing through each individual link. The identification of weak links provides insight into the understanding of stress concentration in the polymer network.

By studying the distribution of shortest path lengths, we relate the strength of the network model to the evolution of the minimum shortest path length. We find that the peak force occurs when the minimum shortest path length approaches the initial average length of shortest paths. In other words, when the shortest path with average length at initialization becomes the global minimum shortest path, strength is achieved. This finding is consistent with the fact that shortest paths concentrate most of the stress in the network.

An alternative perspective is taken to investigate the connection between the strength and the microscopic characteristics of the network. We observe the presence of isolated holes when the network model reaches the peak force. As the isolated holes merge into one or two giant holes, the force applied to the network drops down precipitously. In light of these observations, we propose that there exist phase transitions in the topology of the network, characterized by the formation and growth of holes.

The statistics for the development of holes are consistent with the proposed phase transitions in the network topology. We observe that the magnitude of the applied force remains high while isolated holes exist in the network. Once the isolated holes merge into giant holes, the subsequent broken links tend to be adjacent to them, and as a result the applied force drops precipitously. These findings motivate the task of developing a network growth model that accounts for the development of holes, which remains as future work.

Chapter 6: Conclusions and perspectives

6.1 Conclusions

In this dissertation, two mesoscale models that assume a statistical distribution for the lengths of polymer chains are developed to investigate the fracture properties of polymer networks. In both models, polymer chains are represented by freely-jointed chains that feature a nonlinear J-shaped stress-stretch relationship.

Our models show that the combination of a J-shaped stress-stretch relationship and a distribution of chain lengths leads to a large reduction in strength, while keeping the variability in strength small between samples. The results of our models are in qualitative agreement with the experimental observations for the fracture properties of hydrogels [10].

The reduction in strength obtained by our models accounts for a portion of the giant discrepancy between the experimentally measured strength of hydrogels and the strength of covalent bonds [10]. The parallel chain model demonstrates a large reduction in strength by up to two orders of magnitude. The network model shows a reduction in strength by about a factor of 7. Although the magnitude of the reduction is not large enough, the network model provides a more realistic representation of the polymer network.

Furthermore, our models demonstrate a power law relationship between the strength and the scatter in chain lengths. The strength of the parallel chain model is approximately

inversely proportional to the scatter in chain lengths, while the decay rate of the power law in the network model is slower. This discrepancy is attributed to the underlying structural differences between two models.

One limitation of the network model is that the power law between the strength and the scatter in chain lengths cannot be extrapolated to larger network sizes, and numerical simulations of larger networks are much more computationally demanding. This difficulty is addressed by the parallel chain model.

An advantage of the parallel chain model is that it allows for simple calculations and is amenable for analysis by analytical tools. The simplicity of the parallel chain model allows us to derive the power law analytically, thereby providing insight into the origin of the power law relationship between the strength and the scatter in chain lengths.

Admittedly, the reduction in strength obtained by both models is not large enough to account for the experimentally observed strength reduction [10]. The parallel chain model does not take into account the concentration of stress, which is believed to play a role in reducing strength. On the other hand, the network model is only amenable for numerical simulations and the computational complexity remains a challenge.

The investigation of the microscopic characteristics of the network model provides us with new insight into the underlying breaking mechanism. The shortest paths are identified as the weak paths where the stress tends to concentrate. The links that belong to a large number of shortest paths are more likely to break. Finally, we connect the microscopic characteristics to the macroscopic mechanical properties. It is observed that the strength of the network correlates with the development of holes during deformation.

6.2 Perspectives

The reduction in strength predicted by our models is not large enough to account for the giant discrepancy between the experimentally measured strength of hydrogels and the strength of covalent bonds [10]. This finding suggests that there exist other contributing factors to this phenomenon.

From the physical perspective, the spontaneous breakage of polymer chains may be a potential factor that further reduces strength. That is, there is a higher probability for the chain at larger extension to break before reaching its full contour length. Moreover, the actual length distribution of polymer chains is rarely measured. While we employ the estimated chain length distribution that is similar to the Weibull distribution, the exact distribution of chain lengths needs to be examined. Another contributing factor may be chemical reactions in the polymer network. A real polymer network is filled with fluids. The chemical reactions caused by fluid molecules may play a role.

From the mathematical perspective, in order to understand the development of holes, a network growth model needs to be developed using random graph theory. Furthermore, the statistics for shortest paths are done only for the Weibull distribution of chain lengths. We believe it is of interest to analytically examine the shortest path length distribution. This can be approached by means of extreme value theory [64].

Bibliography

[1] N. G. McCrum, C. P. Buckley, C. Buckley, and C. Bucknall, *Principles of polymer engineering*. Oxford University Press, 1997.

[2] P. C. Painter and M. M. Coleman, *Fundamentals of polymer science: An introductory text*. Routledge, 2019.

[3] J. L. Drury and D. J. Mooney, "Hydrogels for tissue engineering: scaffold design variables and applications," *Biomaterials*, vol. 24, no. 24, pp. 4337–4351, 2003.

[4] T. R. Hoare and D. S. Kohane, "Hydrogels in drug delivery: Progress and challenges," *Polymer*, vol. 49, no. 8, pp. 1993–2007, 2008.

[5] W. Yang, V. R. Sherman, B. Gludovatz, E. Schaible, P. Stewart, R. O. Ritchie, and M. A. Meyers, "On the tear resistance of skin," *Nature Communications*, vol. 6, no. 1, pp. 1–10, 2015.

[6] S. Ling, Q. Zhang, D. L. Kaplan, F. Omenetto, M. J. Buehler, and Z. Qin, "Printing of stretchable silk membranes for strain measurements," *Lab on a Chip*, vol. 16, no. 13, pp. 2459–2466, 2016.

[7] G. A. Holzapfel, "Biomechanics of soft tissue," *The Handbook of Materials Behavior Models*, vol. 3, no. 1, pp. 1049–1063, 2001.

[8] E. M. Ahmed, "Hydrogel: Preparation, characterization, and applications: A review," *Journal of Advanced Research*, vol. 6, no. 2, pp. 105–121, 2015.

[9] S. Bashir, M. Hina, J. Iqbal, A. Rajpar, M. Mujtaba, N. Alghamdi, S. Wageh, K. Ramesh, and S. Ramesh, "Fundamental concepts of hydrogels: Synthesis, properties, and their applications," *Polymers*, vol. 12, no. 11, p. 2702, 2020.

[10] C. Yang, T. Yin, and Z. Suo, "Polyacrylamide hydrogels. I. Network imperfection," *Journal of the Mechanics and Physics of Solids*, vol. 131, pp. 43–55, 2019.

[11] B. Proctor, I. Whitney, and J. Johnson, "The strength of fused silica," *Proceedings of the Royal Society of London. Series A. Mathematical and Physical Sciences*, vol. 297, no. 1451, pp. 534–557, 1967.

[12] A. A. Griffith, "VI. The phenomena of rupture and flow in solids," *Philosophical Transactions of the Royal Society of London. Series A. Mathematical and Physical Sciences*, vol. 221, no. 582-593, pp. 163–198, 1921.

[13] L. G. Treloar, "The physics of rubber elasticity," 2005.

[14] J. Kim, G. Zhang, M. Shi, and Z. Suo, "Fracture, fatigue, and friction of polymers in which entanglements greatly outnumber cross-links," *Science*, vol. 374, no. 6564, pp. 212–216, 2021.

[15] G. Lake and A. Thomas, "The strength of highly elastic materials," *Proceedings of the Royal Society of London. Series A. Mathematical and Physical Sciences*, vol. 300, no. 1460, pp. 108–119, 1967.

[16] L. Mullins, "Effect of stretching on the properties of rubber," *Rubber Chemistry and Technology*, vol. 21, no. 2, pp. 281–300, 1948.

[17] M. Tehrani and A. Sarvestani, "Effect of chain length distribution on mechanical behavior of polymeric networks," *European Polymer Journal*, vol. 87, pp. 136–146, 2017.

[18] E. Ducrot, Y. Chen, M. Bulters, R. P. Sijbesma, and C. Creton, "Toughening elastomers with sacrificial bonds and watching them break," *Science*, vol. 344, no. 6180, pp. 186–189, 2014.

[19] Y. Mao and L. Anand, "A theory for fracture of polymeric gels," *Journal of the Mechanics and Physics of Solids*, vol. 115, pp. 30–53, 2018.

[20] J. Rottler, S. Barsky, and M. O. Robbins, "Cracks and crazes: on calculating the macroscopic fracture energy of glassy polymers from molecular simulations," *Physical Review Letters*, vol. 89, no. 14, p. 148304, 2002.

[21] J. Rottler and M. O. Robbins, "Growth, microstructure, and failure of crazes in glassy polymers," *Physical Review E*, vol. 68, no. 1, p. 011801, 2003.

[22] W. Kuhn and F. Grün, "Beziehungen zwischen elastischen Konstanten und Dehnungsdoppelbrechung hochelastischer Stoffe," *Kolloid-Zeitschrift*, vol. 101, no. 3, pp. 248–271, 1942.

[23] W. Zhang, S. Zou, C. Wang, and X. Zhang, "Single polymer chain elongation of poly(N-isopropylacrylamide) and poly(acrylamide) by atomic force microscopy," *The Journal of Physical Chemistry B*, vol. 104, no. 44, pp. 10258–10264, 2000.

[24] M. Itskov and A. Knyazeva, "A rubber elasticity and softening model based on chain length statistics," *International Journal of Solids and Structures*, vol. 80, pp. 512–519, 2016.

[25] S. R. Lavoie, R. Long, and T. Tang, "A rate-dependent damage model for elastomers at large strain," *Extreme Mechanics Letters*, vol. 8, pp. 114–124, 2016.

[26] T. Yang, K. M. Liechti, and R. Huang, "A multiscale cohesive zone model for rate-dependent fracture of interfaces," *Journal of the Mechanics and Physics of Solids*, vol. 145, p. 104142, 2020.

[27] Y. Yin, N. Bertin, Y. Wang, Z. Bao, and W. Cai, "Topological origin of strain induced damage of multi-network elastomers by bond breaking," *Extreme Mechanics Letters*, vol. 40, p. 100883, 2020.

[28] S. R. Lavoie, P. Millereau, C. Creton, R. Long, and T. Tang, "A continuum model for progressive damage in tough multinetwork elastomers," *Journal of the Mechanics and Physics of Solids*, vol. 125, pp. 523–549, 2019.

[29] W. Kuhn, "Über die gestalt fadenförmiger moleküle in lösungen," *Kolloid-Zeitschrift*, vol. 68, no. 1, pp. 2–15, 1934.

[30] W. Kuhn and H. Kuhn, "Die Frage nach der Aufrollung von Fadenmolekeln in strömenden Lösungen," *Helvetica Chimica Acta*, vol. 26, no. 5, pp. 1394–1465, 1943.

[31] L. Boltzmann, "Studien uber das gleichgewicht der lebenden kraft," *Wissenschafiliche Abhandlungen*, vol. 1, pp. 49–96, 1868.

[32] R. Jedynak, "Approximation of the inverse Langevin function revisited," *Rheologica Acta*, vol. 54, no. 1, pp. 29–39, 2015.

[33] A. Cohen, "A padé approximant to the inverse Langevin function," *Rheologica Acta*, vol. 30, no. 3, pp. 270–273, 1991.

[34] M. Tao, S. R. Lavoie, Z. Suo, and M. K. Cameron, "The effect of scatter of polymer chain length on strength," *Extreme Mechanics Letters*, p. 102024, 2023.

[35] J. Liu, C. Yang, T. Yin, Z. Wang, S. Qu, and Z. Suo, "Polyacrylamide hydrogels. II. Elastic dissipater," *Journal of the Mechanics and Physics of Solids*, vol. 133, p. 103737, 2019.

[36] R. J. Twiss and E. M. Moores, *Structural geology*. Macmillan, 1992.

[37] Y. Nesterov, "A method for unconstrained convex minimization problem with the rate of convergence $O(1/k^2)$," *Soviet Mathematics Doklady*, vol. 27, pp. 372–376, 1983.

[38] J. Nocedal and S. J. Wright, *Numerical optimization*. Springer Science & Business Media, 2006.

[39] D. P. Kingma and J. Ba, "Adam: a method for stochastic optimization," in *Proceedings of the 3rd International Conference on Learning Representations*, pp. 1–13, 2015.

[40] S. R. Lavoie and Z. Suo, "Flaw sensitivity of stochastic elastic materials." Manuscript submitted for publication, 2023.

[41] B. O'Donoghue and E. J. Candès, "Adaptive restart for accelerated gradient schemes," *Foundations of Computational Mathematics*, vol. 15, no. 3, pp. 715–732, 2015.

[42] B. T. Polyak, "Some methods of speeding up the convergence of iteration methods," *USSR Computational Mathematics and Mathematical Physics*, vol. 4, no. 5, pp. 1–17, 1964.

[43] I. Sutskever, J. Martens, G. Dahl, and G. Hinton, "On the importance of initialization and momentum in deep learning," in *Proceedings of the 30th International Conference on Machine Learning*, pp. 1139–1147, PMLR, 2013.

[44] Y. Nesterov, *Introductory lectures on convex optimization: A basic course*, vol. 87. Springer Science & Business Media, 2003.

[45] E. Ghadimi, H. R. Feyzmahdavian, and M. Johansson, "Global convergence of the heavy-ball method for convex optimization," in *2015 European Control Conference (ECC)*, pp. 310–315, IEEE, 2015.

[46] W. Su, S. Boyd, and E. J. Candès, "A differential equation for modeling Nesterov's accelerated gradient method: theory and insights," *Journal of Machine Learning Research*, vol. 17, pp. 1–43, 2016.

[47] Y. Nesterov, "Smooth minimization of non-smooth functions," *Mathematical Programming*, vol. 103, pp. 127–152, 2005.

[48] Y. Nesterov, "Gradient methods for minimizing composite functions," *Mathematical Programming*, vol. 140, no. 1, pp. 125–161, 2013.

[49] P. Tseng, "On accelerated proximal gradient methods for convex-concave optimization," *SIAM Journal on Optimization*, vol. 2, no. 3, 2008.

[50] J. Duchi, E. Hazan, and Y. Singer, "Adaptive subgradient methods for online learning and stochastic optimization.," *Journal of Machine Learning Research*, vol. 12, no. 7, 2011.

[51] M. D. Zeiler, "Adadelta: an adaptive learning rate method," *arXiv preprint arXiv:1212.5701*, 2012.

[52] T. Dozat, "Incorporating Nesterov momentum into Adam," *ICLR Workshop*, 2016.

[53] A. Beck and M. Teboulle, "A fast iterative shrinkage-thresholding algorithm for linear inverse problems," *SIAM Journal on Imaging Sciences*, vol. 2, no. 1, pp. 183–202, 2009.

[54] A. Botev, G. Lever, and D. Barber, "Nesterov's accelerated gradient and momentum as approximations to regularised update descent," in *2017 International Joint Conference on Neural Networks (IJCNN)*, pp. 1899–1903, IEEE, 2017.

[55] S. Becker, J. Bobin, and E. J. Candès, "NESTA: a fast and accurate first-order method for sparse recovery," *SIAM Journal on Imaging Sciences*, vol. 4, no. 1, pp. 1–39, 2011.

[56] Z. Qin and D. Goldfarb, "Structured sparsity via alternating direction methods," *Journal of Machine Learning Research*, vol. 13, no. 5, pp. 1435–1468, 2012.

[57] A. Chortos and Z. Bao, "Skin-inspired electronic devices," *Materials Today*, vol. 17, no. 7, pp. 321–331, 2014.

[58] S. Wagner and S. Bauer, "Materials for stretchable electronics," *Mrs Bulletin*, vol. 37, no. 3, pp. 207–213, 2012.

[59] J. P. Gong, "Materials both tough and soft," *Science*, vol. 344, no. 6180, pp. 161–162, 2014.

[60] P. Millereau, E. Ducrot, J. M. Clough, M. E. Wiseman, H. R. Brown, R. P. Sijbesma, and C. Creton, "Mechanics of elastomeric molecular composites," *Proceedings of the National Academy of Sciences*, vol. 115, no. 37, pp. 9110–9115, 2018.

[61] P. Cordier, F. Tournilhac, C. Soulié-Ziakovic, and L. Leibler, "Self-healing and thermoreversible rubber from supramolecular assembly," *Nature*, vol. 451, no. 7181, pp. 977–980, 2008.

[62] M. Burnworth, L. Tang, J. R. Kumpfer, A. J. Duncan, F. L. Beyer, G. L. Fiore, S. J. Rowan, and C. Weder, "Optically healable supramolecular polymers," *Nature*, vol. 472, no. 7343, pp. 334–337, 2011.

[63] M. Newman, *Networks*. Oxford University Press, 2018.

[64] L. Haan and A. Ferreira, *Extreme value theory: An introduction*, vol. 3. Springer, 2006.